

MSc Physics and Astronomy (joint degree)
Advanced Matter and Energy Physics track

Master Thesis

Tweezer machine for Sr atoms using a homebuilt microscope objective from commercial lenses

by

I.H.A. Knottnerus

10433643

August 2018

60EC

September 2017 - August 2018

Supervisor/Examiner:

prof. dr. F. E. Schreck

Examiner:

prof. dr. H.B. van Linden van den Heuvell

in the

Faculty of Science

Van der Waals-Zeeman Institute

UNIVERSITY OF AMSTERDAM

Abstract

Faculty of Science
Van der Waals-Zeeman Institute

Master of Science

by I.H.A. Knottnerus

In recent years, optical tweezers have been used to create defect-free arrays of single atoms in tailor-made configurations, opening doors to a wide range of quantum simulation experiments. In this thesis, the modification of an existing ultra-cold quantum gas machine for the purpose of Sr optical tweezer experiments is reported. A high resolution long working distance microscope objective is designed using commercial lenses only. The design is predicted to be diffraction-limited with $NA = 0.44$ for 461 nm light, while having a working distance of 18.1 mm. The design is corrected for a 3.175 mm thick fused silica viewport. A simple stacking design is made for the housing and a prototype of the objective is built from PEEK. The performance of the objective has been measured by illumination of a test target containing six 200 nm diameter pinholes. The resolution is measured to be $0.63(4) \mu\text{m}$ for 461 nm light. Furthermore, the objective is shown to have a resolution close to the diffraction limit for 532 nm light, which is used as tweezer light. A low number of atoms is loaded into the tweezer and first steps towards single atom detection of Sr are taken.

Dutch summary

Het experimenteel bestuderen van complexe kwantummechanische systemen is één van de grote uitdagingen in de hedendaagse natuurkunde. Eén van de veelbelovendste technieken om dit te doen is kwantumsimulatie. Hierbij wordt een zeer goed bekend en gecontroleerd systeem gebruikt als analogie voor een systeem dat lastiger te meten is in het lab. Een systeem dat bij uitstek geschikt is voor kwantumsimulatie zijn ultrakoude atomen, doordat parameters zoals de interacties tussen de atomen onderling over een groot domein te variëren zijn en de theoretische basis goed bekend is. Een belangrijke manier om ultrakoude atomen te gebruiken voor kwantumsimulatie is door middel van een *tweezer machine*. Hierin worden lichtbundel sterk gefocuseerd om meerdere vallen te maken waar één enkel atoom in gevangen kan worden. De meerdere vallen kunnen vervolgens verplaatst worden om arbitraire configuraties te maken, waardoor een hele generatie aan nieuwe simulatie-experimenten kan plaatsvinden. Er zijn bijvoorbeeld theoretische voorstellen gedaan om zo *quantum gates* te maken met ultrakoude atomen die weer kunnen leiden tot *quantum computing*.

In deze scriptie is verslag gelegd van het ombouwen van een bestaande machine voor ultrakoud Sr tot een tweezer machine. Voor het creëren van de vallen waarin de atomen geladen kunnen worden, is een objectief ontworpen van enkel commercieel verkrijgbare lenzen. Het ontwerp heeft een numerieke apertuur van 0.44, is geoptimaliseerd voor 461 nm licht en is gecorrigeerd voor een 3.175 mm venster dat tussen het objectief en de vacuümkamer staat. De voorspelde resolutie van het ontwerp is enkel gelimiteerd door diffractie. Er is ook een prototype van het objectief gemaakt met een simpel stapelontwerp voor de behuizing, gemaakt van PEEK. Dit prototype is vervolgens getest door het diffractiepatroon te meten van zes belichte gaatjes met 200 nm diameter. De resolutie voor 461 nm licht is gemeten als 0.63(4) μm , wat uitstekend overeenkomt met de voorspelde diffractielimiet. Verder is het objectief getest voor 532 nm licht, het licht voor de tweezer vallen, waarbij een resolutie dichtbij de diffractielimiet gevonden is, wat betekent dat het objectief goed gebruikt kan worden voor het bouwen van een tweezer machine. Nadat het objectief op de machine was geplaatst om een tweezer machine te vormen, zijn er stappen gezet richting het laden van enkele Sr atomen in de tweezer.

Acknowledgements

I would like to thank everyone who has helped me in writing this thesis. First and foremost, I would like to thank my supervisor prof. dr. Florian Schreck, for giving me the opportunity to do my project in his wonderful lab, where I have learned so much. Not only is Florian a gifted teacher and experimentalist, he also has an enthusiasm for physics in general that has no equal that I know of and is very infectious. I am very grateful to have been a member of the strontium family that Florian has created in Amsterdam and hope he can continue to be a role model for many more like me to come, the same way he has been and continues to be that for me.

Secondly, I would want to say a great thank you to the quantum gas microscope team for everything this year. First of all, my direct supervisor in the team, to Georgios Siviloglou, whose brainchild our machine is. Georgios always had a solution if I presented him a problem and has been very encouraging throughout the whole project, even when his stay in Amsterdam ended and he moved to China. I am sure some great physics will be done in his new group! Then there is Oleksiy Onishchenko, who tackles every problem head-on, seems to have an endless patience and speaks about 10 languages. Thank you for all the discussions, taking over Georgios' role in his absence, and most importantly, for the many chit-chats we would have. Also thank you for the evenings you spent correcting this document. Thank you to Sergey Pyatchnikov, the quizmaster, who would always listen to my ideas or problems and then interrupt me and start questioning basically every sentence I uttered. It has been a remarkably effective way of straightening my thoughts and has helped me a lot. Also thanks to Alex Urech, who is a good runner-up in enthusiasm after Florian. I have been amazed by the amount of solutions Alex can produce and how fast he can adapt to new situations. Last but not least, thank you to Carla Sanna, who had the difficult job of merging into our team when we were all head-over-heels building stuff, but succeeded extremely well. Thank you for the fun in the lab and the construction and testing of the green beam paths for the tweezers.

I also want to express my gratitude to the other teams in the lab, the atom laser team and RbSr team, for sharing the lab and the equipment with me. Thanks to Vincent Barbé for re-locking the master lasers a thousand times and thanks to Lukas Reichsöllner for teaching me how to repair the 10m fiber that I had torn in two pieces. Also thank you to Benjamin Pasquiou for keeping the lab in a workable condition both in terms of safety and in terms of tidiness, and for sharing your experience when we needed some help. And for the rest of the team members: Rodrigo, Severin, Shayne, Chun-Chia and Alessio, thank you for the tips you provided me along the way and the discussions during lunch and/or diner. To all of you in this little strontium family, I have felt that I

could literally ask anybody in the whole team for help at any time, which is something I cannot thank you all enough for.

Moving over to the other end of the building, I want to thank the people of the workshop in our university without whom the whole objective could never have been built at all. Especially, thank you to Hans Ellermeijer, whose coffee/tea break I have ended countless times and who has made all the designs in Inventor. Thank you as well, Hans, for the vast number of discussions and also the small practical solutions that you came up with that are so simple I would not have thought of them if you gave me another year. Thanks to Fred, Tristan and Sven for the construction of the components of the objective. I also want to thank the people from the *Practicum Natuur- en Sterrenkunde* for letting me borrow their optical rail and translation stages, which allowed us to build a setup to test the objective.

Leaving the country even, I want to thank Joakim Reuteler from the ETH Zürich, who has been so kind to make the test target that we used to measure the resolution of our objective.

Finally, I want to thank the persons who are most important to me, my family: my parents Dries and Amy, my siblings George and Suzan, and of course, my girlfriend Anna, thank you for helping me on my way to this point. Without your unconditional support I would not have been able to write this. Also thanks for your understanding for all the times I was busy or tired and you had to be the persons to cheer me up again.

Contents

Abstract	i
Dutch summary	ii
Acknowledgements	iii
1 Introduction	1
1.1 Ultra-cold atoms for quantum simulation	1
1.2 High resolution objectives for imaging quantum gases	3
1.3 Thesis outline	4
2 Theory of imaging with a high-NA objective	5
2.1 Paraxial approximation and Gaussian beams	5
2.2 Validity of the paraxial approximation	8
2.3 Resolution and the PSF of an imaging system	9
2.4 Optical aberrations	12
2.4.1 Defocus	12
2.4.2 Spherical aberration	14
2.4.3 Coma	15
2.4.4 Astigmatism	15
2.4.5 Chromatic aberration	16
3 Building a high resolution objective with commercial lenses	17
3.1 Lens design	17
3.2 Tolerances on the design	20
3.2.1 Tolerances on the placement of the objective	21
3.2.2 Tolerances on the placement of lenses	22
3.2.3 Monte Carlo analysis of the success rate	24
3.3 Housing of the objective	25
3.3.1 Picking the housing design	25
3.3.2 Building material considerations	27
3.3.3 Extra features in the design	28
3.4 Assembly procedure	29

4	Testing the performance of the objective	31
4.1	Test setup outside the machine	31
4.1.1	Creating point sources of light	31
4.1.2	Complete test setup	33
4.2	Resolution of the objective	34
4.3	Additional performance measurements	37
4.3.1	Depth of field and 3D PSF	37
4.3.2	Field of view	38
4.3.3	Other wavelengths	39
5	Theory of single atom preparation for Sr	42
5.1	Getting to know strontium	42
5.2	Atom-light interactions	44
5.2.1	Near-resonant regime	44
5.2.2	Off-resonant regime	45
5.3	Preparation of single atoms	47
5.3.1	Loading using a Poisson distribution	47
5.3.2	Collisional blockade	48
5.3.3	Light-assisted collisions with more than 50 % success rate	49
5.4	Detecting single atoms using fluorescence imaging	53
6	Towards single atom detection of Sr in a tweezer	55
6.1	The tweezer machine	55
6.1.1	Installation of the objective	56
6.1.2	Blue beam path	58
6.1.3	Green beam path	58
6.1.4	Red beam path	60
6.2	EMCCD camera calibration	61
6.3	Tweezer trap measurements	62
6.4	Preliminary results	64
6.4.1	Experimental procedures	64
6.4.2	Histograms of the fluorescence signal	67
6.5	Beyond single atom detection	70
7	Conclusion & Outlook	72
A	Focusing the objective	74
A.1	Ray transfer calculations	74
A.1.1	Focusing with objective	75
A.1.2	Focusing with field lens	76
A.1.3	Comparison of methods	76
B	Calculation of the deconvolution of two Gaussian functions	78
C	Monte Carlo analysis of the assembly success rate	80

D CAD Drawings Thesis

82

Bibliography

91

Chapter 1

Introduction

One of the most challenging fields of research in modern day physics is the experimental study of quantum physics. The study of complicated quantum systems cannot be performed using classical computers. The most powerful argument for this was provided to me by my supervisor, prof. Florian Schreck: let us assume a quantum system of N entangled two-level particles, then the total number of eigenstates of the system is well known to be 2^N [1]. This is also the number of classical bits needed to store the system in the memory of a computer. Now if we consider all of the estimated 10^{86} atoms in the universe to be connected as bits in a universal classical supercomputer, still a quantum state of only $N = 285$ particles could be stored.

The most well-known attempt to solve this problem is the research and development of quantum computers. However, the most recent quantum computers suffer from decoherence issues and the maximal number of qubits that could perform a calculation is 7 qubits, whereas at least 50 qubits are needed to exceed modern classical supercomputers [2]. Instead of calculation, simulation can also be used to study quantum systems. This was proposed in the early 1980's by the late Richard Feynman [3], but the concept of simulation in physics was not new at all. The ancient Greeks already had orreries to simulate the movements of planets solar system [4]. Much like the orrery example, in quantum simulation a well-controlled quantum system is used as a mathematical analogy for an interesting quantum system that is difficult to study directly.

1.1 Ultra-cold atoms for quantum simulation

Ultra-cold atoms have emerged in recent years as an excellent candidate system for quantum simulation experiments. Reasons for the appeal of ultra-cold atoms include

the excellent control of the environment of the system in the ultra-high vacuum, the wide range over which many parameters such as the interactions between atoms can be varied with lasers and magnetic fields and the relatively well-known theoretical basis of the systems [5, 6]. Advances in laser trapping and cooling techniques of neutral atoms such as the magneto-optical trap [7] and evaporative cooling in dipole traps [8, 9] have opened doors to ultra-cold temperatures below 1 μ K and have made quantum degenerate gases of neutral atoms accessible. The first BEC was formed from Rb atoms in 1995 [10] and afterwards BECs have been shown for many other atomic species, mainly alkali and alkaline-earth atoms due to their favourable transitions in the optical spectrum [11–13]. Only a few years after that, in 1999, also fermions have been cooled to quantum degeneracy to create a superfluid phase of matter [14–16]. Almost two decades later, the quantum gases themselves have evolved from an object of study to a tool for e.g. quantum simulation.

One of the types of physics that can be simulated with quantum gases is quantum magnetism. Researching magnetic fields in quantum systems and the interaction of charged matter with magnetic fields is an interesting topic, since it lies at the origin of phenomena such as the quantum Hall effect, the Aharonov-Bohm effect or topological insulators [17]. Magnetic properties have been directly simulated on BECs of neutral atoms by imposing a geometric Berry phase on the atoms, creating an artificial gauge field [17, 18]. In this quantum Hall regime, spin-orbit coupling within a BEC has been simulated, which could be a stepping stone towards simulational study of superconductors or topological insulators [6, 19].

Another way of using ultra-cold atoms for simulation is the formation and study of arrays of atoms. One way of creating arrays is using an optical lattice in which the atoms are loaded. This is a powerful simulation of the Hubbard model describing physics in solid matter: The periodic Coulomb potential on the electrons induced by the array of atom cores is simulated by standing waves of laser light. The electrons themselves are simulated by the atoms, living in the periodic potential. Mott insulator transitions have been shown for both bosons and fermions [20, 21]. A recently developed powerful tool for the study of quantum gases in lattices is the quantum gas microscope (QGM), where a lattice of strongly correlated particles is imaged and addressed using an objective with single-site resolution [22]. After the first realization of a QGM for Rb atoms in [23], reports of QGMs for other species (Li, K, Yb) have been made [24–28]. Using QGMs, anti-ferromagnetic spin chains have been simulated [29] and the superfluid-to-Mott-insulator-transition has been observed [22, 24].

An alternative way of creating an array of atoms is using optical tweezers instead of a lattice. A far off-resonant beam is strongly focused by a high resolution objective to

create a very small potential well. An interesting feature of the tweezer approach is the ability to nearly deterministically load a single atom into the trap [30]. Multiple traps can be realized using spatial light modulators (SLM) or acousto-optic deflectors (AOD) to modulate the beam that goes into the objective. The number of traps is limited by the range of the SLM or AOD, making the atom numbers for the tweezer case less scalable than for the QGM case, where many atoms could be loaded into the lattice at the same time. The individual control of the potential wells, however, enables sorting of atoms and the synthesis of defect-free chains and even 3D structures of up to 72 single atoms [31–33]. The freedom to choose the arrangement of the single atoms at will opens up many possibilities, some of which will be mentioned here. Many different Hamiltonians can be simulated that could not be formed with a regular lattice. Furthermore, the control of single atoms allows synthesis of single molecules, which could serve as qu-dits [34, 35]. A completely different research line is the synthesis of quantum gates by using Rydberg excitations in combination with the tweezer arrays or by combining multiple atom species in tweezers, and experimental quantum computing options can be explored [36–38].

In our group, we focus on quantum simulation using Sr atoms. Several other groups focus on working with Sr as well [39–41]. Sr is an interesting element for quantum simulation due to its transitions in the spectra where laser diodes are available and the existence of meta-stable states [42]. Furthermore, Sr contains a fermionic isotope that is needed for many quantum simulation experiments. Eventually, we aim to construct a QGM for Sr atoms, but thanks to the versatility of our machine, we have many possibilities for intermediate steps towards this goal. This thesis reports on such an intermediate step: the construction of a tweezer machine for Sr atoms. Much information on the machine itself is presented in an earlier thesis in our group by Alex Urech [43].

1.2 High resolution objectives for imaging quantum gases

An important requirement for both the QGM and the tweezer machine is the availability of a high resolution objective that can be placed outside the vacuum chamber. As the requirements for such an objective are very specific including a high resolution and a long working distance (± 20 mm), previous QGMs ordered their objectives from dedicated companies or, in the case of tweezer setups, the machine was built around a glass cell to make the use of commercial objectives possible [23, 24, 31, 39]. Since adjusting the whole machine was no possibility in the span of this work and ordering a custom made objective is very expensive (at least 10 k€), a high resolution objective is built using commercial lenses only.

Not many designs have been proposed for this purpose in the literature. The previous designs of microscope objectives with a long working distance have reached resolutions of around $1\ \mu\text{m}$ [44–46]. In particular, the design in [46] deserves special attention as they reached a resolution of $1.3\ \mu\text{m}$ using commercial lenses only. In this work, we present a design with a resolution of $0.63(4)\ \mu\text{m}$ built with commercial lenses only. This design has also been used to manufacture the objective with a stacking model for the housing. Testing the objective is performed by measuring the point-spread function of the objective when imaging an illuminated target containing $200\ \text{nm}$ holes. Afterwards, the objective is mounted on our machine to form the tweezer machine. In the tweezer machine, few atoms of Sr have been loaded into the tweezer trap and steps have been made towards detection of single atoms in the tweezer trap. At the time of writing, no reports on single atom detection of Sr have been found in the literature.

1.3 Thesis outline

This thesis consists of two main subjects: building and testing the microscope objective and the tweezer machine for Sr atoms. The chapters 2 to 4 are on the objective, and chapters 5 to 6 report on the tweezer machine.

In chapter 2, the theory of imaging using a high resolution objective is presented and optical aberrations are introduced. The design of the objective is presented in chapter 3, where also the theoretical performance of the objective is explored using the optical aberrations. Chapter 4 is on the experimental results of the objective and comparisons to the theoretical performance are drawn. Chapter 5 elaborates on the theory of obtaining single Sr atoms in a tweezer and chapter 6 reports on the experimental results our tweezer machine obtained.

In the appendices, additional calculations are presented (A and B), a Monte Carlo analysis of the success rate of assembly of the objective is presented (C) and the CAD drawings used in the thesis are presented (D).

Chapter 2

Theory of imaging with a high-NA objective

The field of optics is among the oldest fields of physics and many references exist on the subject such as [47]. Less commonly known is the physics of high-NA imaging when the aberrations of imaging systems start to play a role. In this chapter, the relevant theoretical background of imaging with a high-NA objective will be presented. First, the theory of the paraxial approximation is discussed and the Gaussian beam is introduced. This is the framework on which much the rest of the work is based. In section 2.2 then, the validity of using the paraxial approximation at higher values of the NA is discussed. In section 2.3, the resolution and point spread function of an imaging system are defined and in section 2.4 the aberrations resulting from imperfections in the system and leaving the regime in which the paraxial approximation holds, are discussed.

2.1 Paraxial approximation and Gaussian beams

When imaging objects that are not large compared to the wavelength of the imaging light, the ray optics picture of light fails. In this regime, the wave behavior of light has to be taken into account. This means describing light as a complex wavefunction $U(\mathbf{r}, t)$ that satisfies the wave equation:

$$\nabla^2 U - \frac{1}{c^2} \frac{\partial^2 U}{\partial t^2} = 0. \quad (2.1)$$

General solutions of (2.1) have the form

$$U(\mathbf{r}, t) = A(\mathbf{r}) \exp(i\phi(\mathbf{r})) \exp(i\omega t), \quad (2.2)$$

where $A(\mathbf{r})$ is the amplitude, $\phi(\mathbf{r})$ the phase and ω the angular frequency of the wavefunction. In the rest of the analysis, we will neglect the time-dependent part of the wavefunction and only care about the spatial dependence. Surfaces of equal phase $\phi(\mathbf{r})$ are called wavefronts. When a wave gets transmitted through an optical component (e.g. a lens), the phase $\phi(\mathbf{r})$ changes as a function of the refractive index of the material and the thickness of the material. The phase shift deforms the wavefront and the evolution of this determines the shape of the emerging beam.

To simplify calculations in optics, often the paraxial approximation is used. The paraxial approximation in the wave picture of light is the assumption that the amplitude $A(\mathbf{r})$ of a wave travelling in the z -direction varies slowly within the distance of a wavelength $\lambda = 2\pi c/\omega$:

$$\frac{\partial A}{\partial z} \ll kA, \quad (2.3)$$

where $k = \omega/c$ is the wavenumber. This limit is reasonable for most laser beams and only breaks in strongly focused beams. In the paraxial limit, (2.1) can be rewritten for a plane wave to the paraxial Helmholtz equation:

$$\frac{\partial^2 A}{\partial x^2} + \frac{\partial^2 A}{\partial y^2} - i2k \frac{\partial A}{\partial z} = 0. \quad (2.4)$$

A special solution of (2.4) is the case of the Gaussian beam [47]. The Gaussian beam is often used as a model to describe the TEM₀₀ mode of laser beams [48]. Also in this work, many calculations are based on the parameters derived from assumption of a Gaussian beam. The wavefunction for a Gaussian beam traveling in the z -direction is given as:

$$U(\mathbf{r}, t) = U_0 \underbrace{\frac{w_0}{w(z)} \exp\left(-\frac{\rho^2}{w^2(z)}\right)}_{\text{I}} \underbrace{\exp\left(-ikz - ik\frac{\rho^2}{2R(z)} + i\zeta(z)\right)}_{\text{II}} \underbrace{\exp(i\omega t)}_{\text{III}}, \quad (2.5)$$

where $\rho = \sqrt{x^2 + y^2}$, U_0 is the amplitude of the wavefunction at the focus and $w_0 = \sqrt{\frac{\lambda z_R}{\pi}}$ is the waist of the beam at the focus. In the definition of w_0 , z_R is the Rayleigh length, which is the distance Δz from the focus at which the intensity of the beam is halved. Furthermore, in (2.5), $w(z) = w_0 \sqrt{1 + (z/z_R)^2}$ describes the evolution of the waist of the beam along the z -direction, $R(z) = z(1 + (z_R/z)^2)$ is a measure of the radius of curvature of the beam and $\zeta(z) = \tan^{-1} \frac{z}{z_R}$ describes a phase retardation accounting for the Gouy effect [47].

As mentioned in (2.5), the wavefunction of the Gaussian beam can be split into three parts: part I describes the evolution of the amplitude in the spatial directions; part II describes the complex phase of the wave and part III describes the time evolution. In

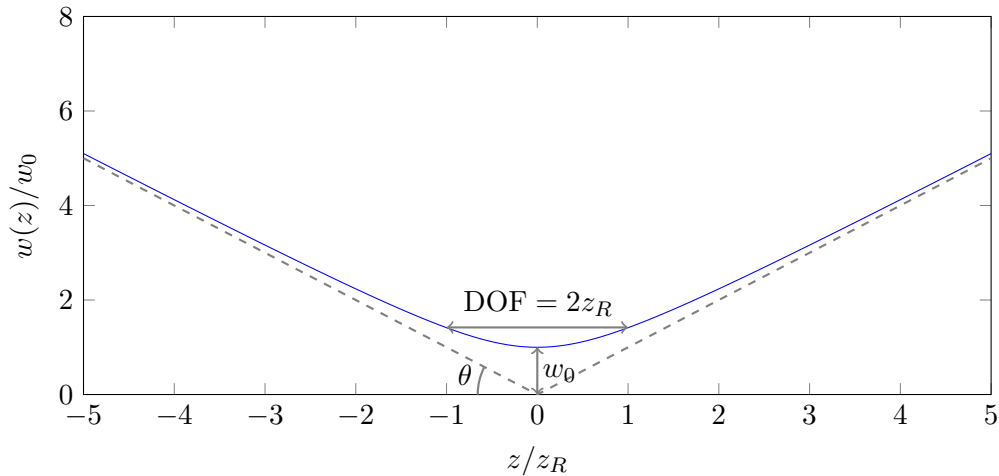


Figure 2.1: The evolution of the waist $w(z)$ with the most relevant parameters for the Gaussian beam. The blue line is the plot for $w(z)$. The divergence θ is given as the angle of the linear asymptote given by the gray dashed line. The depth-of-focus (DOF) is given as twice the Rayleigh length z_R .

part I, it can be seen that the amplitude of a Gaussian beam evolves both in the z -direction following $w(z)$ and in the x - and y -directions as a decaying exponential (hence the name Gaussian). The waist $w(z)$ is defined at each position z as the distance from the optical axis where the value of the intensity resulting from this exponential decay has dropped by a factor of $1/e^2$ and can be taken as a measure of the beam width. In figure 2.1, a schematic plot of the waist $w(z)$ for a Gaussian beam is shown. The waist has a minimum at the focus at $z = 0$. From the definition of $w(z)$ and figure 2.1, it can be seen that a Gaussian beam is always converging or diverging when not in focus. Far away from the focus, this behavior is linear and the beam diverges under an angle:

$$\tan(\theta) = \frac{w_0}{z_R}. \quad (2.6)$$

Since we work in the regime of the paraxial approximation, the above expression can be simplified to:

$$\theta \approx \frac{w_0}{z_R}. \quad (2.7)$$

Collimating a Gaussian beam then means increasing the value of z_R with respect to w_0 such that the divergence is almost zero.

Adjusting the beam shape of a Gaussian beam can be done by placing an optical system such as a lens or objective in the beam path. An optical system with magnification M in the beam path introduces a phase shift and as a consequence of that deforms the wavefront. The emerging beam is thus also Gaussian, but with a modified waist w'_0 and Rayleigh length z'_R . The position of the focus of the beam z_0 is also shifted along the

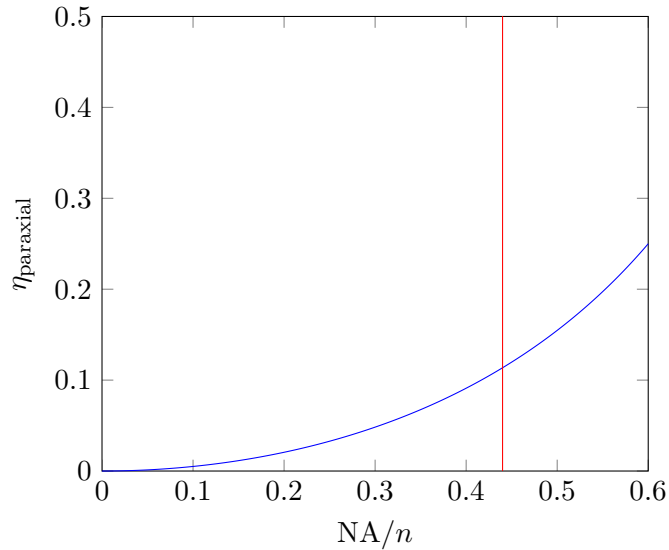


Figure 2.2: The blue line is the relative error η_{paraxial} that arises when taking the paraxial approximation for different values of NA/n . The red line is the value of $NA/n = 0.44$, which is the maximum value in this work.

optical axis to a place z'_0 . The expressions for w'_0 , z'_R and z'_0 are given in terms of M by:

$$w'_0 = Mw_0 \quad (2.8)$$

$$z'_R = M^2 z_R \quad (2.9)$$

$$z'_0 = M^2 z_0. \quad (2.10)$$

These results are important and will be used throughout the rest of work in various calculations. The full derivation for (2.8) and (2.9) can be found in [47]. For the position of the waist, a derivation based on ray transfer calculations is presented in appendix A.

2.2 Validity of the paraxial approximation

Although the description of the Gaussian beam leads to measurable quantities, it is only valid within the limits of the paraxial approximation (2.3). At this point, it is convenient to define the numerical aperture of a beam as:

$$NA = n \sin(\theta), \quad (2.11)$$

with n the refractive index of the medium. Using (2.11), the expression (2.6) for the divergence of the beam can be rewritten as:

$$\begin{aligned}\frac{\cos(\theta)}{\sin(\theta)} &= \frac{z_R}{w_0}, \\ \sqrt{1 - \sin^2(\theta)} &= \frac{z_R}{w_0} \sin(\theta), \\ \sqrt{1 - \frac{\text{NA}^2}{n^2}} &= \frac{z_R \text{NA}}{w_0 n},\end{aligned}\tag{2.12}$$

where the paraxial approximation can be used to expand the square root to only the zeroth term to retrieve (2.7). Furthermore, (2.12) also gives a limit for the paraxial approximation in terms of the NA:

$$\frac{\text{NA}}{n} \ll 1.\tag{2.13}$$

In this work, the NA of the beam will go as high as 0.44 and n will be taken in air or vacuum, such that the condition (2.13) is no longer a priori valid. Therefore, it is important to analyze the error induced by taking the paraxial approximation. The relative error is defined as:

$$\eta_{\text{paraxial}} = \frac{1 - \sqrt{1 - x^2}}{\sqrt{1 - x^2}}, \quad x = \frac{\text{NA}}{n}.\tag{2.14}$$

In figure 2.2, the relative error of the approximation is plotted. At $\text{NA}/n = 0.44$, it can be seen that the relative error induced by taking the paraxial approximation is around 0.11. This means the paraxial approximation for such NA does not hold well. Leaving the regime of the paraxial approximation means higher order terms have to be included leading to aberrations, which are discussed in section 2.4.

2.3 Resolution and the PSF of an imaging system

Up to this point, no limitations have been set on the waist w_0 of a beam and it might seem to be possible, using a perfect lens, to focus a beam to an infinitely small spot. In reality this is not possible, due to the wave nature of light, which leads to diffraction. Due to time-reversal symmetry of the system, this also gives a limit on the smallest spot that a lens with a given NA can image. The image that an imaging system produces when imaging a perfect point source is called the point spread function (PSF). The PSF of a perfect imaging system is a diffraction pattern of a circular aperture with a finite radius a . This diffraction pattern is called the Airy disk, an image of which is shown in

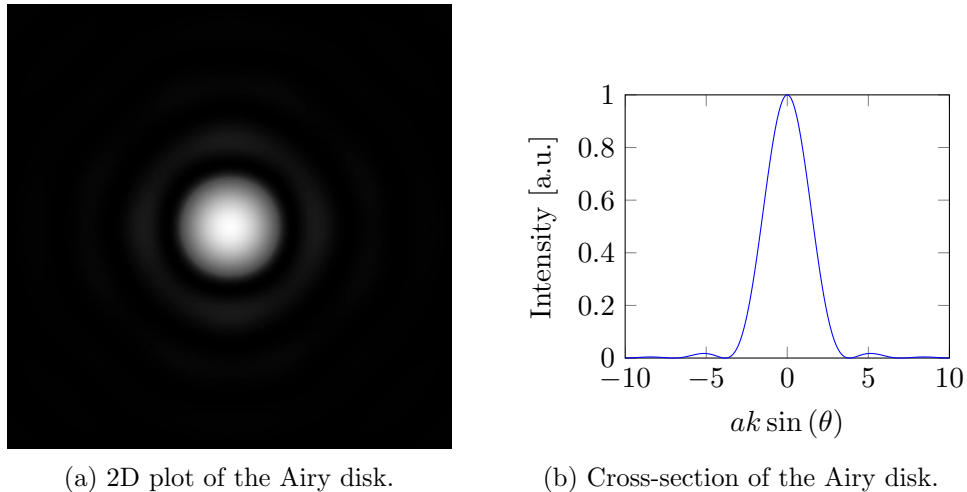


Figure 2.3: The PSF of a perfect imaging system is the Airy disk. (a): A 2D plot of the Airy disk. White denotes higher intensity. (b): A cross-section of the PSF.

figure 2.3a. The intensity of the Airy disk is given by [49]:

$$I(\theta) = I_0 \left(\frac{2J_1(ak \sin(\theta))}{ak \sin(\theta)} \right)^2, \quad (2.15)$$

with $J_1(\rho)$ the first-order Bessel function and a the effective radius of the spot. The minimum spot size is determined by the distance from the principal maximum of the Airy disk to the first minimum. The first minimum is found at

$$ak \sin(\theta) \approx 1.22\pi. \quad (2.16)$$

Introducing the NA of the imaging system as given by (2.11), neglecting n and solving for the spot size, we find an expression for diffraction limit a_0 :

$$a_0 = \frac{0.61\lambda}{\text{NA}}. \quad (2.17)$$

Equation (2.17) sets a theoretical diffraction limit of an imaging system with given NA and for a given wavelength λ .

Due to imperfections in an imaging system, the imaged spot size of a point source can be larger than the theoretical minimum presented in (2.17). From the PSF again a resolution r_0 can be determined by taking the distance from principal maximum to first minimum. When r_0 is at the theoretical minimum, the resolution of an imaging system is said to be diffraction-limited. The value of r_0 allows us to give a definition of the maximal achievable resolution of an optical system: two spots that are separated more than r_0 are said to be resolved and two spots are not resolved if the separation is less

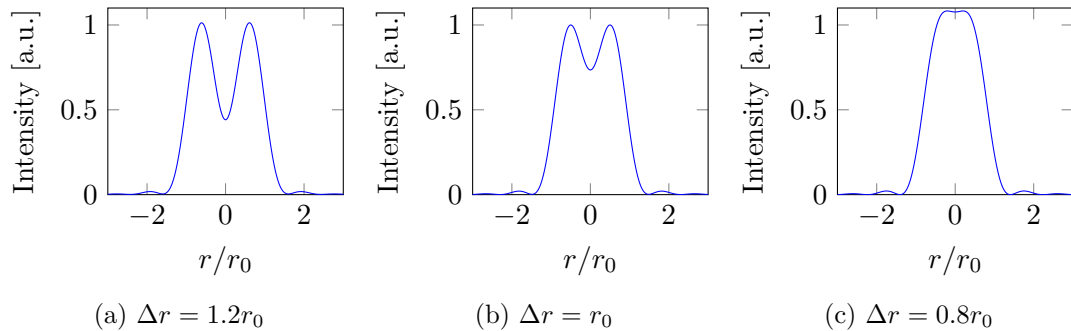


Figure 2.4: The imaged intensity (in arbitrary units) of two identical point sources for varying distance Δr between them. (a): At more separation than the Rayleigh criterion the two sources are distinguishable. (b): At $\Delta r = r_0$, the sources are just distinguishable. (c): At lower separation, the sources are not resolved anymore.

than r_0 . This is called the Rayleigh criterion for the resolution. A plot of the Rayleigh criterion is shown in figure 2.4.

Since the PSF of an imaging system usually contains imperfections, fitting (2.15) to a dataset can deliver unsatisfactory results, mostly when the rings of the Airy disk are deformed by aberrations, to which the Bessel function is sensitive and a Gaussian function is not. Often, a Gaussian approximation to (2.15) is used in that case [50]. When a Gaussian is fit to a perfect Airy disk, the best fit yields

$$\sigma_{\text{fit}} = 0.21 \frac{\lambda}{\text{NA}}, \quad (2.18)$$

for the standard deviation σ of the Gaussian function. Combining this expression with (2.17) gives us an expression for the resolution when a Gaussian fit to the PSF is performed:

$$r_0 \approx 2.9\sigma_{\text{fit}}. \quad (2.19)$$

In this work, we will also use the Gaussian approximation as we are only concerned about the resolution given by the spot size r_0 .

It is important to note that the PSF is an inherent property of the imaging system. Every image taken with the imaging system gets blurred by the convolution of the object with the PSF. When imaging spots of finite size that are close to the resolution r_0 this blurring effect is significant and has to be accounted for by deconvolution of the image with the measured PSF of the imaging system [51]. In the relevant case of Gaussian approximations, the deconvolution is expressed as

$$\sigma_{\text{object}} = \sqrt{\sigma_{\text{image}}^2 - \sigma_{\text{sys}}^2}. \quad (2.20)$$

The derivation for this is presented in appendix B.

2.4 Optical aberrations

Optical aberrations arise when the paraxial approximation fails, because off-axis points and greater divergences start playing a role. This makes that for high-NA imaging systems the optical aberrations are limiting in reaching the diffraction-limit. The theory of optical aberrations has been studied extensively in a few good references where also calculations for the wavefront distortions per aberration are presented [52, 53]. In our case, the aberrations do not have to be quantized so here only the qualitative effects of the aberrations are shown and the ways of compensating are discussed.

The most obvious aberration is defocusing of the imaging system, discussed in subsection 2.4.1. The most important other monochromatic aberrations are spherical aberration, coma and astigmatism. Those are the topics of subsections 2.4.2-2.4.4. In subsection 2.4.5, the chromatic aberration when introducing multiple wavelengths is discussed. Using the program Aberrator by Cor Berrevoets illustrations are made for each of the monochromatic aberrations [54]. Those are presented in figure 2.5. Since the aberrations can be seen as phase shifts resulting in errors on the wavefront of the beam, the aberration is given in units of the period λ .

2.4.1 Defocus

When the imaging plane is not within the depth of field (DOF) of an imaging system, an image is said to be defocused. The result of the defocus on the spots can be seen in figures 2.5a-2.5d. The DOF of an imaging system is often given as twice the Rayleigh length:

$$\text{DOF} = 2z_R. \quad (2.21)$$

Let us now take the example of a diffraction-limited imaging system. Using the definition of w_0 at (2.5) and (2.17) for the waist, we obtain:

$$\text{DOF} = 0.74 \frac{\pi \lambda}{\text{NA}^2}. \quad (2.22)$$

From (2.22) it becomes clear that focusing a diffraction-limited system becomes quadratically more difficult if the NA goes up. For the case of $\text{NA} = 0.44$ and $\lambda = 461 \text{ nm}$ the DOF is $5.6 \mu\text{m}$.

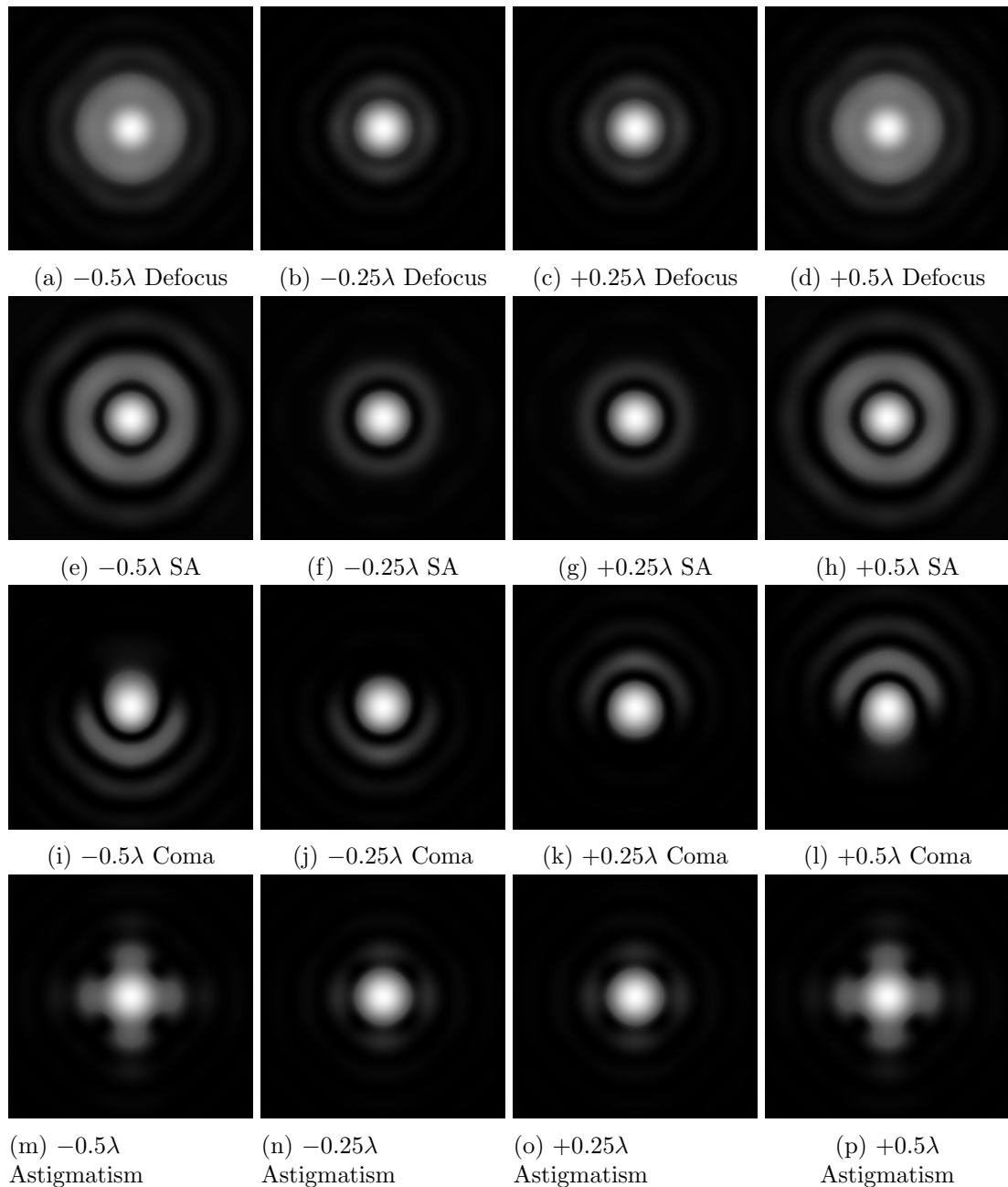


Figure 2.5: Models of the effect of different degrees of aberrations on the PSF of a system. Each picture is taken at the position of the focus of the system with no aberrations. (a-d): Defocus causes the the PSF to be blurred in every direction. (e-h): Spherical aberration makes some of the rays originating from the source being not focused at the same focal plane, resulting in an increase in intensity in the rings of the PSF. (i-l): Coma causes an off-axis point to be imaged as having a tail. The direction of the tail depends on the sign of the coma. (m-p): The effect of astigmatism on the PSF is a cross-shaped pattern due to the sagittal and tangential plane being focused at a different focal plane. Illustrations have been made with the Aberrator software made by Cor Berrevoets [54].

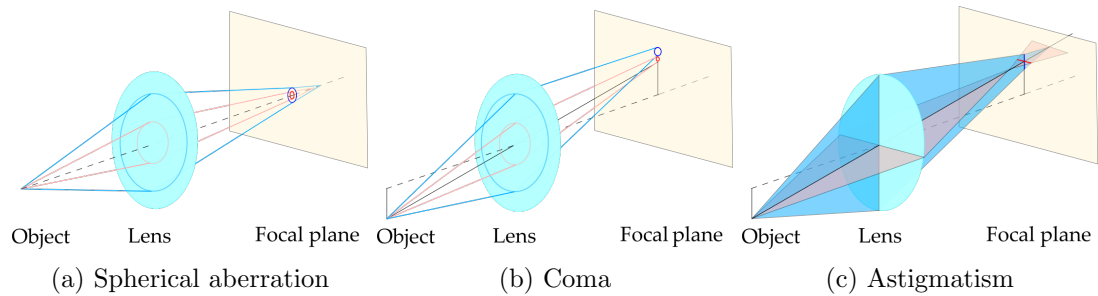


Figure 2.6: Schematic drawings of monochromatic aberrations on a lens. The optical axis is drawn as the dashed line, the lens as the blue oval and the focal plane when no aberrations are present as the yellow plane. (a): the spherical aberration produces a different focus for the paraxial (red) and marginal (blue) rays. (b): Coma causes an off-axis point to be depicted as having a tail. (c): Astigmatism results in the lens having different focal lengths for different rotations of the incoming rays. NB: although differently colored rays are used for clarity of the image, the same wavelength is assumed.

2.4.2 Spherical aberration

Spherical aberration occurs when lenses contain spherical surfaces. It is an on-axis aberration and arises from the higher order on-axis terms that are neglected in the paraxial approximation. In a ray tracing picture, one can say that the on-axis paraxial rays are getting focused on a different spot on the optical axis than the on-axis marginal rays that travel at a higher divergence angle. This is illustrated in figure 2.6a, where the paraxial rays are red and the marginal rays are blue. Spherical aberration can be positive or negative, depending on whether the paraxial or the marginal rays get focused closer to the lens. In figures 2.5e-2.5h, the effect of spherical aberration on the imaged pattern is shown. As the spherical aberration increases, the relative intensity of the rings of the PSF grows, but the resolution stays almost the same.

The simplest way of dealing with spherical aberration is placing an aperture in front of the lens and thereby blocking the marginal rays. This would however decrease the NA, which makes this method undesirable. There are two other ways of compensating for spherical aberration: introducing aspherical surfaces or compensation with other spherical surfaces. The first solution is the cleanest one, but aspherical surfaces are relatively difficult to manufacture and therefore expensive. The other option is combining multiple elements with spherical surfaces so that the spherical aberrations cancel out. Including multiple elements makes alignment of the elements more demanding and the additional surfaces create losses in the system.

2.4.3 Coma

Coma is the effect where rays from an off-axis source cannot be focused like the rays from an on-axis source. An illustration of the coma can be found in figure 2.6b. Neither the paraxial (red) nor the marginal (blue) rays coming from off-axis sources are focused in the focal plane and they also cross the focal plane in different locations. Depending on the type of coma, the rays that pass the lens more to the edge are more defocused than the ones that pass through the center.

An image with coma has a typical tail-like pattern, as shown in figures 2.5i-2.5l. In the PSF, coma is visible as an asymmetry in the wings, where one side is elongated and the other side is compressed. The origin of the coma lies in the misalignment of the imaging system (such that the sources become off-axis) or in errors in the surfaces. The degree of misalignment that an imaging system can have is given by the field of view (FOV). Placing the object in the center of the FOV drastically reduces and for a well-aligned imaging system eliminates the coma. Further compensation for the coma can be done by matching the surfaces of the optical elements to cancel out the errors in the individual surfaces. This matching not only involves the shape of the elements, but also the individual alignments and tilts.

2.4.4 Astigmatism

Astigmatism is also an off-axis aberration like coma, but it can also occur as an on-axis aberration if the imaging system is not rotationally symmetric around the optical axis. Instead of the divergence of the rays coming from the off-axis point like in coma, now their angular orientation is the parameter that makes the rays focused to a different spot on the focal plane. This is illustrated in figure 2.6c, where the red plane corresponds to the sagittal plane and the blue plane to the tangential plane. The effect of astigmatism on the imaged spot is modelled in figures 2.5m-2.5p. It can be seen that the pattern gains the shape of a cross, which is typical for the different focal lengths of the sagittal and tangential plane.

Correcting for astigmatism can be done by placing the object into the FOV of the imaging system. In addition to that the placement of the individual elements of the imaging system can reduce the asymmetry in the system as a whole.

2.4.5 Chromatic aberration

Chromatic aberration arises from the difference in the dispersion relation of the material for light at different wavelengths. This causes the imaging system to have a wavelength dependent focal length. Correcting for chromatic aberration is done by the introduction of doublets in which the two lenses compensate the chromatic aberration of the other. For cold atom purposes, the objective is usually used to address a single transition at high resolution and the resolution for the other wavelengths is of lesser importance. In our case, the objective only needs to have a high resolution for the imaging transition at $\lambda = 461$ nm and the $\lambda = 532$ nm light used to create our tweezer traps.

Chapter 3

Building a high resolution objective with commercial lenses

In this chapter, the process of designing and building the objective is described. The main goal was to design the objective using a set of commercial lenses, in order to keep the manufacturing costs low. The considerations in picking the lens design are described in section 3.1. When working with commercial lenses, a high quality of the lenses is not guaranteed and the tolerances on the lenses has to be taken into account. The predicted tolerances on the lens design and lenses themselves are discussed 3.2. Additionally, the results of a Monte Carlo simulation for the success rate of assembly are discussed. The full results of the Monte Carlo analysis can be found in appendix C. In section 3.3, the housing of the lenses and its features are presented. CAD drawings of every piece used in this thesis can be found in appendix D. In the last section, a set of steps taken to assemble the objective is presented.

3.1 Lens design

The two main requirements the lens design has to fulfill is having a high resolution of around 600 nm and having a long working distance of more than 18 mm. The high resolution requirement originates from the eventual goal of the objective of being part of a QGM. To resolve single lattice sites the resolution has to be on the order of the planned lattice constant of 532 nm. Imaging of Sr is performed on the broad $^1S_0 \leftrightarrow ^1P_1$ line with a wavelength of 461 nm. Using (2.17), the required NA of the objective can be determined to be 0.53 for a 532 nm resolution. When deconvolution is considered, a slightly lower resolution and NA could suffice and we expect a resolution of around 600 nm to be high enough [24]. The objective has to be mounted outside the vacuum chamber, so the

#	Lens name	Manufacturer	$\text{\O}(\text{mm})$
1	LAM-459 ¹	Melles Griot	18.0
2	LE1076	Thorlabs	50.8
3	LE1418	Thorlabs	50.8
4	KBX-151	Newport	50.8
5	LC1315	Thorlabs	50.8

Table 3.1: The configuration used to create our objective. For each lens the name, diameter and manufacturer is given.

objective cannot be placed close to the atoms making the first requirement of the high resolution harder to meet.

The working distance of an objective is defined as the optical distance between the center of the first lens and the object. In the microscope chamber of our machine, the atoms are 10 mm away from the 3.125 mm thick fused silica viewport. Because the first lens is a meniscus lens, its center needs to be at least 3 mm away from the viewport, giving a total working distance of at least 18 mm. An additional difficulty introduced by placing the objective outside the vacuum chamber is the refraction of light that happens at the viewport. This gives rise to additional spherical aberration and coma, if the objective is tilted with respect to the viewport, which the objective has to be corrected for to reach the diffraction-limited resolution.

The starting point of our lens design is the design presented in [46]. Their design consisted of four 50.8 mm diameter commercial lenses and yielded a diffraction-limited result for $\text{NA} = 0.36$ over a long working distance. Two adjustments have been made in order to fit our needs. First of all, the model used in [46] has been used for imaging Rb atoms through a 5 mm thick viewport, whereas our experiment focuses on Sr atoms and uses a 3.125 mm thick viewport. The difference in atom species requires using 461 nm light instead of 780 nm. To correct for both the wavelength difference and thinner viewport, the configuration of the lenses has been adjusted. Secondly, to be able to reach a resolution around 600 nm, a higher NA than 0.36 was needed. For this reason, a fifth commercial lens is included in the design.

Modifications of the design are performed using the ray-tracing software OSLO [55]. For a given configuration of the lenses, OSLO is able to calculate the magnitude of the optical aberrations discussed in section 2.4. To get a first order estimation, the position of every lens was taken as a free fitting parameter when minimizing the aberrations. Using these positions, a new lens was included with variable thickness and radii of curvature in front of the design. Optimizing on those variables and looking for a lens in the catalog

¹The LAM-459 model is deprecated.

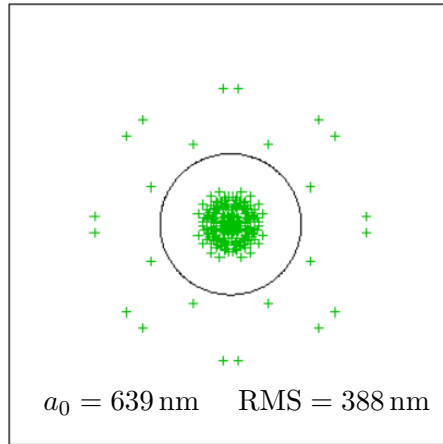


Figure 3.1: Spot diagram created in OSLO. The black circle denotes the diffraction limit, given as a_0 in the image. Since the RMS-value is smaller than a_0 , the system is diffraction-limited.

that matches the value, a design of five singlet lenses was found. The last optimization steps included again fitting for the positions of all the lenses as free parameters and subsequently, fitting for the position of each lens individually while keeping the position of the others locked. Only the position of the first lens was kept free at all iterations, because it served as the refocusing option of the whole objective. The final lens design is shown in table 3.1.

Using OSLO, 500 rays have been traced through the system to form a spot diagram. The rays are initially distributed over the active aperture of the TL-LC1315 lens as a homogeneous field and then traced through every optical surface of the objective and viewport. The final positions in the focal plane form the spot diagram presented in figure 3.1. The RMS value is the variance of the position of the traced rays. The black circle is the calculated diffraction limit, using (2.17). It should be noted the RMS value can be significantly smaller than the diffraction limit, because diffraction is not taken into account during the ray tracing. The design is predicted to be diffraction-limited with $\text{NA} = 0.44$ at a working distance of $10 + 3.175 + 4.94 = 18.1 \text{ mm}$ for 461 nm light. Due to different refractive indices the total optical path length is longer than the working distance with $10 + 3.175 \cdot 1.464 + 4.94 = 19.6 \text{ mm}$. We call this the optical working distance and use this in most calculations.

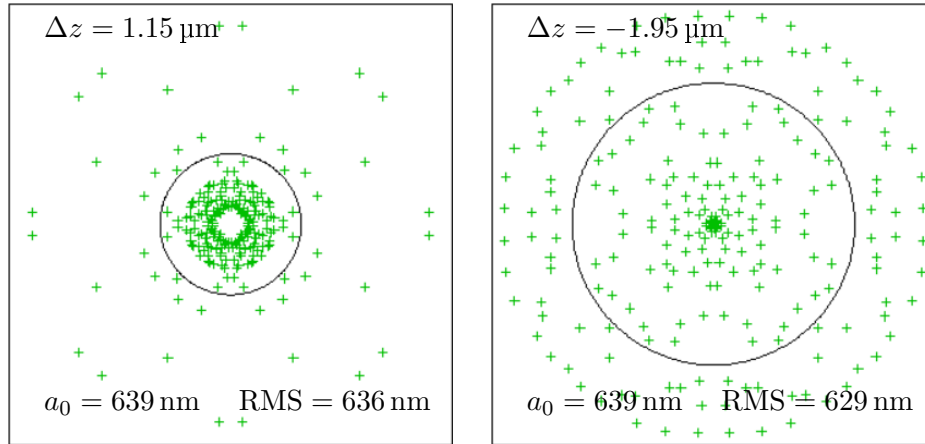


Figure 3.2: Spot diagrams for the defocus of the objective in OSLO. The Δz values in the upper left corner give the amount of defocus.

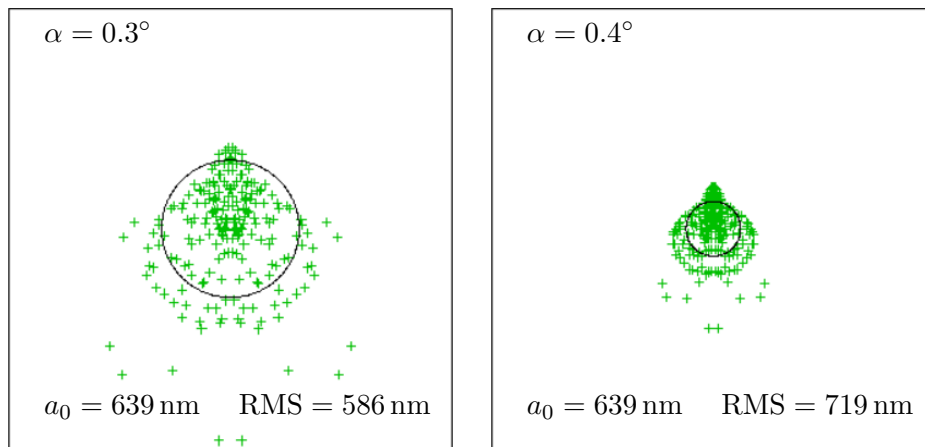


Figure 3.3: Spot diagrams for the objective under an angle α with respect to the viewport.

3.2 Tolerances on the design

The predictions of the previous section only hold in the ideal case, but in the realistic case, when the objective is assembled, lenses will be displaced and tilted and tolerances for these effects have to be investigated. An analysis of the tolerances on the design is performed using OSLO. The tolerances considered are three errors on the placement of the whole objective, presented in subsection 3.2.1, and errors on the placement and manufacturing of the individual lenses within the objective, presented in 3.2.2. In the last subsection, a Monte Carlo analysis for the success rate of assembly is performed using the derived individual tolerances.

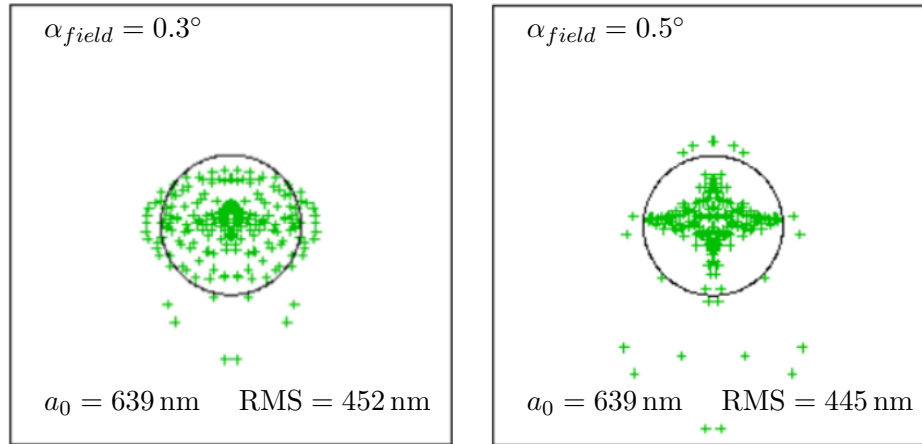


Figure 3.4: Spot diagrams for different field angles α_{field} . At $\alpha_{field} > 0.3^\circ$, the spot pattern becomes distorted, but the RMS value is still less than the diffraction limit.

3.2.1 Tolerances on the placement of the objective

Focusing the objective is modeled by adjusting the distance of the first lens to the viewport, while keeping the other distances constant. For each position, a spot diagram is made and the RMS value is calculated. The spot diagrams for the two distances around the focus at which the resolution is just diffraction-limited are presented in figure 3.2, and give a total diffraction-limited range of $\Delta z = 3.1 \mu\text{m}$. This is on the same order as the theoretically predicted DOF using the Rayleigh range in subsection 2.4.1.

The focusing range of a few μm means that steps of more than $1 \mu\text{m}$ precision are needed to focus the system. This can be achieved with high precision piezo actuators, but these are expensive [24]. Another practical solution is hinted at by (2.10), which gives the scaling between the focus position before and after an optical system with a magnification M . A step in the position of the field lens before the objective results in M^2 less displacement of the focus compared to an equivalent step in the objective position. This change makes the requirements on the precision of the steps a factor M^2 less demanding. The main disadvantage of focusing this way is that it gives rise to spherical aberration by compensation one out-of-focus surface with the other [56].

Using the function OSLO function "TLA" on the first surface of the first lens, a tilt α with respect to the viewport is modeled on the whole system. This induces a coma on the spot diagram as can be seen in figure 3.3. The objective stops being diffraction-limited at angles higher than $\alpha = 0.3^\circ$. To keep the objective within this tilting range, the objective is mounted on a custom made square tilting mount. The width of the mount is 10 cm and the screws have a pitch of 80 threads-per-inch. Assuming a 5° rotation of the screw is possible, which corresponds to about 0.0025° per step.

Modeling the field of view is done by adjusting the angle of the incoming light in OSLO. The range of acceptable angles is called the angular field of view (AFOV) and is related to the spatial field of view in the focal plane as [53]

$$\text{FOV} = 2\text{WD} \tan\left(\frac{\text{AFOV}}{2}\right), \quad (3.1)$$

where WD is the optical working distance of the objective, corrected for the different refractive indices. In figure 3.4, spot diagrams for various incoming field angles have been given. Although the RMS values remain smaller than the diffraction limit for high values of the field angle α_{field} , the spot pattern gains a cross-like shape. Therefore, values above $\alpha_{field} = 0.3^\circ$ are not wanted and $\text{AFOV} = 0.6^\circ$ is taken. Using the optical working distance of 19.6 mm, this results in a FOV of about 200 μm .

3.2.2 Tolerances on the placement of lenses

Each of the lenses can also be displaced individually with respect to its default position in the design. Simulations of the axial displacement, tilt and decenter of the lenses are performed and determine tolerances that serve as requirements on the housing. In each run, the placement of a single lens is adjusted and the remaining lenses are kept at their position. Then, the system is refocused by varying the distance between the first lens and the viewport. The resulting RMS values are presented in table 3.2. The first lens is not included in these runs, because displacements of the first lens can be compensated by moving the objective as a whole.

The objective seems to be robust to axial displacements from the nominal values. Each of the lenses can be displaced over 100 μm without significant loss in performance. Additionally, the position of all lenses can be varied by 90 μm both ways at the same time, while keeping the RMS value below the diffraction limit after refocusing. When assembling the objective, the displacement of one lens can be compensated by deliberately displacing another lens. This has been simulated with the two lenses that are the most sensitive to displacement, TL-LE1076 and TL-LC1315. It was possible to compensate displacements of TL-LE1076 as large as 600 μm both ways, by displacing TL-LC1315. We have taken the tolerance on the position to be 50 μm for each lens.

The design is less robust to the tilts of individual lenses. Especially the biconvex N-KBX-151 lens is sensitive to tilts and has to be placed within 0.03° precision. Tilts are caused by asymmetries in the spacing rings or mounts holding the lens. Given that the lenses have a diameter of 50.8 mm, the 0.03° precision corresponds to the spacing rings having a height difference of 26.6 μm over the course of a 180° rotation. Tilts could also be compensated by adjusting the TL-LC1315 lens, making the maximal allowed tilting

Lens		Axial Displacement					Tilt			Decenter	
Name	f (mm)	Default (mm)	$-200\ \mu\text{m}$	$-100\ \mu\text{m}$	$+100\ \mu\text{m}$	$+200\ \mu\text{m}$	0.03°	0.05°	0.1°	d (mm)	RMS
TL-LE1076	100	9.08	324.9	292.4	495.3	654.5	-	468.4	694.1	0.046	575.3
TL-LE1418	150	5.10	369.9	366.4	361.0	359.2	-	-	539.5	0.069	835.7
N-KBX-151	88.3	1.00	381.8	372.3	356.6	351.3	493.1	664.0	1169	0.040	753.3
TL-LC1315	-75	28.00	351.4	296.8	502.6	671.3	-	-	547.5	0.034	819.2

Table 3.2: The focal spot size RMS radii in nm for the displacements of the individual lenses. The axial displacement, tilt and decenter have been included. For each displacement, the individual lens is adjusted and the remaining lenses are kept at their default values. The focal spot size RMS radius is then determined after refocusing the objective. When the focal spot size RMS radius value exceeds the diffraction limit, the value is colored red.

Tolerance	Estimated Value
Distance	50 μm
Thickness	100 μm
Tilt	0.02°
Decenter	3'

Table 3.3: Summary of the estimated tolerances for the lenses. These are also the tolerances used in the Monte Carlo simulations.

angle for the N-KBX-151 more than 0.05°. To stay within the margin, the tolerance on the angle is taken to be 0.02° for each lens.

The tolerances that are set by the manufacturers for commercial lenses are the center thickness of the lens and the decenter. The thickness has a tolerance of 100 μm . For all the commercial lenses used here the decenter is specified indirectly by stating the wedge angle $\theta < 3'$. Using

$$d = \theta f(n - 1), \quad (3.2)$$

the difference d of the optical and mechanical axis for a specific lens with focal length f and refractive index n is obtained [57]. The values of d for the lenses in this design are given in table 3.2. Decenter is modelled as the radial displacement of the lenses by the distance d . The resulting focal spot size RMS radii indicate that the decenter of the lenses is detrimental to the performance.

To compensate for decenter the radial placement of the lenses can be adjusted. However, in many designs of objectives this is impossible. A second approach involves rotating the lenses such that the optical axis deviates from the mechanical axis in the same direction for each lens. This reduces the relative decentering between the individual lenses and the remainder can be compensated by translating the objective. In the simulations, this method reduced the effect of the decenter drastically. The tolerances on the placement of the lenses in the design have been summarized in table 3.3.

3.2.3 Monte Carlo analysis of the success rate

When assembling the objective the lenses are placed with a random displacement and tilt within the housing. The displacements and tilts might or might not compensate each other, which can be expressed by a success rate of obtaining a diffraction-limited objective. An expected success rate is determined with a series of Monte Carlo simulations using the tolerances from table 3.3. For each lens, a random value for each tolerance is generated assuming a uniform distribution. Compensation variables are defined, which are varied to minimize the aberrations and the focal spot size RMS radius given such

a randomly generated design. Each run consisted of 500 simulations and the success rate is determined by the percentage of designs where the position could be adjusted to being diffraction-limited. The full results of the Monte Carlo analysis can be found in appendix C. In the first run, just the refocusing of the objective is used as a compensation for the errors. This resulted in a probability of around 3% of reaching a focal spot size RMS radius of less or equal to 650 nm. When also the translational x,y-position of the objective was included as a compensation variable, the success rate was increased to around 14%. In reality even more compensation parameters are possible such as the tilt of the objective and the rotation of the lenses, which have not been taken into account in the Monte Carlo analysis, but can only increase the success rate.

3.3 Housing of the objective

The housing of the objective in which the lenses from table 3.1 are placed is presented in this section. The tolerances on the individual placement of the lenses from table 3.3 served as the requirement for the design of the housing. The housing was designed and milled at the workshop of the university. In the process of choosing a housing, a series of designs was considered, which will be discussed in subsection 3.3.1. Additionally, the used material had to be non-conducting and be stiff, while being manufacturable. This is the subject of subsection 3.3.2. In the last subsection, extra features in the design of the housing are explained.

3.3.1 Picking the housing design

In total, three candidate designs were considered for the housing. Our choice in this will be discussed in the following paragraphs. The first design was placing the lenses in a 50.8 mm diameter commercial lens tube. They are held in place inside the tube by locking rings. An adapter piece can hold the first lens as this has a different diameter compared to the other lenses. The main advantage of this design is that the vast majority of the pieces is commercially available; only the adapter piece needs to be manufactured by the workshop. This is a big advantage as it saves both time and expenses. The design contains three major drawbacks. First of all, the thin locking rings that are used in this design have no fixed position but are screwed into the main tube with a standard thread. This highly limits the accuracy of the placement of the lenses and also the stability of the system and it is not guaranteed that we are within the tolerance of 50 μm . Secondly, we would not have the freedom of choosing the material of the housing and finally, there is no possibility of adjusting the placement of individual lenses, without disassembling the whole objective. On basis of these drawbacks, this design is not chosen.

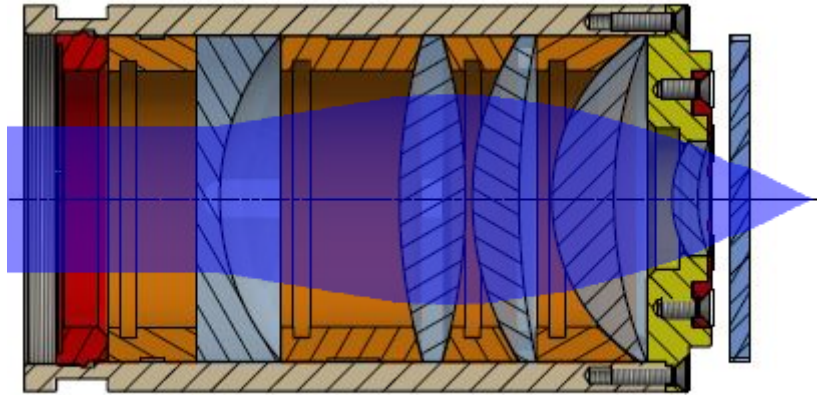


Figure 3.5: Drawing of the design of the objective. The lenses (gray) are held in place by spacing rings (orange). The assembly is held in the outer tube by means of a single locking ring (red). The first lens is mounted in a separate piece (yellow) that at the same time functions as a cap for the outer tube. The blue plate on the right hand side resembles the glass of the viewport. The blue area indicates the path of the light coming from the atoms. The drawing is to scale.

A slightly more sophisticated design is the stacking model, shown in figure 3.5. This design is used in previous works [45, 46] and is also used for the housing in this work. Again, the lenses are directly placed inside an outer tube, but instead of locking rings, non-threaded spacing rings are used. The rings are milled to exactly fit between two adjacent lenses, with a precision well within the predicted tolerance of $50\ \mu\text{m}$. The edges of each ring are milled skewed at appropriate angles to fit the curvatures of the lenses. The whole stack of lenses and rings is held together by one locking ring at the end. The first lens is mounted in a separate piece that at the same time functions as a cap for the bigger tube. This model is more stable than the commercial lens tubes due to the spacing rings and the material can be chosen at will. However, adjusting lenses is difficult and the diameter of the outer tube is determined by the largest lens diameter only. A fluctuation in the diameter of the lenses can thus cause decenter of the smaller lenses. For each lens, three holes have been drilled for the placement of set screws to hold the lens in place and compensate for the decenter.

To completely avoid the problem of different diameters, a poker-chip model can be used [58]. Each lens or a combination of lenses is then assembled first in separate holding pieces before stacking those assemblies in the outer tube. The separate holding pieces can be manufactured to precisely fit specific lenses, correcting for errors in the lenses. The drawback is that making such pieces is significantly more difficult than making the rings needed for the stacking design. These efforts make the design not desirable for the first prototype, but in future versions, this design could prove to be an improvement over the stacking model.

Material	Color	E [GPa]	α [$\cdot 10^{-5} \text{K}^{-1}$]
PEEK Unfilled	Gray/brown	3.1 to 3.8	4.7 to 5.5
MACOR	White	66.9	0.9
Ultem 1000	Light brown	3.2	5.0

Table 3.4: Overview of the properties of candidate materials. The color should be dark to reduce the reflections of stray light inside the objective. E is the tensile modulus of the material, α the linear coefficient of thermal expansion. Data taken from references [60–62].

3.3.2 Building material considerations

The material of the housing is a crucial factor in the stability of the objective. Aluminum is often chosen for its relative strength and ease of machining, also for making the microscope objectives in [45, 46]. In our case, this is impossible, because the objective will be used to image quantum gases and will be placed inside an electromagnetic coil. The magnetic fields produced by the coil will vary during the detection sequence and if the material of the housing conducts electricity, eddy currents will start flowing during those field ramps [59]. Magnetic fields induced by the eddy current could be detrimental for the trapping of atoms and the objective could jitter as a result of induced magnetic forces, decreasing the resolution.

Non-conducting stiff materials include ceramics and thermoplastics. An overview of candidate materials and their properties is presented in table 3.4. These materials were chosen either because our workshop has experience working with it or because a material is used in designs of earlier QGMs [24]. The color of the material is of minor importance, but preferably the material should be as black as possible, because the objective will be used for imaging low intensity sources such as a few atoms and reflections of stray light should be reduced to a minimum. Based on the color alone, none of the materials has a particular preference. For both PEEK and Ultem, black carbon fiber filled versions are commercially available, with only slightly different properties [63].

For stability of the alignment and ease of machining, the tensile modulus is an important material property to consider. The tensile modulus is a measure of the stiffness of the material. MACOR is a ceramic and has the highest tensile modulus. On the one hand this means that a piece MACOR will deform the least once it is made, but on the other hand, milling MACOR is a lot more tedious, since a higher tensile modulus means a more brittle material.

A high value for the linear coefficient of thermal expansion α is unwanted, because fluctuations in the ambient temperature could destroy the alignment of the lenses. For

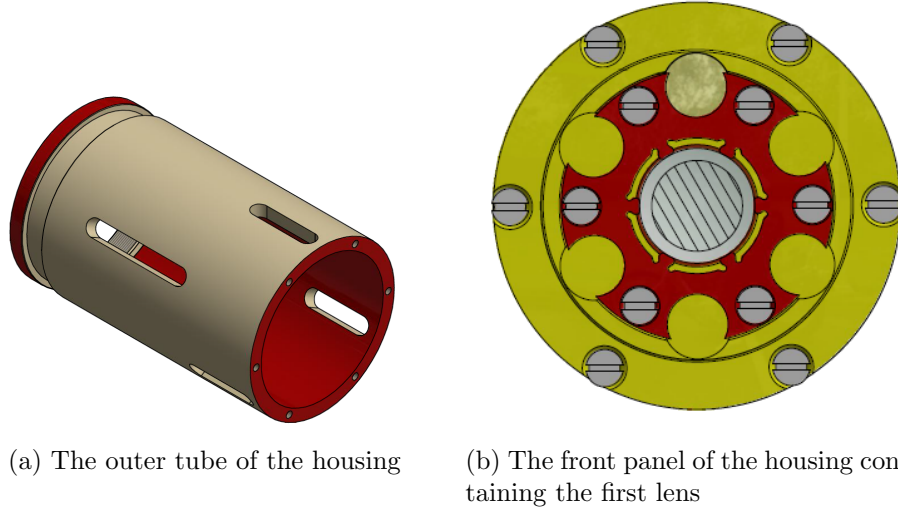


Figure 3.6: Some extra features have been added to the design. (a): Six slits have been milled in the outer tube of the housing. Those serve to move the lenses and rings during assembly and performance optimization. Also the notch for mounting the objective as a whole is visible. (b): The front panel of the objective contains the first lens (center), which is held in place by a red clamping piece. Six wells offer mounting options for small alignment mirrors.

an objective of length L , the expansion can be calculated as:

$$\Delta L = \alpha L \Delta T. \quad (3.3)$$

Temperature fluctuations on the optical table are expected to be within 1 K. For a 10 cm long objective made of PEEK or Ultem, (3.3) then yields $\Delta L \approx 5 \mu\text{m}$. We expect this to be small enough to not cause significant distortions in the alignment, which is supported by the tolerances from table 3.2. Based on this conclusion, the higher brittleness of MACOR and the experience that our workshop has with PEEK, PEEK is chosen as the material for our objective. In the first version of the objective, about which this work reports, the unfilled version of PEEK was chosen, because of its immediate availability in our stock.

3.3.3 Extra features in the design

Since the inner diameter of the tube is made to just fit the diameter of the biggest lens with a difference in diameter of $20 \mu\text{m}$, a small tilt can jam the lens when placing it inside the tube. On top of that, it should be possible to take the assembly apart in case of lacking performance. Therefore, the spacing rings are equipped with a notch, in which a tool can be clamped to pull the spacing rings out. In addition, as can be seen in figure 3.6a, six slits are milled into the outer tube to guide this process. The slits in

the outer tube can also be used to gently push out the lenses, or to manipulate their rotation within the tube. At the position of each lens there are also 3 holes for placing set screws that can hold the lenses in place while rotating and adjusting the position of other lenses. The slits and holes are placed in two groups of three with 120° separation between them, to minimize the deformation of the outer tube.

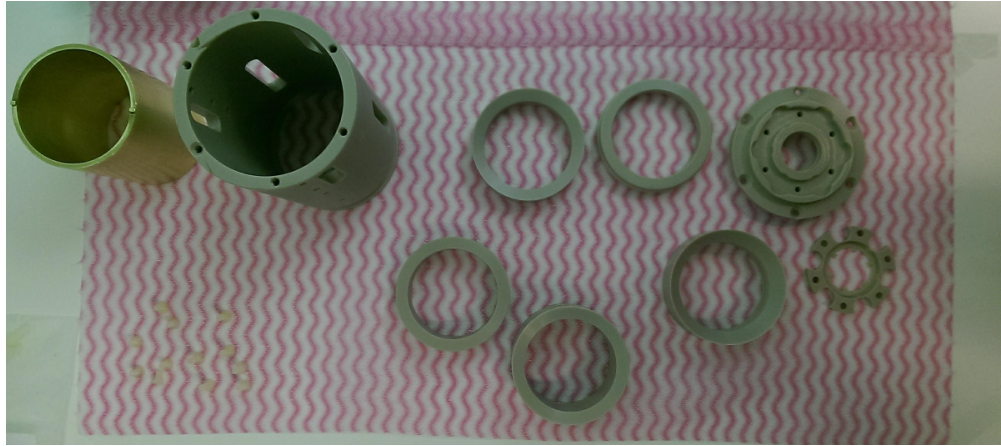
To mount the objective on the machine, the notch on the left hand side of the outer tube is used. Two hemispherical clamping pieces are made to fit precisely inside this notch and are screwed onto a piece that is connected to the remainder of the setup.

In addition to the hole for the lens, six wells of 10 mm diameter have been milled in the panel. Those wells can be used to mount dielectric mirrors that will be used in the alignment of the objective to the vacuum chamber viewport. An illustration of the front panel is given in figure [3.6b](#).

3.4 Assembly procedure

After all of the components had been milled in our workshop, the objective was assembled in a series of steps in a clean environment with filtered air flow. These steps are briefly listed in the following. The objective has been assembled once completely and afterwards the TL-LC1315 lens has been taken out and replaced with a random rotation several times for compensation. This was sufficient to obtain a prototype with satisfactory performance. The whole assembly procedure has not been repeated multiple times afterwards.

1. The PEEK components and lenses are cleaned using high purity ethanol. Ethanol is used instead of acetone to not damage the plastic. An image of the PEEK components is shown in figure [3.7a](#).
2. The front panel is mounted to the outer tube to serve as the cap against which the lenses are stacked. Nylon screws were used to avoid eddy currents in the screws.
3. The TL-LE1076 lens is placed in the tube and its dedicated spacing ring is used to push it through the tube against the front panel.
4. Using a height gauge the distance of the center of the back surface of the lens with respect to the end of the outer tube is measured. A cleaned PEEK tip is placed on the tip of the gauge to prevent it from scratching or leaving dirt on the lens.
5. The previous two steps are repeated for the TL-LE1418, N-KBX-151 and TL-LC1315 and their dedicated spacing rings.



(a) Upper left corner: Outer tube and key for locking ring. Lower left corner: Nylon screws. Middle: Spacing rings and locking ring. Right: Front panel and clamping piece for first lens.



(b) Front view

(c) Side view

Figure 3.7: (a): The PEEK components of the objective. Locations of parts in the caption of the image. (b): Front view of the objective with the small mirror mounted. (c): The side of the fully assembled objective.

6. The stack of elements is tightened in the tube by the locking ring. For small adjustments in lens placement or further tightening, set screws can be placed in the outer tube in the designated holes.
7. The MG-LAM-459 lens is placed in the hole in the front panel. The clamping piece is placed in the front panel using six nylon screws to hold the MG-LAM-459 lens in place.
8. A 5 mm diameter dielectric mirror is placed in one of the dedicated wells and glued in place. A diameter of 5 mm is used instead of the planned 10 mm because of a manufacturing error in the clamping piece on the front panel, which was too thick to contain a larger mirror. The CAD files are correct, however. The front of the objective is shown in figure 3.7b.
9. The objective is now fully assembled. An image of the assembly is shown in figure 3.7c.

Chapter 4

Testing the performance of the objective

In this chapter, the performance of the objective in a test setup is presented and compared to the expected values from chapter 3. Mounting and aligning the objective on the main machine is a job that takes a couple of days if not weeks. In the mean time, it is impossible to do other measurements, as the optical access to the atoms is blocked. On top of that, it would be highly inconvenient if the objective turned out to be not performing well only after the whole process of mounting it on the main machine. Therefore, the objective was first tested as much as possible in a separate test setup outside the machine. First, the test setup is briefly discussed in section 4.1. The results and analysis of the measured PSFs are given in section 4.2. Additionally, measurements for the FOV, DOF and the resolution at other wavelengths have been performed. Those are reported in section 4.3.

4.1 Test setup outside the machine

The test setup outside the machine is designed to measure the PSF of the objective. As discussed in section 2.3, the resolution can be obtained from the PSF as the distance from principal maximum to the first minimum. To measure the PSF of the objective one needs a point source to image.

4.1.1 Creating point sources of light

A finite size source can be considered a point source if the size is significantly smaller than the resolution of the imaging system. The resolution in our case is expected to be

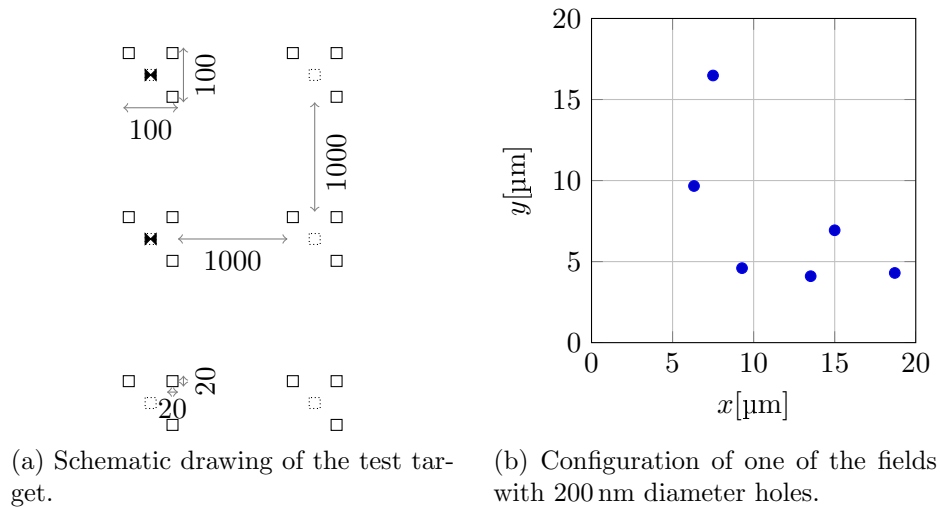


Figure 4.1: (a): Schematic drawing of the test target. Measures are in μm . Not to scale. The target consists of six fields of $100\ \mu\text{m} \times 100\ \mu\text{m}$, each with three $20\ \mu\text{m} \times 20\ \mu\text{m}$ markers in the corner. In the middle of each field a $20\ \mu\text{m} \times 20\ \mu\text{m}$ field containing six holes is located. The two filled fields have $100\ \text{nm}$ diameter holes, whereas the others have diameter $200\ \text{nm}$. (b): The configuration of the holes of the field that is most used in the measurements. Diameter is $200\ \text{nm}$ for this field.

$639\ \text{nm}$ when using $\lambda = 461\ \text{nm}$. Hence, a light source that is $100\ \text{nm}$ or $200\ \text{nm}$ large is small enough to be considered a point source for the objective, but sufficiently large to emit enough light to make sampling time short and obtain a good signal-to-noise ratio.

The most common ways to obtain small light sources are fluorescent beads, SNOM fiber tips and pinholes. The fluorescent beads are microspheres of diameters that can be as small as $20\ \text{nm}$ that are prepared on a glass slide. The fluorophore is pumped with an excitation laser and the beads will start to fluoresce. The excitation laser needs to have a wavelength that is smaller than that of the fluorescence. In our case of $461\ \text{nm}$ light, this requires an excitation laser at $430\ \text{nm}$ and such a laser was not available in our lab. In addition, the fluorescence of the beads is broadband, which causes chromatic aberrations for which the objective is not corrected. SNOM fiber tips are conically shaped fiber tips with a small aperture at the apex of the cone. Commercially available are tips with an aperture diameter of $100\ \text{nm}$ on a fiber that is suitable for $461\ \text{nm}$ light. The tips are, however, expensive and quite fragile [64]. Therefore, the light source in this setup is formed by illuminating a pinhole.

The smallest commercially available pinholes have $1\ \mu\text{m}$ diameter, which is too large to serve as a point source. Fortunately, we were able to obtain a suitable test target from ETH Zürich¹, where it was made by a focused ion beam. A schematic drawing of the target is presented in figure 4.1a. The test target consisted of six fields of $100\ \mu\text{m} \times$

¹We thank Joakim Reuteler for the manufacture of the test target.

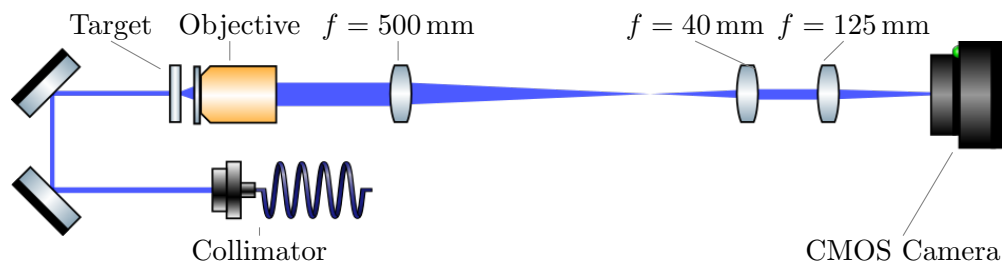


Figure 4.2: Schematic drawing of the test setup used. The target, objective and 500 mm lenses are mounted on translation stages. Drawing is not to scale.

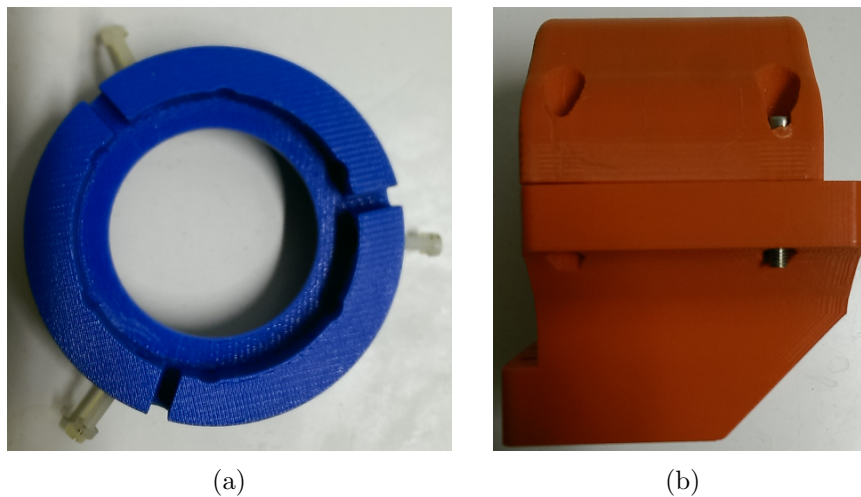


Figure 4.3: The 3D-printed mounting pieces for the viewport onto the objective (a) and the objective itself (b).

100 μm , each marked with three 20 $\mu\text{m} \times 20 \mu\text{m}$ markers in the corners. In the center of each field there is a 20 $\mu\text{m} \times 20 \mu\text{m}$ area containing six pinholes with diameters 100 nm or 200 nm, depending on the field. The positions of the pinholes in the central areas is chosen to be random, in order to avoid the Talbot effect [47]. The pattern for the field that is used in the vast majority of the measurements is presented in figure 4.1b.

4.1.2 Complete test setup

The PSF of the objective is measured by imaging the diffraction pattern of the illuminated target through a substitute viewport. It is important that the thickness and refractive index of the viewport are the same in the test setup as on the main machine, because the modeled performance of the objective depends heavily on the viewport. Ideally, the same viewport would have been used, but no spare piece was available and a substitute viewport had to be used. The substitute viewport is also made of fused silica and its thickness is measured to be 3.20(10) mm, which is almost identical to the 3.175 mm thick fused silica viewports on the main machine.

The setup consists of an optical rail on which the objective with viewport, the target and several imaging lenses were mounted. A schematic of the setup is given in figure 4.2. Since the target, viewport and first lens of the objective have to be placed within 18.175 mm, two special mounting pieces needed to be designed. Both the pieces were 3D-printed for easy and cheap fabrication. Figure 4.3 shows an image of both pieces. The blue piece is designed to hold the viewport and attach it to the objective. The viewport and the blue piece itself are held in place by 3 setscrews each. The red piece is the piece that holds the objective (with the viewport mounted on it). It is essentially a V-block aimed to minimize tilts of the objective.

The outgoing beam from the objective is magnified and projected onto the camera by a series of lenses. The field lens is an achromatic doublet with focal length $f = 500$ mm. To further magnify the image, an $f = 40$ mm and an $f = 125$ mm achromatic doublets are used in a telescope configuration. Given that the effective focal length of our objective is 25.3 mm, this results in a total magnification of 61.8. The diffraction limit of 639 nm for 461 nm light is then projected onto the camera as a circle with a radius of 39.5 μm . The camera is a CMOS camera (BlackFly BFLY-PGE-23S6M-C) with a pixel size of 5.86 μm , meaning that the image is oversampled by roughly a factor 6. Oversampling makes fitting the PSF more accurate. On the other hand, the oversampling leads to fewer photon counts per pixel, so makes the relative contribution of the electronic noise of the camera larger. In this test setup, this is no problem, since the power of the light illuminating the target can be increased at will.

In order to properly focus the objective, we use four translation stages. The first two stages are for the x,y-translation of the test target. This makes it possible to sweep through the FOV of the objective. The other two stages are placed in the z-direction on both the objective and the field lens. The translation stage on the objective is used for coarse focusing, but the minimal movement of 10 μm is too large for finer focusing. For that the stage on the field lens is used. As can be seen from the relation given by equation (2.10), moving the field lens 10 μm corresponds to shifting the focal plane of the objective by 0.026 μm .

4.2 Resolution of the objective

Using the test setup described in section 4.1, the PSF of the objective was measured for 461 nm light. The 461 nm light is of special importance since it will be the imaging wavelength and has been the baseline of the performance in chapter 3. Figure 4.4 shows the raw image on the camera after focusing the system. The six spots are clearly visible and up to four rings can be observed per spot. When compared to the ideal Airy disk in

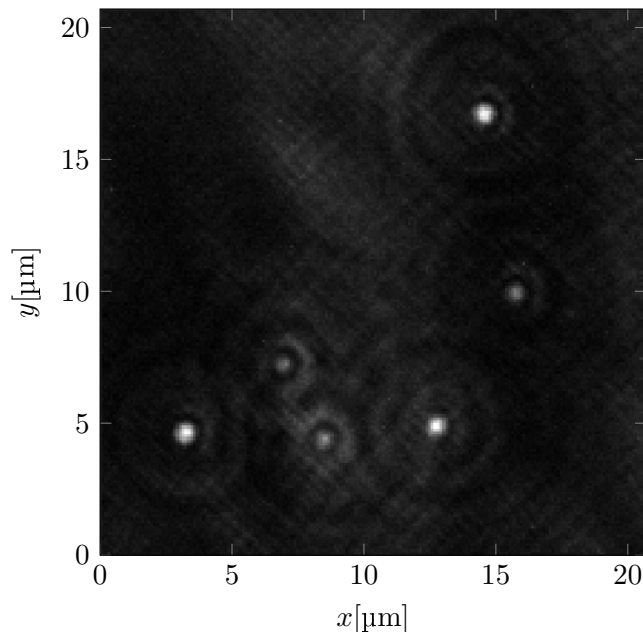
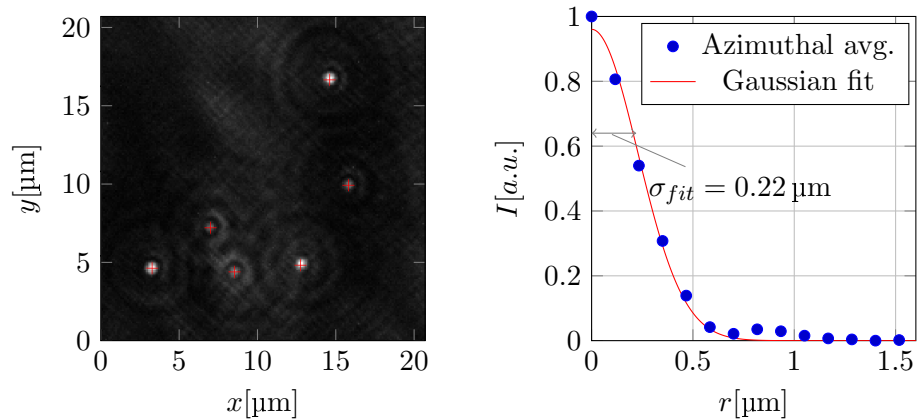


Figure 4.4: The six spots of the field shown in figure 4.1b viewed through the objective. For each spot a diffraction pattern with up to four rings can be observed.

2.3a, the rings in this image are rather bright compared to the center, which is a signal of spherical aberrations present in the system. Since the spots are placed relatively close together, the fringes of the diffraction pattern of some of the spots overlap with each other, giving rise to distortions in the pattern.

There are several types of noise superimposed on the diffraction patterns. The background intensity is observed to fluctuate over a period of around $10\ \mu\text{m}$. This results in some spots being illuminated more than others. This fluctuation also varied with time. We expect this to be an effect of the relatively low quality CMOS camera used in the experiment. A second pattern that can be observed is a set of diagonal fringes with a period of around $1\ \mu\text{m}$. These are due to an artifact of the design. The markers on the test target are placed close to the field of interest and the diagonal fringes come from the diffraction pattern of the markers.

The observed diffraction patterns are analyzed to obtain the resolution of the objective. Using a Laplacian of Gaussian detection method, the blobs in the images that correspond to the centers of the holes are detected [52]. These are marked as the crosshairs in figure 4.5a. The Laplacian of Gaussian detection is used because of its fast performance compared to fitting 2D Gaussians. The pattern of the centers is the pattern used in figure 4.1b. The image is then calibrated by calculating the distance between the centers of two spots i and j and comparing this to the value in μm in the known pattern of holes in the target to obtain a calibration factor for that distance. This is repeated



(a) Crosshairs depicting the detected centers.

(b) Fitted azimuthal average of the PSF for a single point.

Figure 4.5: Analysis of the objective's resolution. (a): Using a Laplacian of Gaussian algorithm the centers of the spots is detected and marked with red crosshairs. (b): An azimuthal average of the intensity of a single point. The red line shows a Gaussian fit through the data resulting in $\sigma_{fit} = 0.22 \mu\text{m}$, which corresponds to a resolution of $r_0 = 0.639 \mu\text{m}$.

for every combination i, j . The average of the 15 possible calibration factors is taken as the calibration of the image and the standard error of the calibration is defined as the standard deviation of the set of calibration factors. At the center of each blob, an azimuthal average is taken to increase the signal-to-noise ratio. Subsequently, a Gaussian function is fitted to the radial profile to obtain a resolution for each of the spots. The Gaussian fitting function is given by

$$I = I_0 \exp(-r^2/(2\sigma^2)) + a, \quad (4.1)$$

where I_0 is the amplitude, usually taken to be 1, r is the radial distance from the center, σ is the standard deviation and a is an offset of the function. The Gaussian function was found to fit better than a Bessel function like (2.15). The better fitting performance of the Gaussian function can be explained by the spherical aberration in the system. Due to the spherical aberration the rings around the central peak get broadened and more pronounced, which influences the fit of a Bessel function much more than the fit of a Gaussian function.

The resolution is obtained from the Gaussian fit using relation (2.18). The fit result for one of the spots is shown in figure 4.5b. The average of these fit results is taken as the resolution and the standard error is determined by the standard deviation of the sample. In the case of figure 4.5a, this calibration was found to be $9.23(6) \text{ px}/\mu\text{m}$ and the resolution of the objective is $r_0 = 0.63(4) \mu\text{m}$. The predicted resolution of 639 nm is within the error margin.

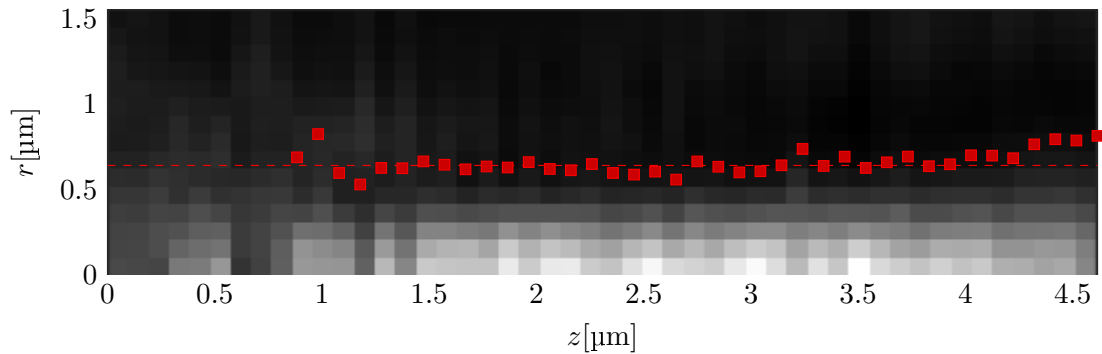


Figure 4.6: Measurement of the 3D PSF of the objective. The radial profile of the PSF is plotted for a range of z -values. The red dots denote the results for the fit of the resolution of the objective. The dashed line denotes the diffraction limit for 461 nm light of 639 nm. The objective is diffraction-limited from 1.1 μm to 4.2 μm .

If we had not taken the assumption that the 200 nm diameter holes are point sources for the objective, the found resolution should have been deconvolved with the size of the holes. When using (2.20) with the resolution of 0.63 μm and the 100 nm radius of holes, the obtained resolution is 0.622 μm . The difference of not taking this assumption is much smaller than the error margin on the measurement and can thus safely be neglected.

4.3 Additional performance measurements

Other important quantities for characterizing the performance of our objective are the depth of field and the field of view. Besides that, the objective is tested for different wavelengths, most importantly 532 nm, and the chromatic aberration of the objective is modeled.

4.3.1 Depth of field and 3D PSF

As defined in section 2.4, the depth of field (DOF) is the region along the optical axis in which the objective focuses within satisfactory resolution. The DOF can be measured by measuring the resolution of the objective for different values of the position on the optical axis z . In section 3.2.1, the DOF where our objective is diffraction-limited is predicted to be 3.1 μm .

By varying the position of the field lens of the objective, the focus of the objective is varied. After each step with the field lens, a shot is taken and the resolution of the objective is determined. As the Laplacian of Gaussian method did not result in satisfactory fits for every frame, the same single spot is manually cropped out in each

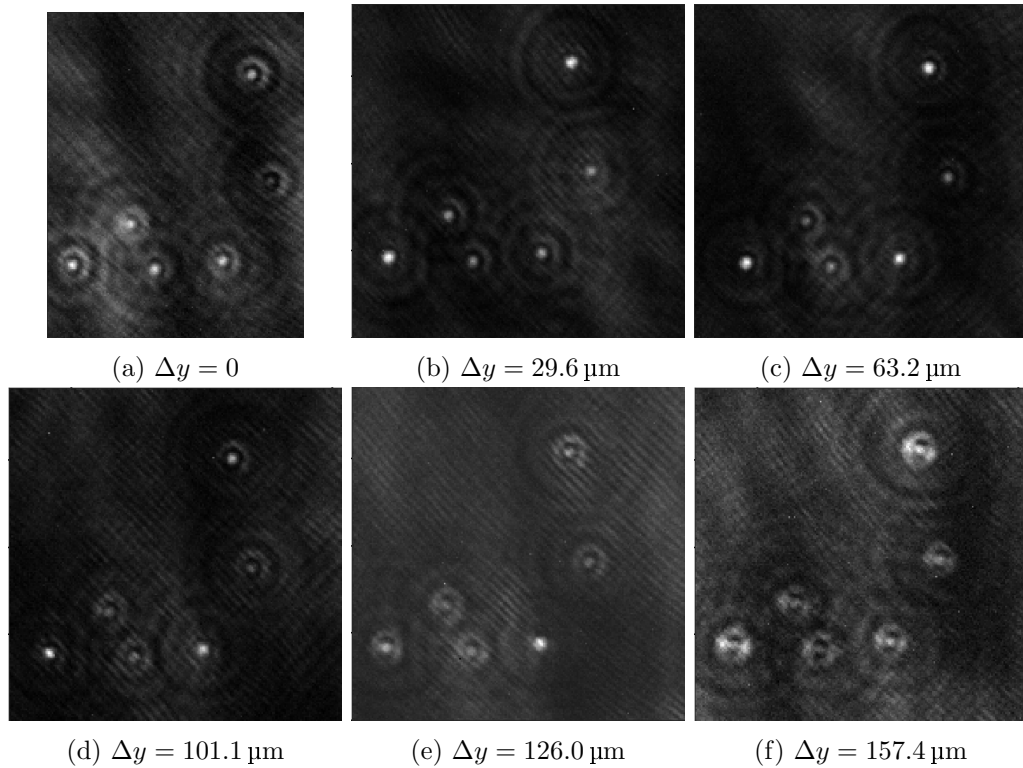


Figure 4.7: The field of view is modeled by translating the target. At $\Delta y = 126.0 \mu\text{m}$ shot, the objective is no longer diffraction-limited.

frame. The exact position is determined by a fit of a 2D Gaussian on the spot. Around that center the azimuthal average is taken to obtain the radial profile. In figure 4.6, a visualization of the 3D PSF of the objective is given. The radial profile for each frame is normalized and plotted. The resolution of the objective is marked by the red dots in the plot and the diffraction limit is given as the red dashed line. For values of z from $1.1 \mu\text{m}$ to $4.2 \mu\text{m}$, approximately, the objective is diffraction-limited, which is in very good agreement with the predicted value of the DOF of $3.1 \mu\text{m}$. At values below $z = 0.8 \mu\text{m}$, the quality of the crop was bad due to defocus and the fit for the center was not satisfactory. This means the resulting radial profile does not contain useful information and the fit of the RMS value cannot be used. The fit results for values of $z < 0.8 \mu\text{m}$ have therefore been omitted from figure 4.6.

4.3.2 Field of view

Testing the field of view (FOV) is done by translating the target in front of the objective using the translation stage. For each frame, the resolution is determined using the same method used for the resolution measurements. Six shots for different positions of the target are presented in figure 4.7. The amount of translation Δy is determined by the

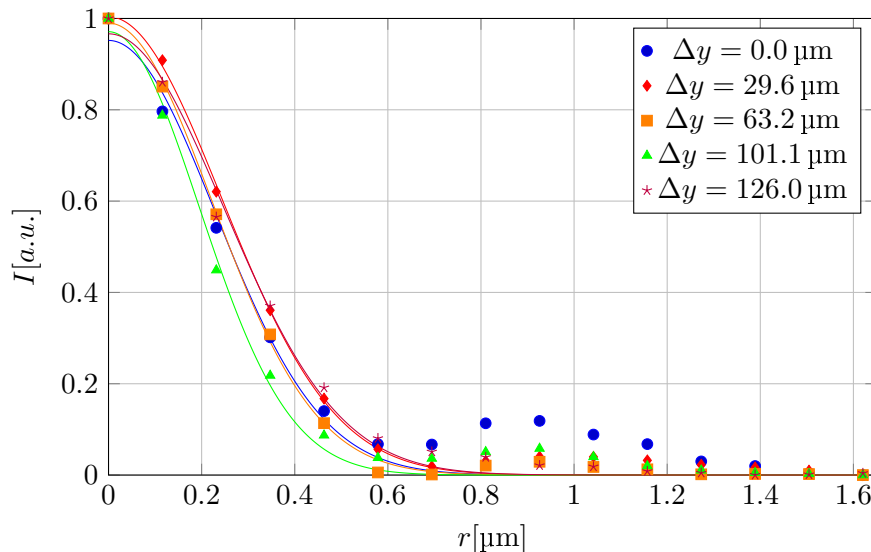


Figure 4.8: Radial profiles for the different frames in figure 4.7. The solid line depict the Gaussian fit through the data points. All data sets resulted in resolutions around the diffraction limit. At $\Delta y = 126.0 \mu\text{m}$, the objective starts losing this behaviour as the fitted resolution is $0.719 \mu\text{m}$.

distance of the field to the camera field in pixels, converted to μm using the calibration that is determined in section 4.2.

Radial profiles for spots in the frames in figure 4.7 are presented in figure 4.8. All the profiles result in fits that have resolutions close to the diffraction limit. The objective is diffraction-limited up to frame 4.7d, and barely exceeds the limit with $r_0 = 0.695(13) \mu\text{m}$ in frame 4.7e. This gives an estimate of about $100 \mu\text{m}$ for the FOV. This is a lower limit since the objective is still diffraction-limited in frame 4.7a, which is cropped by the edge of the CMOS chip of the camera. Since $100 \mu\text{m}$ is already large enough for our needs and of the same order of magnitude as the value predicted in section 3.2, the FOV is not further investigated by displacing the setup to explore a broader range.

4.3.3 Other wavelengths

Finally, we measure the resolution of the objective for different wavelengths. In particular, 532 nm is interesting for our setup as this is the wavelength that will be used for the dipole trap of the Sr atoms in our tweezer experiment. In figure 4.9a, radial profiles are presented for 461 nm , 532 nm , 635 nm and 671 nm light. For 532 nm , the resolution is determined to be $0.75(4) \mu\text{m}$, which is close to the diffraction limit of 738 nm . This lies within the values of the resolution of the objective at this wavelength. For the red wavelengths of 635 nm and 671 nm , the resolution is found to be $1.09(9) \mu\text{m}$ and $1.05(4) \mu\text{m}$, respectively. At these wavelengths, the resolution of the objective starts to drift away

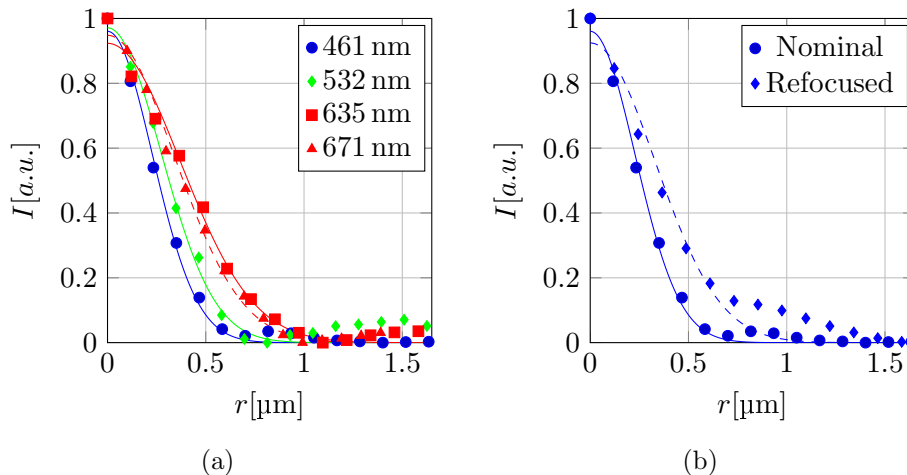


Figure 4.9: Radial profiles of the PSF for different wavelengths. The lines are the Gaussian fit results for the data points. (a): The normalized PSF of the objective for 461 nm, 532 nm, 635 nm and 671 nm light. (b): Two measurements of the PSF for 461 nm light. The nominal is the case when focused with both objective and field lens. The refocused line is the PSF when refocused from the focus of 532 nm light by only adjusting the field lens.

from the diffraction limit given by (2.17). We expect the resolution at the $^1S_0 \leftrightarrow ^3P_1$ transition at $\lambda = 689$ nm to be not much different from these values.

In the tweezer experiment, the trap made by 532 nm light will be imaged using fluorescence from the $^1S_0 \leftrightarrow ^1P_1$ line with $\lambda = 461$ nm. Due to chromatic aberration of the objective there will be a difference in the positions of the focal plane. The position of the objective cannot be moved to focus the blue 461 nm light, so the field lens is the only piece that can be used for focusing. In figure 4.9b, the measured radial profile in the case where the objective is focused on the target that is illuminated with 461 nm light is given with the circles. The diamonds represent the radial profile for the case of first focusing on the target using 532 nm light for illumination and subsequently switching to 461 nm light and refocusing by translating the field lens. This method clearly gives rise to significant aberrations as the radial profile does not have a clear minimum anymore. A Gaussian fit yields a resolution of 1.09(15) μm .

The radial profile for 532 nm is of lesser quality than those for the other wavelengths, due to chromatic aberrations originating from the poor quality of the light source, which had a linewidth of 10 nm. Whereas for the other wavelengths some laser power could be borrowed from one of the narrow linewidth sources used in the other experiments in the lab, there was no such source for 532 nm and a low end commercial laser pointer had to be used. The performance of the objective for the green light has to be measured more thoroughly in a separate setup, which is discussed in section 6.3.

Wavelength	Focus Shift [mm]
461 nm	-0.373
532 nm	0
689 nm	0.485

Table 4.1: Relative shift of the focus due to chromatic aberrations.

Each of the different wavelengths focuses on a different spot on the optical axis due to chromatic aberrations that the objective is not corrected for as mentioned in subsection 2.4.5. On the main machine, the three wavelengths that will go through the objective are 461 nm, 532 nm and 689 nm. The magnitude of the chromatic aberration is not measured directly because 689 nm light was not available at the location of this setup and it has only been modeled using Gaussian beam ray transfer matrix calculations with the lens data. In the simulations, the center of the first lens of the objective is placed at a distance of 3 mm from the viewport. The position of the focus of the 532 nm light is taken to be zero, as the atoms will be trapped there. The relative differences of the positions of the focus of 461 nm and 689 nm light are presented in table 4.1. The negative value for 461 nm means that its focus is closer to the objective than the green focus. The 689 nm light focuses the farthest from the objective. On the main machine, the 461 nm light is used to image the atoms in the trap formed by the 532 nm light and so their foci must overlap. To achieve this, the field lens for the blue light is moved, as modeled in figure 4.9b. The shift of the red light should also be compensated, since the atoms are transported into the focus of the green light through the focus of the red light, which might blow away the atoms. This shift is done by the placement of an additional lens in the red beam path as presented in subsection 6.1.4.

Chapter 5

Theory of single atom preparation for Sr

A lot has been written already on the theory of atom-light interaction [65, 66] and also the element Sr has been thoroughly explored in the literature [42, 67, 68]. The idea of this chapter is therefore to present a short summary of the most important theoretical notes that are fundamental in the understanding of the working of our tweezer experiment. First, in section 5.1, a brief introduction to the element strontium (Sr) is given and in section 5.2, an overview of the relevant atom-light interaction theory is presented. The core of the tweezer experiment is the loading of single atoms of Sr. This is the subject of section 5.3. The detection method of single atoms inside the tweezer is described in section 5.4.

5.1 Getting to know strontium

Strontium (Sr) is an alkaline-earth metal with electronic configuration $[\text{Kr}]5s^2$. The two valence electrons in the filled outer shell produce a singlet ground state 1S_0 without net electronic spin ($S = 0$) and give rise to triplet states with narrow transitions. In nature, Sr is found as a mixture of four isotopes. The three bosonic isotopes ^{84}Sr , ^{86}Sr and ^{88}Sr all have nuclear spin $I = 0$. The fermionic isotope ^{87}Sr has a nuclear spin of $I = 9/2$. The fact that Sr has both bosonic and fermionic isotopes makes it an interesting candidate for simulating quantum systems, where especially the non-zero nuclear spin of the fermionic isotope is interesting [42]. The natural abundance of the isotopes of Sr can be found in table 5.1. Since the ^{88}Sr isotope is an order of magnitude more abundant than the other ones, in the remainder of the work, ^{88}Sr is used to shorten loading times.

Isotope	Abundance	Statistics
^{84}Sr	0.56 %	Bosonic
^{86}Sr	9.86 %	Bosonic
^{87}Sr	7.00 %	Fermionic
^{88}Sr	82.58 %	Bosonic

Table 5.1: Abundance of the four isotopes of Sr. Data taken from [69].

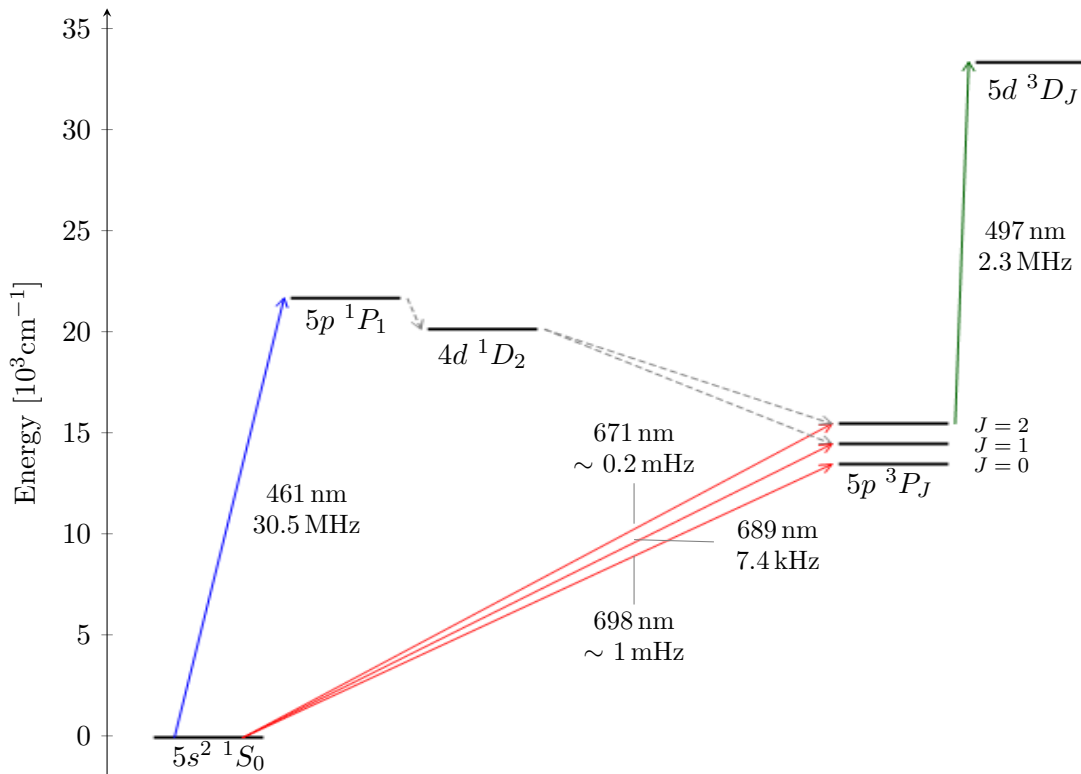


Figure 5.1: The relevant part of the level scheme of Sr. The fine structure splitting of the $5p \ ^3P_J$ state is not drawn to scale for clarity of the image. The dashed lines represent a decay path from the 1P_1 state to the 3P_1 and 3P_2 states. The $^1S_0 \leftrightarrow ^3P_{0,2}$ transitions are given for ^{87}Sr . Energy levels taken from [69, 70].

The relevant part of the Sr level scheme presented in figure 5.1 and it suggests the second reason for the interest in Sr for quantum simulation. Like many alkali and alkaline-earth elements, Sr has many interesting transitions in the visible spectrum for which laser diodes are available. The energy shifts between the different isotopes are several hundreds of MHz, meaning that switching between isotopes can be done using a few acousto-optic modulators (AOMs).

The first transition that deserves special interest is the broad $^1S_0 \leftrightarrow ^1P_1$ transition with $\lambda = 461 \text{ nm}$ and linewidth $\Gamma = 2\pi \times 30.5 \text{ MHz}$. This *blue* transition is used for slowing down and capturing atoms in an initial relatively hot blue MOT. This transition is also the one used for imaging. The second interesting transition is the *red* $^1S_0 \leftrightarrow$

3P_1 transition at $\lambda = 689$ nm, which is used for the formation of the red MOT. The transition is spin-forbidden and is thus much narrower than the blue transition, having $\Gamma = 2\pi \times 7.4$ kHz. Atoms that have been cooled in the blue MOT to temperatures of around 1 mK can be captured in a red MOT and cooled down to temperatures below 1 μ K and a phase space density of around 0.1, which is almost sufficient for quantum degeneracy, which occurs at densities higher than roughly 2.6 [42, 71]. The $^1S_0 \leftrightarrow ^3P_0$ and $^1S_0 \leftrightarrow ^3P_2$ transitions are of special interest due to the fact that they are doubly forbidden and thus ultra-narrow, making them suitable for clock lasers or reservoirs. These transitions are opened as electric dipole transitions in ^{87}Sr by hyperfine mixing of $^3P_{0,2}$ with 3P_1 and 1P_1 . To open the transitions in bosonic isotopes a magnetic field can be applied [68]. The wavelengths for these transitions are 698 nm and 671 nm and the line widths are on the mHz-scale.

The gray dashed lines in figure 5.1 denote a decay channel from the blue MOT to the long-lived reservoir state 3P_2 . In around 1 case in 50000, the 1P_1 state decays to the 1D_2 state, which decays to the 3P_2 and 3P_1 states with a 1:3 branching ratio [72]. Weak-field seeking 3P_2 states can be trapped in the quadrupole magnetic field of the MOT, forming a reservoir of atoms. To bring back the atoms from the 3P_2 state reservoir, they are repumped to the 3P_1 state using a $^3P_2 \leftrightarrow ^3D_J$ transition.

5.2 Atom-light interactions

For the description of interactions between an atom and the light field, two regimes can be distinguished. The first is the near-resonant regime where the wavelength of the light field is close to a transition of the atom and the second regime is the off-resonant regime, where the wavelength is far away from the transitions of the atom. Both regimes are exploited in our experiment and are discussed in the following subsections.

5.2.1 Near-resonant regime

When an atom is placed in a monochromatic near-resonant light field, the interaction is dominated by photon scattering. In this regime, the atom can be modeled as a two-level system consisting of only the transition closest to the wavelength of the light. The ground and excited states are coupled by the light field. The time evolution of the system can be obtained by solving the optical Bloch equations and the photon scattering rate can be determined [65]. For a light field that is slightly detuned from the transition by a detuning $\Delta = \omega_{\text{field}} - \omega_{\text{transition}}$ and linewidth Γ of the transition, the scattering rate

γ_p is given by:

$$\gamma_p = \frac{\Gamma}{2} \frac{s}{1 + s + 4\Delta^2/\Gamma^2}, \quad (5.1)$$

where the saturation parameter $s = I/I_{sat}$ has been introduced as a measure of the field intensity. When $s \ll 1$, the scattering rate is small and the majority of the atoms remain in the ground state. For values $s \gg 1$, the transition becomes saturated and the atoms are distributed equally over the ground and excited states. Near-resonant light is used on our machine to cool the atoms in the transverse molasses cooling, the Zeeman slower and the MOTs. It is also used for the imaging beams to drive excitations of the atoms leading to a fluorescence signal of the atoms.

5.2.2 Off-resonant regime

If the wavelength of the light is far-detuned from the transitions of the atom, scattering events are heavily suppressed. This does however not mean that there is no interaction between the atom and the light, since the light induces an electric dipole in the atom. The energy shift of a state $|i\rangle$ is given by the second-order energy shift from the dipole moment interaction Hamiltonian $\hat{\mu}\mathbf{E}$:

$$\Delta E_i = \sum_{j \neq i} \frac{|\langle j | \hat{\mu} \mathbf{E} | i \rangle|^2}{\hbar \Delta_{ij}}, \quad (5.2)$$

where $\hat{\mu}$ is the operator for the electric dipole moment, \mathbf{E} the operator for the electric field and Δ_{ij} the detuning from the transition $|i\rangle \leftrightarrow |j\rangle$ [66]. This shift is called the AC Stark shift. For the ground state $|g\rangle$, the AC Stark shift can be rewritten as:

$$\Delta E_g = -\frac{1}{4} \alpha_g E_0^2 = -\frac{1}{2} \alpha_g \eta I, \quad (5.3)$$

where $\alpha_g(\omega)$ is the polarizability of the ground state dependent on the frequency of the driving field and E_0 is the amplitude of the electric field of the light [67]. In the last expression of (5.3), we have used that the light intensity is given by $I = E_0^2/2\eta$ with $\eta = 1/c\epsilon_0$ in vacuum [59]. The value for the polarizability $\alpha_g(\omega)$ for Sr atoms has been calculated and cross-checked with experimental data in reference [68].

An important feature of the AC Stark shift, as presented in equation (5.3), is the dependence of the energy on the light intensity. The intensity profile of the light field is usually not homogeneous, which results in a spatial profile for the AC Stark shift and makes the AC Stark shift capable of creating *dipole traps* for atoms. In spatial regions where the energy shift is negative compared to zero light intensity regions, the atoms can be trapped. On the other hand, atoms are repelled from regions where the energy

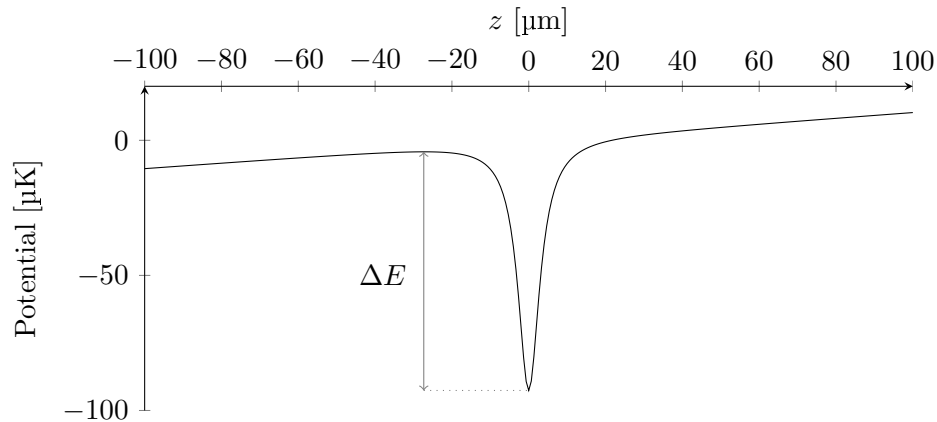


Figure 5.2: The trapping potential of the green beam including gravity, causing a linear pattern. The trap depth is denoted as ΔE .

shift is positive. The sign of the AC Stark shift depends on the sign of the polarizability, which depends on the sign of the laser detuning. For light fields that are far red-detuned ($\Delta < 0$) from a transition, the AC Stark shift is negative and the ground state energy is lowered, whereas for the blue-detuned case ($\Delta > 0$), the AC Stark shift is positive [66].

In our experiment, we use off-resonant 532 nm light with a Gaussian beam profile to create tweezer traps for the atoms. The 532 nm light is far red-detuned from the strongest transition in the ground state of Sr at 461 nm, and so the atoms are trapped in the places where the intensity of the beam is highest. Gravity deforms the trap and superimposes a linear profile on the potential. The resulting trap depth is smaller when gravity is present and only atoms with thermal energies $E_T = k_B T$ that satisfy

$$E_T < |\Delta E_g + mgz|, \quad (5.4)$$

are trapped, where m is the mass of the atom, g the gravitational acceleration, and z the chosen axis along which gravity works. In figure 5.2, the shape of a dipole trap created by a Gaussian beam profile of red-detuned light including gravity is plotted along the gravity axis and the trap depth is denoted by ΔE . The trap depth is often compared to thermal energies, which is the reason it is often expressed in multiples of the Boltzmann constant, resulting in units of K. For a Gaussian beam profile of 532 nm light with 2.86 mW of power and a focus of 0.75 μm , the trap depth is found to be around 300 μK .

As can be seen in (5.2), not only the ground state shifts due to the presence of the light, but also the other states get shifted in energy. For a system with a ground state $|g\rangle$ and an excited state $|e\rangle$, this means the transition frequency is shifted by

$$\Delta\omega = \frac{1}{2\hbar}\eta(\alpha_e(\omega) - \alpha_g(\omega))I, \quad (5.5)$$

which is called the differential Stark shift [73]. Because the differential Stark shift can act as a broadening mechanism and make it impossible to resolve the side-bands of the trap, it is often desirable to reduce it to a minimum. It is important to note that α_g and α_e both scale differently with the frequency ω of the driving field. At certain values of ω , the differential Stark shift can vanish completely as $\alpha_g = \alpha_e$. These are called the magic wavelengths of a transition [73]. Following the calculation methods in [68], for the $^1S_0 \leftrightarrow ^3P_1$ cooling transition in Sr, a magic wavelength is found at around 515 nm. For this reason, our dipole trap is operated at the closest wavelength we had available, which was 532 nm. In the future, this will be improved on by implementing a 515 nm diode laser as the light source.

5.3 Preparation of single atoms

With the tweezer potential present, the next challenge is to obtain a trap containing a single atom only. The simplest strategy is using the Poisson distribution governing the loading process, described in subsection 5.3.1. Two main strategies are proposed in literature to obtain single atom preparation efficiencies better than for poissonian loading, both involving light-assisted collisions. The first strategy involves using the red-detuned MOT light, resulting in the collisional blockade for highly focused traps, described in subsection 5.3.2. This method yields up to 50% efficiency, but is not expected to be possible with Sr atoms. The second strategy uses a separate beam with either red-detuned or blue-detuned light to mediate light-assisted collisions and has been shown to reach near-deterministic efficiencies of 90% [74] and is discussed in subsection 5.3.3.

5.3.1 Loading using a Poisson distribution

The Poisson distribution for the probability $P(X = k)$ of k atoms being loaded into the tweezer after a time t at a constant loading rate ρ is given by [75]:

$$P(X = k) = \exp(-\rho t) \frac{(\rho t)^k}{k!}. \quad (5.6)$$

For the single atom case of $k = 1$, this gives:

$$P(X = 1) = \exp(-\rho t) \rho t. \quad (5.7)$$

The probability of loading a single atom varies with the loading time t and the maximal single atom probability is found at $t_{\text{single}} = 1/\rho$, when the single atom probability is

36.8%. Zero atoms are loaded with the same 36.8% probability, two atoms with 18.4% probability and three or more atoms with 8% probability. In a high density trap such as a tweezer, the three-body losses from collisions are expected to lower the lifetime of samples with three or more atoms. The collisions will decrease the number of atoms to zero, one or two atoms in the tweezers and thus the observed preparation efficiency can be higher than the peak of the Poisson distribution, such as in reference [76] where 44% of the traps contained single atoms.

5.3.2 Collisional blockade

In the tight confinement of the tweezer and with the MOT light present, the collisional blockade regime can be reached where only zero or a single atom is loaded into the tweezer with 50% chance [77]. We consider the case where the tweezer is loaded directly from the red MOT that contains many atoms. Following the analysis in [78], the dynamics of the atom number N in the tweezer is given by:

$$\frac{dN}{dt} = \rho - \gamma N - \beta' N(N - 1), \quad (5.8)$$

where ρ is a constant for the rate of atom loading, γ is a constant for single atom losses due to scattering events with photons or stray atoms in the vacuum chamber and β' is a rate of two-body losses in the system. When a steady-state solution of (5.8) is considered, a weak loading regime (small ρ) and a strong loading regime (large ρ) can be distinguished. Determining the regime is done by looking at the parameter $N_C = \gamma/\beta'$, where $N_C \gg 1$ corresponds to the weak loading regime and $N_C \ll 1$ corresponds to the strong loading regime.

The strong loading regime is of special interest in the case of a highly focused trap, where the collisional term becomes the dominant term for the average number of atoms. For weak loading rates ρ and small γ , the collisional blockade regime is reached, which can be understood as follows: Initially, the tweezer is empty and the first atom is loaded into the trap. Upon the entry of a second atom into the trap, where the collisional term is dominant, a collision mediated by the MOT light occurs, kicking out both atoms. The resulting number of atoms is either zero or one, depending on what exact moment the tweezer is switched off. Effectively, this means loading the tweezer with a single atom with at most 50% probability. When the loading rate ρ exceeds the collisional blockade regime, the atoms load faster than they get kicked out by the MOT light and multiple atoms can be loaded into the tweezer.

The greatest appeal for using collisional blockade to prepare single atoms is that no additional optics have to be installed. The light needed for the collisions comes from

the MOT beams. Experimental realizations of single atom loading using the collisional blockade regime have been reported in references [79, 80], confirming the 50-50 behavior of loading zero or single atoms using only MOT light.

As the typical temperature of the red MOT in the final cooling steps is of around 1 μK , the trap depth of around 300 μK is large compared to the thermal energy of the atoms and ρ is expected to be large in our setup. On top of that, because the detuning of the trapping light is large, the value for γ is mainly determined by the pressure in the vacuum chamber [78]. Our pressure of 10^{-10} Torr is smaller than the pressure used in [78] and the same value of $\gamma = 0.2$ can be assumed. The collisional factor β' scales inversely with the size of the trap, underlining the importance of a small trap size. For a waist of $w_0 = 0.7 \mu\text{m}$, not much smaller than the predicted waist of our tweezer spot, the collisional blockade could be clearly seen in the analysis in reference [78]. Therefore, we expect to be able to reach the collisional blockade regime on our machine. However, we do not expect the collisional blockade to perform well for Sr, because of two reasons, both originating in the narrow linewidth of the $^1S_0 \leftrightarrow ^3P_1$ transition along which the MOT operates. Most importantly, the lifetime of the excited atom pair of which one atom is excited to the 3P_1 state is too large to let the semi-classical analysis of light-assisted collisions be valid, see subsection 5.3.3. Secondly, a bound vibrational mode is resolved due to the narrow linewidth and the atom pairs can be associated to bound molecules that remain trapped [81].

5.3.3 Light-assisted collisions with more than 50 % success rate

Instead of the MOT light, a separate beam can be used to mediate light-assisted collisions in the tweezer. The idea behind this method is to initially load multiple atoms into the tweezer, switch atom loading off by extinguishing the MOT light and then to blow the excess atoms away in a series of controlled collisions. Experimental realizations of this technique using Rb have reached near-deterministic single atom preparation efficiencies [30, 77].

To understand the working principle of the light-assisted collisions, one has to look at the relevant molecular potentials for atom pairs. Two atom pair potentials for two ^{88}Sr atoms, one of which is excited in the 1P_1 state, have been schematically drawn in figure 5.3. The excitation to the 1P_1 state is considered rather than the 3P_1 state, as the long lifetime of the 3P_1 state makes a semi-classical analysis impossible. The notation is taken from references [30, 77] where $|S + S\rangle$ denotes the two-atom state of both atoms in the 1S_0 state and $|S + P\rangle$ the two-atom state where one of the two atoms is excited to the 1P_1 state. The two relevant singlet excited states both are attractive for small

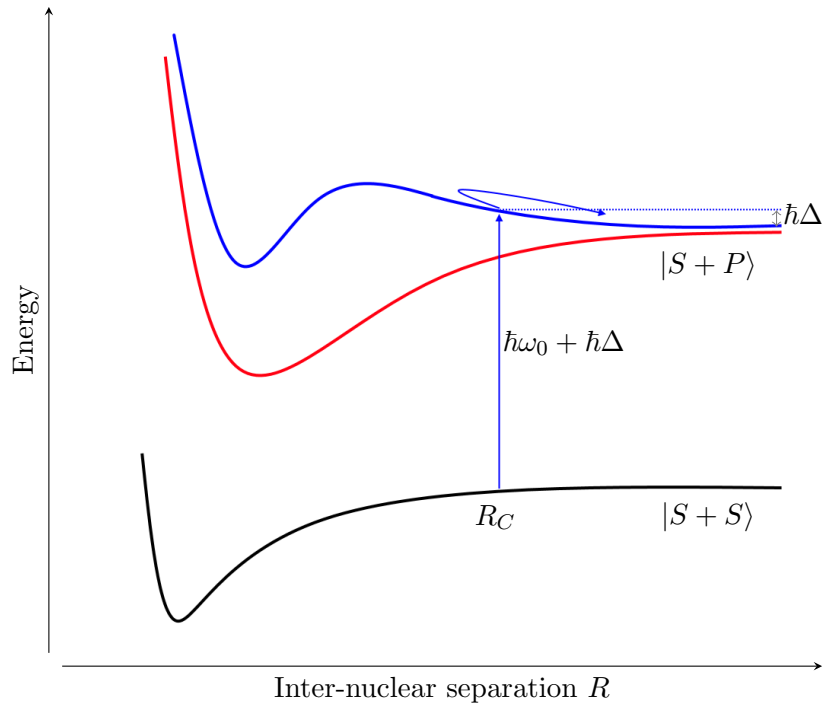


Figure 5.3: Schematic drawing of the molecular potentials for the Sr_2 dimer. The blue solid arrow depicts excitation of an atom pair to the repulsive potential via a blue-detuned photon, where it rolls down the potential hill and gains a momentum boost. Potential shapes taken from [82].

values of the inter-nuclear separation R , but for larger values of R the blue potential has a repulsive bump, which is why we will call the blue potential the *repulsive* potential in the rest of the analysis and call the red potential the *attractive* potential.

As depicted in figure 5.3 by the solid blue arrow, a separate laser source can produce photons that are blue-detuned with a detuning Δ from the free transition to excite a short-lived unbound state on the repulsive potential at an energy shift $+\hbar\Delta$ from the free energy. During its lifetime and in process of the collision, the unbound state will roll down the potential bump, gaining kinetic energy maximally equal to the excitation energy $\hbar\Delta$. After decaying back to the $|S + S\rangle$ state, the kinetic energy is distributed over the two atoms because of momentum conservation. If Δ is chosen such that

$$E_T < \hbar\Delta < 2E_T, \quad (5.9)$$

where E_T is the trap depth, it is impossible for both atoms to obtain a kinetic energy higher than E_T at the same time and at least one of the two atoms remains in the trap. This method has been shown to work for Rb and is capable of obtaining single atoms as often as 90% of the time [77]. For the case of excitations to the short-lived 1P_1 state of Sr, it should be noted the the lifetime is so short that the maximal kinetic energy $\hbar\Delta$ might not be reached and larger detunings can be considered, which increase the slope

of the molecular potential at the inter-nuclear separation at which the excitation takes place. By increasing the slope, the force accelerating the atoms is increased.

A similar analysis as above holds for light-assisted collisions using red-detuned light to excite the attractive potential. Light-assisted collisions using red-detuned light has been shown to work in references for efficiencies up to 63% [83]. The main difference is the different slope of the potential, which causes the excitation probability and the energy kick from the collision to be different from the blue-detuned case.

The inter-nuclear distance where the excitation of an atom pair takes place is called the Condon point and is determined by the shape of the $|S + P\rangle$ state potential [74]. At the values of R where the excitations take place, we assume the van der Waals potential of the $|S + S\rangle$ ground state to be negligible and the long range dipole-dipole interactions of the excited potentials to be dominant, which scale as R^{-3} :

$$V_{\text{attr}} \approx -2C_3/R^3, \quad (5.10)$$

$$V_{\text{rep}} \approx C_3/R^3, \quad (5.11)$$

where the constant C_3 can be expressed in terms of the linewidth and wavenumber k as $C_3 = 3\hbar\Gamma/(4k^3)$ [41, 84]. The Condon points are found by solving for the value of R where the potential has changed enough to match the detuning Δ of the photon:

$$-\hbar\Delta = -2C_3/R_{\text{C,attr}}^3 \quad \implies \quad R_{\text{C,attr}} = \left(\frac{2C_3}{\hbar\Delta}\right)^{1/3}, \quad (5.12)$$

$$\hbar\Delta = C_3/R_{\text{C,rep}}^3 \quad \implies \quad R_{\text{C,rep}} = \left(\frac{C_3}{\hbar\Delta}\right)^{1/3}. \quad (5.13)$$

Semi-classically, the probability of an $|S + P\rangle$ excitation at the Condon point can be obtained by looking at the Landau-Zener model [74, 85]. The absorption of a photon by the atom pair is then described as the avoided crossing of two atom-field states $|S + S, n\rangle$ and $|S + P, n - 1\rangle$, where n is the number of photons in the light field. The probability of the atom pair not following adiabatically and instead undergoing a Landau-Zener transition at the Condon point is given as [83, 85]:

$$P_{\text{LZ}} = \exp\left(\frac{-2\pi\hbar\Omega^2}{v\alpha}\right), \quad (5.14)$$

where Ω is the Rabi frequency of the transition, dependent on the intensity of the driving laser, v is the relative speed of the atoms and α is a measure of the force exerted on the atom pair in this semi-classical assumption, given by:

$$\alpha = \left|\frac{d(V_e(R) - V_g(R))}{dR}\right|_{R_C}. \quad (5.15)$$

Using the potentials given by (5.10) and (5.11) for the excited state potential V_e and taking the assumptions mentioned in the calculation of the Condon points so that only the dipole-dipole interactions are considered, $V_g = 0$ and the Condon points are given by (5.12) and (5.13), we obtain values for α :

$$\alpha_{\text{attr}} = \frac{6C_3}{R_{C,\text{attr}}^4} = \frac{3\hbar\Delta}{R_{C,\text{attr}}}, \quad (5.16)$$

$$\alpha_{\text{rep}} = \frac{3C_3}{R_{C,\text{rep}}^4} = \frac{3\hbar\Delta}{R_{C,\text{rep}}}. \quad (5.17)$$

Substituting this into (5.14), gives us:

$$P_{\text{LZ,attr}} = \exp\left(\frac{-2\pi\Omega^2}{3v\Delta} \left(\frac{2C_3}{\hbar\Delta}\right)^{1/3}\right), \quad (5.18)$$

$$P_{\text{LZ,rep}} = \exp\left(\frac{-2\pi\Omega^2}{3v\Delta} \left(\frac{C_3}{\hbar\Delta}\right)^{1/3}\right), \quad (5.19)$$

which is an expression for the probability of an atom pair not getting excited by a photon at R_C . The atom pairs can cross the Condon point more than once and the final excitation probability can be calculated from equations (5.18) and (5.19) as:

$$P_{e,\text{attr}} = 1 - \frac{P_{\text{LZ,attr}}}{2 - P_{\text{LZ,attr}}}, \quad (5.20)$$

for the attractive potential, where the atom pair can cross the Condon point infinitely many times in principle, and

$$P_{e,\text{rep}} = 2P_{\text{LZ,rep}}(1 - P_{\text{LZ,rep}}), \quad (5.21)$$

for the repulsive potential, where the atom pair can only cross the Condon point twice [74, 83].

For our trap depth of 300 μK , the required detuning range to fulfill condition (5.9) is around 39.3 MHz to 78.6 MHz, but as mentioned before the lifetime of the $|S + P\rangle$ state is too small to get the full momentum kick from rolling down the potential. Also, the range is within the $2\pi \times 30.5$ MHz linewidth of the $^1S_0 \leftrightarrow ^1P_1$ transition, so the resonant scattering along this transition will dominate. For these reasons, we performed calculations with a larger detuning of $\Delta = 2\pi \times 150$ MHz, blue-detuned from the transition. For an input beam power of 1 μW that is focused to a waist of 500 μm , the resulting probability of exciting an atom pair at the Condon point of 39 nm separation was 0.33. The momentum release per event is calculated as the force α_{rep} times the lifetime $2\pi/\Gamma$. This is subsequently calculated to an energy kick that the atom pair typically gets from an excitation, which is found to be 391 μK , which is roughly the energy needed to kick

one atom out, but leave the other in the trap. In a more detailed analysis, the heating by off-resonant scattering events needs to be taken into account, which has to be compensated with red cooling light.

5.4 Detecting single atoms using fluorescence imaging

When a single atom is prepared in the tweezer, an imaging method is needed that is sensitive enough to the low-intensity signal of a single atom. Fluorescence imaging on the broad $^1S_0 \leftrightarrow ^1P_1$ transition with $\lambda = 461$ nm and $\Gamma = 2\pi \times 30.5$ MHz is used for this purpose. In fluorescence imaging, an atom is excited by counter-propagating fluorescence imaging beams and decays via spontaneous emission, emitting fluorescence photons in random directions. Photons that are emitted in the direction of the objective are collected by the objective and imaged onto the camera.

The probability of an atom scattering a photon from the fluorescence beams is calculated with equation (5.1). The number of scattering events in an illumination period τ_{exp} is then found as $N = \tau_{exp} \gamma_p$.

The objective detects the photons that are emitted into the solid angle covered by the NA. The fraction of the sphere η_{NA} with radius ρ that the NA encompasses is found by integrating over the solid angle:

$$\eta_{NA} = \frac{1}{4\pi\rho^2} \int_0^{\arcsin(NA)} \int_0^{2\pi} \rho^2 \sin(\theta) d\phi d\theta, \quad (5.22)$$

$$= \frac{1}{2} \int_0^{\arcsin(NA)} \sin(\theta) d\theta, \quad (5.23)$$

$$= \frac{1}{2} - \frac{1}{2} \sqrt{1 - NA^2}. \quad (5.24)$$

The NA of 0.44 for our objective allows us to collect 5% of the emitted light, where we assumed $n = 1$. Other losses are caused by losses on the optical surfaces in the beam path and are estimated to be around 30%. We assume that at least 10 photons are needed on the camera to obtain a signal of the atom, which means around 285 photons need to be emitted by the atom. For two pumping beams at the saturation intensity ($s = 2$), with a detuning of $\Delta = \Gamma/2$, this corresponds to an exposure time of 4.5 μ s.

The atom also gets momentum kicks from absorbing and emitting the photons, resulting in Brownian motion during the exposure time τ_{exp} . The diffused distance during the exposure has to be on the smaller than the size of the trap in order to not significantly lose resolution. When an atom is excited by or emits a photon, it gets a momentum kick $\pm \hbar k$. The Brownian motion results in a random walk of N steps. Assuming N is

large, the net velocity of the atom is given by:

$$v_{\text{net}} = \frac{\sqrt{N}\hbar k}{m}, \quad (5.25)$$

where m is the mass of the atom. Integration of the velocity over the exposure time $\tau_{\text{exp}} = N/\gamma_p$ results in the diffused distance during the exposure:

$$x_{\text{final}} = \int_0^{N/\gamma_p} \frac{\sqrt{N'}\hbar k}{m} d\tau', \quad (5.26)$$

$$= \int_0^N \frac{\sqrt{N'}\hbar k}{m\gamma_p} dN', \quad (5.27)$$

$$= \frac{2}{3} \frac{N\sqrt{N}\hbar k}{m\gamma_p}. \quad (5.28)$$

During the exposure time of 4.5 μs , the atom diffuses around 0.52 μm . This is well within the trap size of 0.75 μm . It should be noted that in the experiments in the next chapter the exposure time has been taken longer, because only the detection of single atoms was relevant and not their position.

When multiple atoms are trapped close together, the fluorescence beams can also drive light-assisted collisions, as discussed in the previous section. To avoid this, the trap is turned off to let the atoms diffuse for a time τ_{free} before the atoms are imaged. The diffusion in free space is given by the temperature T of the atoms. Gravity also plays a part in this along the vertical axis, but its effect is negligible compared to the thermal component. The velocity of an atom is given by:

$$\frac{1}{2}mv^2 = k_B T \quad (5.29)$$

$$v = \sqrt{\frac{2k_b T}{m}} \quad (5.30)$$

The diffused distance is then given by:

$$x_{\text{free}} = \sqrt{\frac{2k_b T}{m}} \tau_{\text{free}} \quad (5.31)$$

As the inter-nuclear separation at which the light-assisted collisions occur is in the several tens of nanometers regime, the exposure time is usually picked on the order of several μs .

Chapter 6

Towards single atom detection of Sr in a tweezer

In this chapter, the tweezer experiment for the single atom detection of Sr is presented. First, the experimental setup is discussed in section 6.1, including the calibration of the camera in section 6.2 and the separate imaging of the tweezer traps in section 6.3. Then, the results of the setup are presented in section 6.4, where first the loading of the tweezer is shown, and then the presumable single atom detection is presented. Potential improvements are presented in section 6.5.

6.1 The tweezer machine

The machine that is used in this experiment is extensively described in the master thesis of Alex Urech [43]. To turn the versatile machine into a tweezer machine, several adjustments have been made to the machine, while maintaining its main functionality. Most importantly, the objective described in chapters 3 and 4 has been installed. The objective is used for two purposes on the setup. First of all, the objective is used to create the tweezer traps for the atoms and secondly, the objective should collect the fluorescence signal of the atoms. Finally, it is placed in the path of the vertical retro MOT beams for both the blue and red MOT and should not make it impossible to form a MOT. For these tasks three separate optical breadboards have been designed, which are discussed in subsections 6.1.2 to 6.1.4.

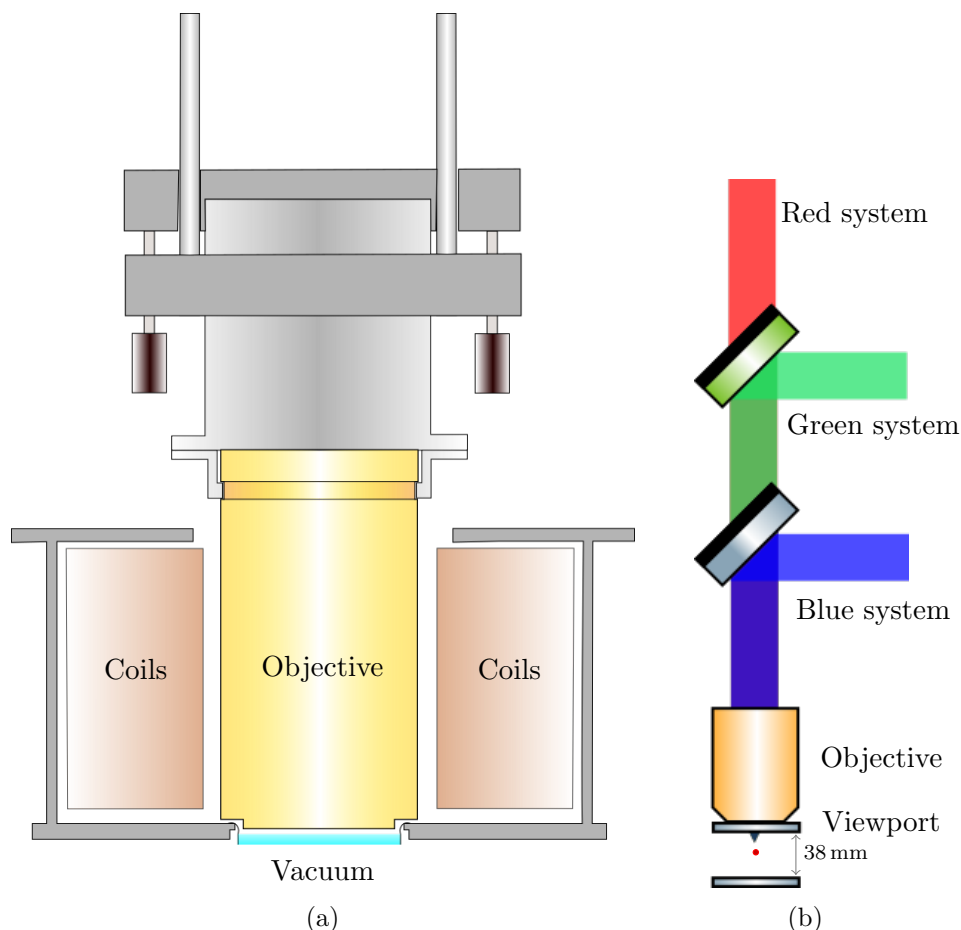


Figure 6.1: Two schematic drawings of the placement of the objective in the machine. (a): The objective is placed above the upper viewport of the main chamber. The mounting piece is clamped to the notches on the outer housing and connected to the top plate of a custom made tilting mount. The bottom plate is connected to the rest of the setup using three 6 mm diameter rods. (b): The three different beam paths are split using two dichroic mirrors. For each of the paths a drawing is presented in the next subsections. The red dot denotes the quadrupole center of the coils.

6.1.1 Installation of the objective

The objective is mounted above the upper viewport of the main chamber. A schematic drawing of the upper part of our main chamber including the viewport and the objective is shown in figure 6.1a. The objective is mounted using the connector piece described in subsection 3.3.3 to the top plate of a custom made tilting mount. The tilting mount consists of two square aluminum plates with side 10 cm connected by four springs. Three adjustment screws (Thorlabs FAS125) allow the top plate to be tilted in two independent directions with a precision of about 0.0025° . The objective and the tilting mount are held in place by three 6 mm diameter rods that are attached to the bottom plate of the

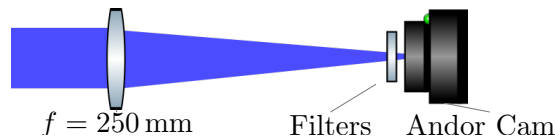


Figure 6.2: Schematic drawing of the blue beam path as installed on the machine at the time of writing. Drawing not to scale. An achromatic lens focuses the light from the atoms onto the camera. In the future, a path for the vertical blue MOT light can be installed.

tilting mount and clamped on a breadboard roughly 40 cm above the vacuum chamber with a dedicated plate.

The three different paths are separated by two dichroic mirrors. This is shown in figure 6.1b. Closest to the objective, the blue light is split off using a 50.8 mm diameter long-pass dichroic mirror with a cutoff wavelength at 505 nm (Thorlabs DMLP505L). The green and red light are split using a similar dichroic mirror with a cutoff at 567 nm (Thorlabs DMLP567L). The dichroic mirrors are mounted in two cage mounts (Thorlabs LC6W) that are slid onto the three connecting rods of the tilting mount.

The center of the quadrupole magnetic field (QP) of the coils in the main chamber is located at the center of the chamber. This is the location where the red MOT is formed after the repumping from the reservoir. The viewports of the main chamber lie 38 mm apart, as drawn in figure 6.1b. Given that the objective has a working distance of 18.175 mm, the focus of the tweezer does not overlap with the initial position of the red MOT and the MOT has to be moved upwards to load the tweezer. The objective is placed as close to the viewport as possible (around 2 mm) to minimize the distance the MOT has to travel, and the front ridge is inserted into the flange of the viewport, without losing the ability to adjust for small tilts.

To place the housing of the objective at a distance of around 2 mm from the flange of the viewport, two perspex spacing rings of 1 mm and 2 mm have been cut out. First, the thicker perspex ring has been placed on the metal flange surrounding the viewport and the objective was gently lowered onto the ring such that it rested on the ring. The position of the rods holding the tilting mount and the objective was marked and the objective was pulled out again. After the thicker spacing ring had been removed and the thinner one had been placed, the objective was placed again at the previously marked position, to ensure a distance of around 2 mm. The thinner ring acts as a safety mechanism. In case the mount of the objective gets loose somehow and the objective falls, the thinner ring will prevent the objective from touching the viewport, which could bring our vacuum at jeopardy.

6.1.2 Blue beam path

The blue path is the path that is used for the fluorescence imaging of the atoms on the $^1S_0 \leftrightarrow ^1P_1$ transition with $\lambda = 461$ nm. The schematic drawing is presented in figure 6.2. The beam coming out of the objective is focused onto an EMCCD camera (Andor Luca) by a 50.8 mm diameter $f = 250$ mm achromatic doublet. To reduce counts from stray light, a bandpass filter (Thorlabs FB460-10) and a shortpass filter (Thorlabs FES0500) are placed in front of the camera. The center wavelength of the band that is transmitted by the bandpass filter is 460 nm and the band has a FWHM of 10 nm, and the shortpass filter has a cutoff wavelength at 500 nm. At $\lambda = 461$ nm light illumination, the loss is specified to be 20 % roughly.

The achromatic lens is placed on a translation stage with a minimal step size of 10 μm to focus the beam on the camera. Given the EFL of the objective at 25.3 mm, the magnification of the blue system is determined to be 9.88. Using (2.9), the 10 μm steps translate to 0.10 μm steps in the focus of the atoms. The Andor Luca camera has a pixel size of 8 μm [86]. A trap of waist 0.75 μm is thus imaged on a 2x2 square on the pixel grid. This is unfavorable for fitting purposes, but since we want to detect only the total number of counts not coming from noise, we expect this to be no problem for our system.

In the current setup, the blue vertical MOT path has been put out of use. The reason for this is that the blue MOT performs sufficiently for our purposes for now, even with the omission of the vertical blue MOT path and including it would mean at least one additional surface of the beam splitting cube through which the fluorescence signal of the atoms has to be transmitted, resulting in a lower signal. On the blue breadboard, space is reserved for future installation of a MOT path, much like the path presented in subsection 6.4.

6.1.3 Green beam path

The green beam path is the path that guides the 532 nm tweezer light. In figure 6.3, a schematic drawing of the green breadboard is presented. The setup consists of three beam paths on the board, numbered with the Roman numerals in the figure. The correct path can be chosen by means of three flip mirrors. Each path starts with a collimator (Schäfter-Kirchhoff 60FC-A11-01) that produces a collimated beam with diameter 1.97 mm. The light source is a free running laser diode (Thorlabs DJ532-40), operated at output of 40 mW. The collimated beam is deflected with a 80 MHz single-pass acousto-optic modulator (AOM) (Gooch&Housego AOMO 3080-125) with an active

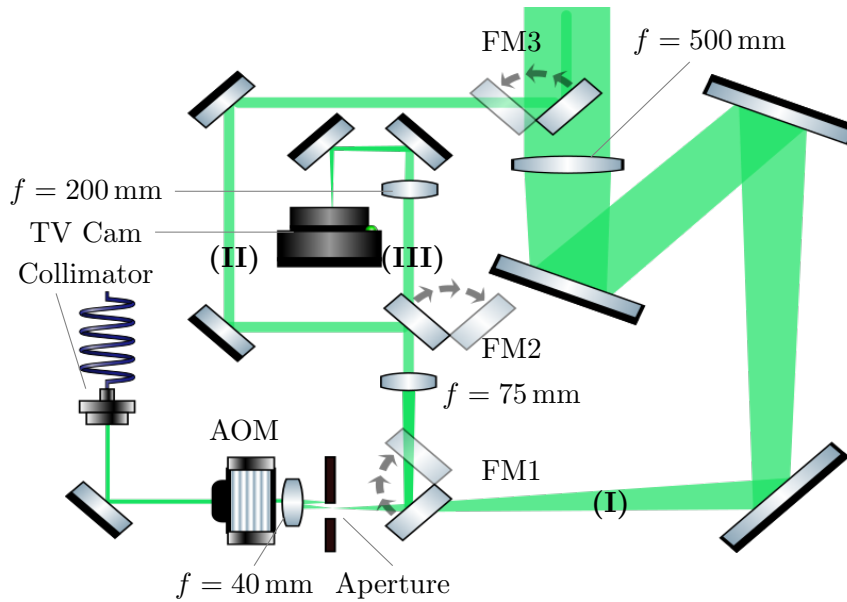


Figure 6.3: Schematic drawing of the green beam path used for making the tweezers. Drawing not to scale. The board can be divided into three paths, marked in the figure with the Roman numbers. A full description for each of the paths is given in the text. The board has been built by Carla Sanna. FM stands for *Flip Mirror*.

aperture of 2 mm. The light from the AOM is focused by a $f = 40$ mm achromatic lens. An aperture filters out the zeroth order in the focus of the lens, such that only the first order light is used for the rest of the beam paths.

The AOM gives intensity and frequency control and allows for making multiple tweezer spots by using different radiofrequencies simultaneously. The different frequencies correspond to different field angles of the incident beam and so the spots projected by the objective are displaced corresponding to this angle. The maximum diffraction angle of the AOM is 4.9 mrad. After the demagnification of this angle by the optics in the green tweezer path with a factor of 12.5 this gives a maximum angle of 0.392 mrad going into the objective. Using formula (3.1) and the working distance of our objective, this corresponds to a distance of 7.7 μm . Assuming a spot size of 1.5 μm , this means we can make around four traps using this setup when leaving 0.5 μm separation between each trap.

The first (I) of the three beam paths after the aperture is the path that has the largest beam and creates the tweezer spots. After three 50.8 mm diameter mirrors the beam is collimated again by a $f = 500$ mm achromatic lens. The diameter of the beam that goes into the objective is 25 mm, which is more than the required beam diameter to use the full NA of the objective and thus to create the small traps of 0.75 μm . A test of the trap size has been performed before installation and is discussed in section 6.3.

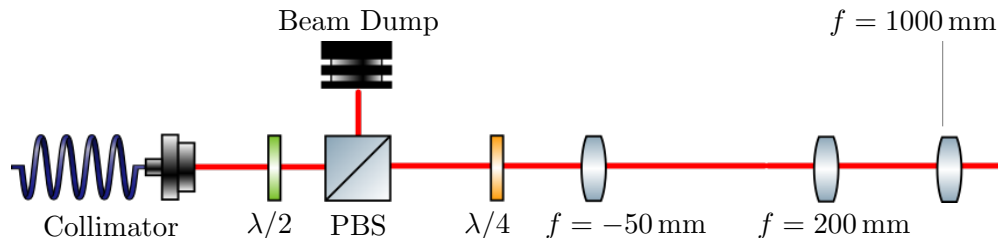


Figure 6.4: Schematic drawing of the board for the red vertical downwards MOT beam. A beam of red circularly polarized light is expanded to fit the size of the upwards MOT beam. The $f = 1000$ mm lens is used to shift the focus of the red light through the objective before the tweezer focus.

When the first and second flip mirror are flipped down, the second beam path (II) is used. This path is used to create a small beam coming into the objective, which results in a big dipole trap. The size of the trap is around $5 \mu\text{m}$ waist. This big dipole trap is used for alignment purposes only.

To investigate the pattern coming out of the AOM, the third beam path (III) allows for imaging the pattern using a TV camera. This path is solely for debugging purposes.

6.1.4 Red beam path

At the time of writing, the red system is not used, because the measurements have been performed on ^{88}Sr . For that isotope, the vertical downwards beam of the red MOT is not needed. For the fermionic ^{87}Sr , however, the vertical downwards beam is more important and has to be implemented. The board that has been installed for this is shown in figure 6.4. Since all the red MOT beams are made with the same AOM, the intensity of this path cannot be regulated independently by that AOM [43]. A $\lambda/2$ waveplate and a polarizing beam splitter are used for this purpose. The $\lambda/4$ waveplate ensures the circular polarization necessary for the MOT light. Afterwards the beam is expanded using an $f = -50$ mm and an $f = 200$ mm telescope to fit the size of the upwards going MOT beam at the QP center.

Due to chromatic aberration, the downwards red beam has a focus farther from the viewport than the green light for the same beam shape going into the objective, as was shown in table 4.1. To prevent this from blowing out the atoms when moving them from the QP center position to the tweezer trap from below, an $f = 1000$ mm lens focuses the beam slightly before being focused by the objective. This shifts the focus of the red up to around 0.5 mm above the green focus.

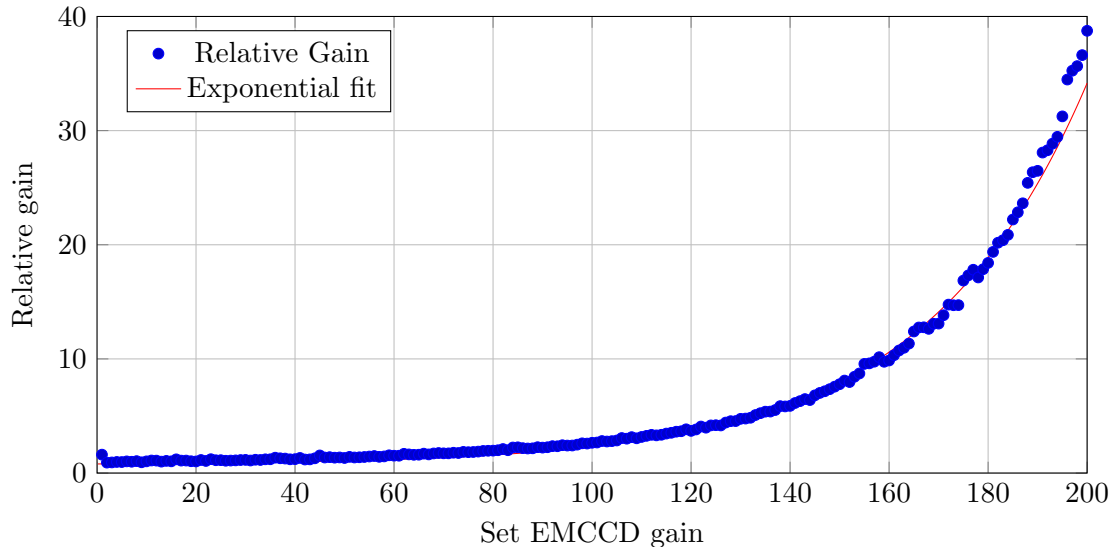


Figure 6.5: The calibration curve of the EMCCD gain of the EMCCD camera. The red line is an exponential fit with formula $g(N) = 0.075 * \exp(0.0305N) + 0.7232$.

6.2 EMCCD camera calibration

In the calculation for the fluorescence detection in section 5.4, only 10 photons in total on the camera have been considered for the detection of the single atoms. To ensure this signal is large enough to be detected, an electron multiplying charge-coupled-device (EMCCD) camera (Andor Luca) is used in the measurements. A calibration of the gain function of the EMCCD camera is required to translate the counts into single photons. To calibrate the gain function of the camera, a beam of well-controlled intensity is sent to the camera and the resulting number of counts is measured. Two optical density filters with $OD = 2$ are placed to lower the intensity further to 320 pW. This low intensity is used to mimic the expected low-intensity signals from the atoms.

For different EM gain values of the camera, the integrated intensity in the beam is fitted with a 2D Gaussian. Afterwards, each frame is normalized by the intensity of the second frame with a gain factor of 1 to obtain a value for the relative gain. The second frame is chosen for normalization, since the first frame corresponds to a set gain of 0, which the camera interprets as no gain, resulting in the use of a different pixel well-depth and hence different measured intensities [86]. The calibration curve of the camera is plotted in figure 6.5, where also the first point for gain of 0 is observed to deviate from the trend. On the horizontal axis, the set value N for the EM gain that is sent to the DAC of the camera is plotted and the relative gain g is plotted on the vertical axis. The red line is

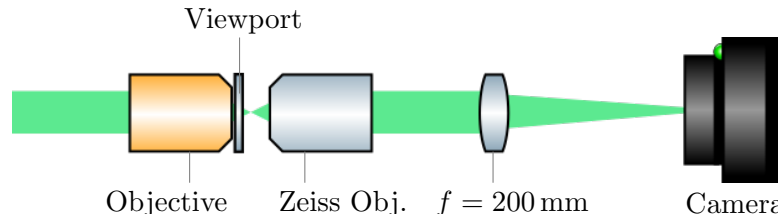


Figure 6.6: Schematic drawing of the test setup for the tweezer spots. The green light from the board described in subsection 6.1.3 is used to form the tweezer. This is imaged using an NA = 0.5 objective.

an exponential fit, resulting in a formula for the gain function $g(N)$:

$$g(N) = 0.075 * \exp(0.0305N) + 0.7232. \quad (6.1)$$

Most measurements are done with a set gain of $N = 254$, which corresponds to a relative gain value of $g = 174$. It should be noted that the calibration curve is not measured at that value of the set gain, which is exactly where the function will be steepest. For future experiments, a new curve should be made, but for this experiment we are more interested in the order of magnitude of the gain than in the actual number.

6.3 Tweezer trap measurements

The size of the tweezers is measured on a setup outside the main machine. The separate setup consisted of the green board discussed in subsection 6.1.3 and the objective mounted on the tilting mount as described in subsection 6.1.1. In this way, the alignment of the green board could be checked and the effectiveness of the tilting stage could be tested. A schematic drawing for the test setup is presented in figure 6.6. The objective creates a spot that will form the tweezer using the light from the green test board. This spot size is measured onto a CMOS camera (BlackFly BFLY-PGE-23S6M-C) by a NA = 0.5 microscope objective (Zeiss EC Plan-Neofluar 20x/0.50) and an $f = 200$ mm field lens. This separate imaging system has first been characterized with the test target described in chapter 4. The fit for the resolution using equation (4.1) is presented in figure 6.7b and it resulted in the resolution of the imaging system of $\sigma_{\text{sys}} = 239.1$ nm. The image and the fit results for the spot formed by the objective are given in figure 6.7d. The fitted standard deviation is found to be $\sigma_{\text{fit}} = 316.4$ nm. Because the spot size created by the objective is close to the fitted resolution σ_{sys} , the spot size is broadened by the PSF of the imaging system. To compensate for this broadening, deconvolution is used, given by (2.20):

$$\sigma_{532} = \sqrt{\sigma_{\text{fit}}^2 - \sigma_{\text{sys}}^2} = 207.2 \text{ nm}, \quad (6.2)$$

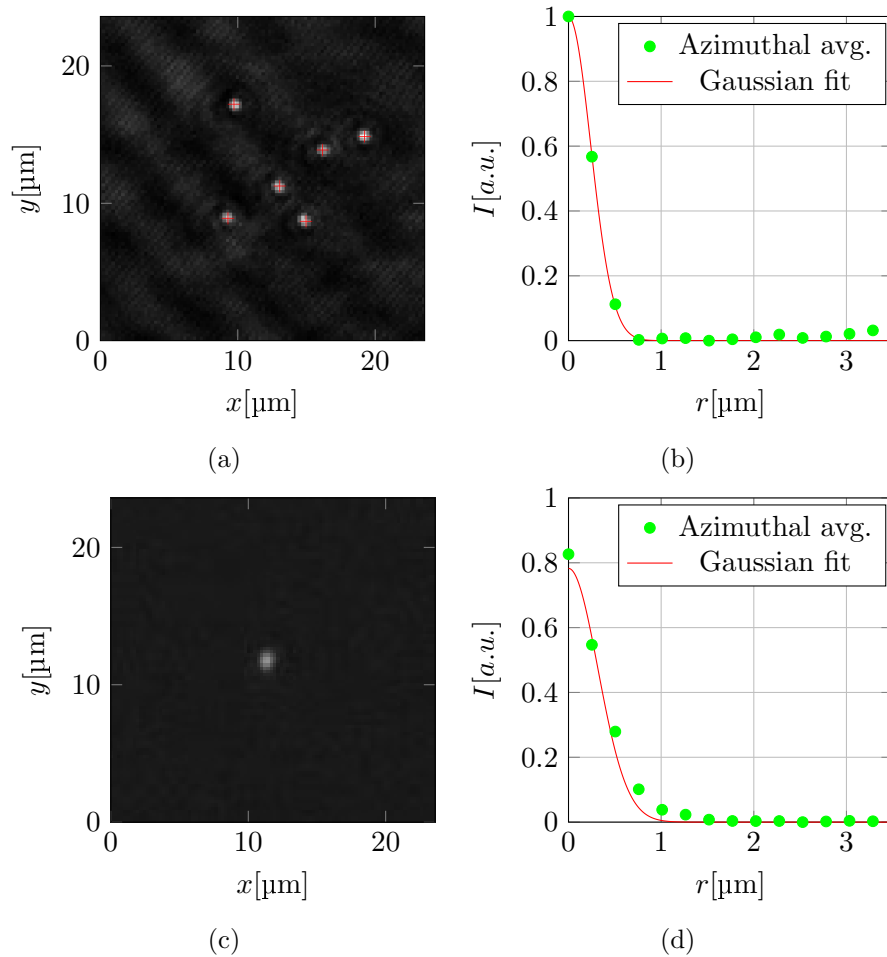


Figure 6.7: (a): The spot pattern of a field of the test target imaged with the green test setup. (b): The resulting fit gives $\sigma_{\text{sys}} = 239.1$ nm. (c): The tweezer spot measured on the separate test setup. (d): The radial profile after analyzing the spot. The solid line is the resulting Gaussian fit, yielding a standard deviation of $\sigma_{\text{fit}} = 316.4$ nm.

which results in a resolution of $0.6 \mu\text{m}$. This is smaller than the diffraction limit for 532 nm and cannot be correct. A possible explanation lies in the low signal-to-pixel ratio in these measurements, limiting the accuracy of the method of detecting the center with the Laplacian of Gaussian method and the subsequent azimuthal averaging. A second possible explanation is the lack of cover glass that the $\text{NA} = 0.5$ objective is corrected for. This causes aberrations that can cause the measured PSF of the imaging setup to increase. The fitted resolution does give reason to assume the tweezer spot has a resolution close to the diffraction limit and hence we take the spot size to be $0.75 \mu\text{m}$, which is the resolution measured in chapter 4.

6.4 Preliminary results

The steps towards single atom detection in Sr are described in this section. The experimental sequence is described in subsection 6.4.1. In subsection 6.4.2, the images and the preliminary results are presented. A hint of single atoms is found in these results, but the data are not robust and potential improvements are discussed.

6.4.1 Experimental procedures

Our experimental procedures can be divided into three steps: First, a general Sr loading and cooling procedure is used to obtain a red MOT with Sr atoms. Secondly, the red MOT is moved upwards towards the focus of the tweezer in a series of magnetic field and laser ramps and finally, the tweezer is loaded and imaged.

Our procedure for Sr loading and cooling is based on the procedure from reference [72], but uses less MOT beams. In the oven Sr sublimates to a gas that is then made into a collimated beam of atoms by means of collimation tubes and transverse cooling beams. The beam is subsequently slowed in a Zeeman slower and captured in an initial blue MOT using circularly polarized 461 nm light and a quadrupole magnetic field. Together with the blue MOT light, the red MOT light is turned on, which does not influence the atoms at this stage, due to the high magnetic field gradient. To shorten loading times, we use ^{88}Sr , which has a significantly higher abundance than the other isotopes. Because the $^1S_0 \leftrightarrow ^1P_1$ transition has a very short lifetime of about 30 ns, many scattering events occur inside the blue MOT and the decay channel from the 1P_1 state to the long-lived 3P_2 creates a reservoir that is magnetically trapped in the quadrupole magnetic field. The filling of the reservoir is so efficient that the vertical blue MOT beams are not needed to trap several million atoms in a loading time of 0.5 s. While the blue MOT beams are ramped off, a repumping flash of 497 nm light is sent to let the atoms in the reservoir state decay back to the ground state. Several tens of ms after the repumping flash, the magnetic field gradient is lowered so that the atoms can be recaptured by the already present red MOT light. The red MOT consists of five beams in a quadrupole magnetic field: Four horizontal beams and one vertical upwards-traveling beam, all circularly polarized with $\lambda = 689$ nm and initially 600 kHz to 2000 kHz red-detuned with a modulation of 20 kHz. The beams are detuned over such a long range so that the fast atoms from the reservoir can be captured. Typically, $2.5 \cdot 10^6$ atoms are trapped in the broadband red MOT. The inclusion of a sixth downwards-traveling vertical beam through the red system from subsection 6.1.4 was found to have no positive effect on the atom number in the red MOT. A possible explanation is the deformation of the beam shape of the downwards-traveling beam by the objective. The red MOT is ramped from

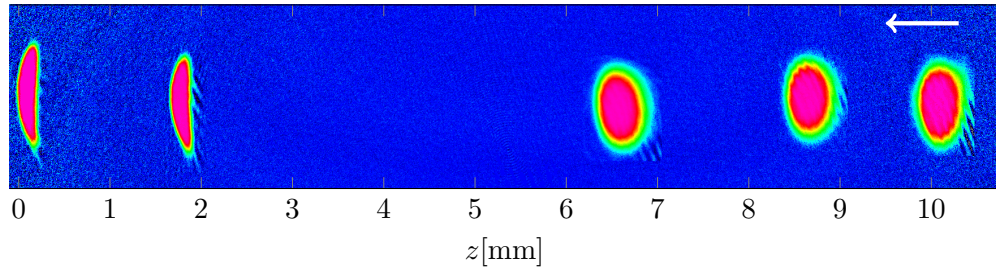


Figure 6.8: The red MOT imaged in-situ for various steps in the transport to the tweezer. Gravity works in the direction of the white arrow.

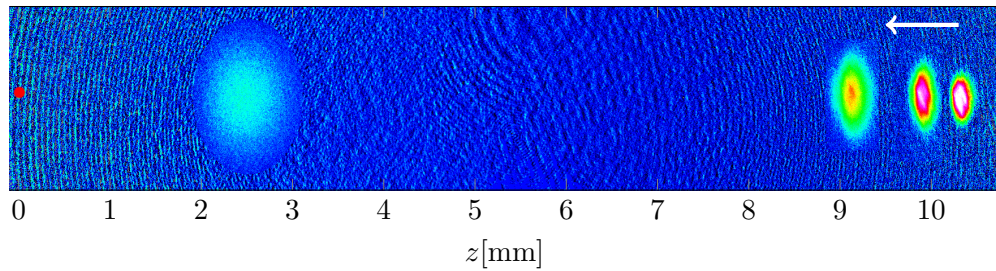


Figure 6.9: The red MOT imaged for four different flight times (3, 8, 15, 40 ms) after the release of the MOT from the tweezer location. The red dot on the left denotes the QP center. Gravity works in the direction of the white arrow.

broadband to almost single frequency in three stages in which the detuning range and intensity of the beams are adjusted to cool and compress the atoms. Going from the initial broadband stage to the first stage, the detuning range is lowered to the span of 100 kHz to 700 kHz. In the second stage, the range becomes 50 kHz to 500 kHz and in the third stage, it is lowered further to the span of 50 kHz to 90 kHz. In all stages, the modulation frequency is kept constant.

The tweezer lies around 10 mm above the QP center, where the red MOT is formed, so the red MOT has to be moved upwards to load the tweezer. Using vertical compensation coils, the magnetic field gradient for the atoms is shifted upwards and the vertical beam pushes the red MOT towards the focus of the green light. This is done in three equal ramps during the cooling stages of the red MOT. Absorption images of the MOT at various positions during the transport are shown in figure 6.8. In figure 6.9, time-of-flight (TOF) images of the red MOT at different times of flight after transport are presented, from which the length and the heating of the transport can be estimated. The atoms are transported from the quadrupole center denoted by the red dot at $z = 0$ to a height a little over 10 mm, shown with the most right image of the MOT. From right to left, the other frames are TOF images for 8 ms, 15 ms and 40 ms flight duration. The atom number measurements resulted in a remarkably high transport efficiency, which is near unity and the temperature in the final stage is determined to be below 1 μ K indicating negligible heating is caused by the transport.

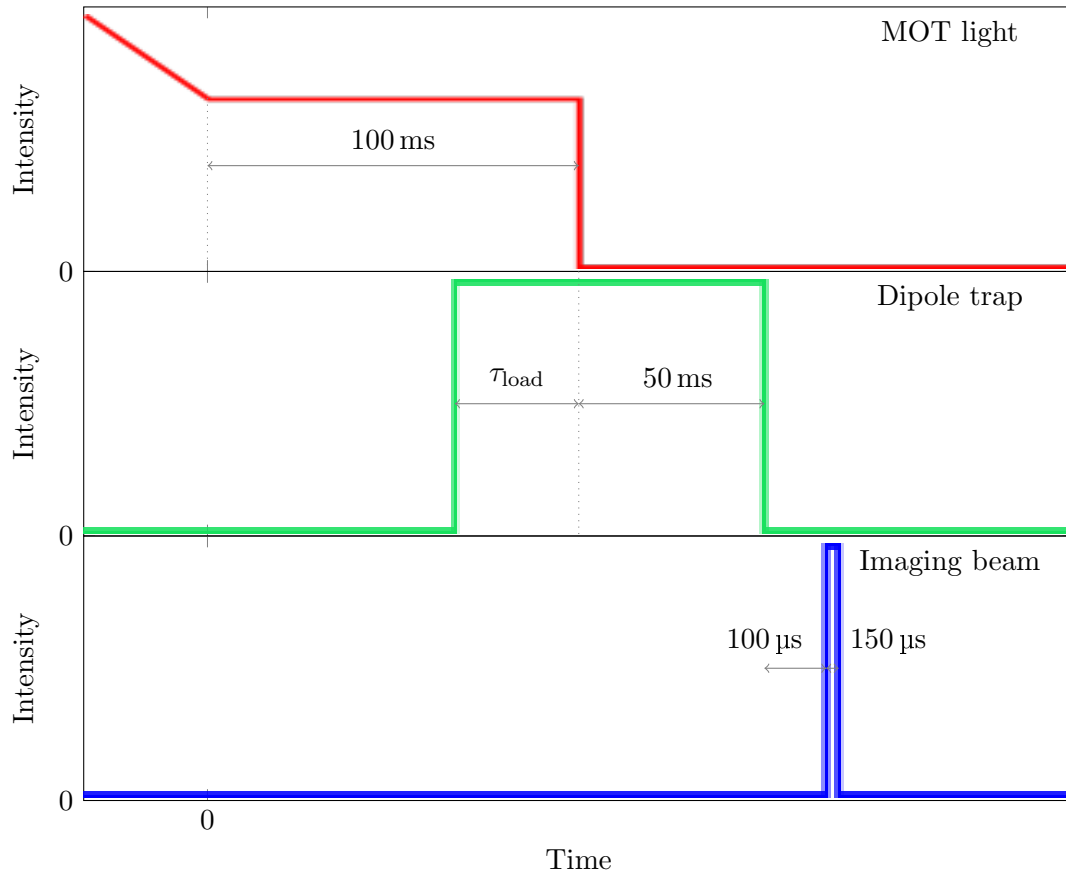


Figure 6.10: Illustration of the beam ramps during tweezer loading. The plots are not to scale.

When the MOT is in its final position and on its final cooling frequencies, the tweezer is loaded and imaged with the timing sequence shown in figure 6.10. After the final ramp of the red MOT, at $t = 0$ a 100 ms wait is issued to ensure the dynamics of the ramping and moving the MOT have settled down. Near the end of the wait, the tweezer trap is turned on within $10 \mu\text{s}$ with a laser power of 2.86 mW, corresponding to a trap depth of around $300 \mu\text{K}$. The tweezer is set to load for a duration τ_{load} , making the effective waiting time for the MOT to lose its dynamics of the ramps $100 - \tau_{\text{load}}$ ms. After the tweezer has been loaded, the MOT is turned off abruptly. During a 50 ms wait time, the atoms from the MOT that are not loaded into the tweezer drop. The tweezer is then imaged by fluorescence imaging. Images of a deep tweezer containing many atoms both before and after dropping the MOT are shown in figure 6.11. The total run time of our sequence is around 2 s.

Before the fluorescence imaging of the atoms in the tweezer takes place, the tweezer itself is turned off and a wait of $100 \mu\text{s}$ is used. This gives the atoms time to diffuse away from each other, which is desirable when multiple atoms are in the trap, to avoid photo-association of Sr_2 dimers that could go undetected. Using (5.31) and the maximum

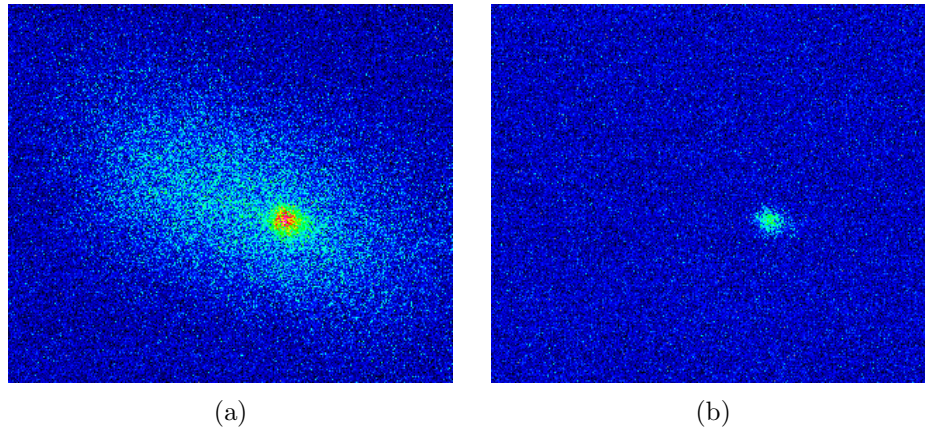


Figure 6.11: Fluorescence images of atoms trapped in a deep tweezer when the MOT is on (a) and after the MOT is dropped (b).

temperature of $300 \mu\text{K}$, this results in a diffused distance of $35.7 \mu\text{m}$. After the atoms have diffused away, two opposing fluorescence beams with an intensity of about $I = 21.5 \mu\text{W cm}^{-2}$ are shone on the atoms for $150 \mu\text{s}$. The two beams are red-detuned by 9 MHz and 7 MHz . The detuning of the beams is different to avoid the creation of a static lattice during the exposure time.

6.4.2 Histograms of the fluorescence signal

Using the experimental sequence as presented in the previous subsection, a series of measurements is taken where the loading time τ_{load} of the tweezer is taken as a variable, to explore the single atom loading. Loading times of 30 ms , 60 ms and 90 ms have been considered. To ensure the other parameters remained constant, after each shot the loading time was adjusted in a cycle $30 \text{ ms} - 60 \text{ ms} - 90 \text{ ms}$, which has been repeated 108 times, resulting in 324 EMCCD camera images.

The analysis of the images starts by determining a region-of-interest (ROI) in which the tweezer is by manually selecting the center of the tweezer and drawing a square around that with side $x_{\text{diff}} = 35.7 \mu\text{m}$, the diffusion distance in the wait time before the imaging. A first crop is taken of the ROI and a second crop is taken of a large background region in which the tweezer could not lie. The mean background is subsequently subtracted from the counts in the ROI crop, and the resulting counts are summed up to a total intensity in the ROI. These counts have been visualized in three histograms in figure 6.12.

Using the parameters of the experimental sequence, we can estimate the number of counts per single atom. Taking the $150 \mu\text{s}$ exposure time into account and the values for the intensity, detuning and linewidth we use equation (5.1), and calculate the number of

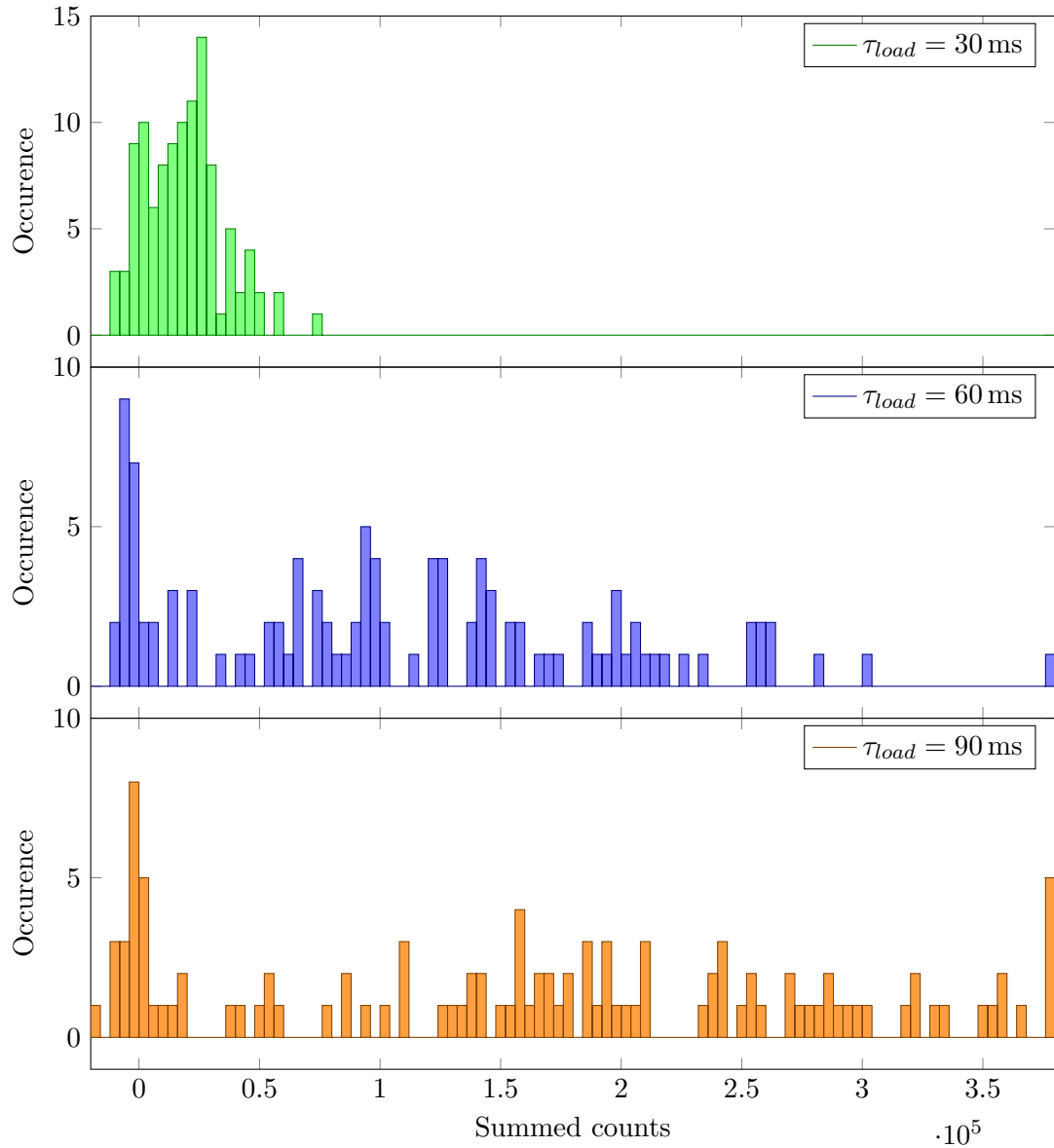


Figure 6.12: Histograms for the summed counts within the ROI after subtraction of the background average for 90 ms (top), 60 ms (middle) and 30 ms (bottom) waiting times.

photons emitted by the atoms to be around 9582 photons. Using $NA = 0.44$ in equation (5.22) and assuming a loss of 30% of the light from the surfaces of the objective and dichroic mirror, the number of photons reaching the camera is then assumed to be 335 photons. The quantum efficiency of the EMCCD camera is around 0.5 for 461 nm light [86] and using the predicted EMCCD gain value of 174 for a set gain of 254 in the fit (6.1), the total number of electrons expected is 29145. The sensitivity of the camera is $1.6 e^-/\text{count}$ and results in around 18000 counts per atom. This number serves only as an order of magnitude estimation as there are assumptions in the gain that is not calibrated in this region and the losses in the system.

The histogram for $\tau_{\text{load}} = 30$ ms loading time is presented with the green bars in figure 6.12. Around the value of 0 counts, a peak is distinguished and a second peak lies around 20000 counts. We expect this to correspond to the predicted signal of a single atom. Using the above analysis the deviation from 18000 could already be explained by a gain factor of 190 instead of the estimated 174. This is further supported by the observation that the peak around zero stays at the same place for longer loading times in the $\tau_{\text{load}} = 60$ ms and $\tau_{\text{load}} = 90$ ms histograms, and the peak at 20000 counts lowering dramatically as more atoms are loaded. However, the peaks are not resolved in the histogram for $\tau_{\text{load}} = 30$ ms and a Poisson distribution fit could not be performed.

A possible explanation for the peaks being not resolved is the relatively low number of runs per histogram, as the collected number of photons from the atoms and the gain of the EMCCD are both stochastic in nature and the peaks in the histograms. During the writing of this thesis, the power supply responsible for the transport is replaced to increase the reliability in the position of the red MOT after transport and the software has been updated, making it easier and faster to collect data in the future.

A second important explanation is noise from the EMCCD camera, consisting of read-out noise and spurious charges [87]. The effect of the read-out noise is the broadening of the zero-peak, which could make it overlap with the single atom peak. The spurious charges are the electrons that are formed by dark currents and clock-induced charge (CIC) instead of a photon. The dark currents are produced by thermal excitations of electrons, which is why the chip needs to be cooled. The CIC comes from the transfer process when electrons are created by the clocking signal. Because the spurious charges are formed before the EM register, they are amplified and result in hot pixels that do not correspond to the signal of an atom, but give counts in the histograms. A measurement for the camera noise only has been performed by taking dark pictures with the camera for different exposure times in the range 1 ms to 900 ms. The average pixel count was 489 counts and the standard deviation of the peak was 5.1 counts. The read-out noise has a long tail at high counts and roughly 1 % of the pixels were more than 100 standard deviations higher than the average pixel count in the 1 ms exposure time frame, indicating significant spurious charges for this camera. To solve this problem, an EMCCD camera model with less CIC noise and a better cooled chip has been ordered (Andor iXon 897 EXF).

In the $\tau_{\text{load}} = 60$ ms and $\tau_{\text{load}} = 90$ ms histograms, a lot of higher summed counts can be seen that appear to be not grouped. The fact that the counts are ungrouped is not only explained by the presence of additional atoms, as peaks around integer multiples of 18000 counts should be expected. It is also important to note that the exposure time was the same for all the histograms, so this effect is also not explained by spurious

charges. It is possible that the ungrouped peaks arise because the number of atoms that is fluorescing is not constant during the exposure. A possible explanation for this is that the long diffusion time of $100\ \mu\text{s}$ before exposure and the lengthy pumping duration of $150\ \mu\text{s}$ allow some atoms to leave the focus of the objective and thus not produce the 18000 counts per atom. A second explanation is the formation of molecules during imaging via the fluorescence beams. The molecules stop fluorescing, which randomly reduces the number of fluorescence photons per atom. This is a trade-off that has to be investigated further since to prevent molecule formation from the fluorescence beams, the atoms should diffuse more, but both might lead to an ungrouped signal. Although this makes it challenging to produce a histogram with clear peaks corresponding to two or more atoms, the problem is fortunately not present when only a single atom is wanted in a tweezer, which is the case for all the interesting experiments.

6.5 Beyond single atom detection

The next step beyond single atom detection is sorting of atoms in multiple tweezer traps. The first intermediate step that has to be taken before atom sorting can take place is the in-situ detection of single atoms. For in-situ detection, in-trap cooling is required. If the atoms are not cold enough, the very low intensity pumping blue light that is needed to make the atoms fluoresce inside the traps is already enough to blow them out of the trap. For the in-trap cooling of the atoms red MOT light can be used, performing molasses cooling of the atoms. The blue fluorescence beam intensity has to be lowered such that the heating by the blue light does not overwhelm the heating capacity of the red light. A cleaner, more effective way of cooling the atoms than with molasses cooling from the MOT light would be side-band cooling, which has been proven to cool single atoms to their motional ground state [88], but this is much more elaborate.

After the atoms have been cooled properly and can be imaged in-situ, the possibility of loading multiple tweezer traps at the same time has to be investigated. Currently, the active aperture of our AOM allows the formation of around 10 traps. In future experiments, however, the AOM can be easily replaced by an AOD or SLM, creating many more traps. At that point, the dedicated diode laser that is used right now as the source of the green light has to be replaced by a more powerful source to provide the amount of power needed for more than a handful of traps. Also, for addressing the traps individually, the control system has to be adjusted from using one digital synthesizer per frequency to a general wavefunction generator that could send all the frequencies at the same time.

With both in-situ detection and the multiple traps, atom sorting can be performed. Using in-situ detection, the control system can determine for every trap whether it contains an atom or not. Based on that result it can then turn off the traps that contain no atoms and move the traps containing an atom by changing the frequencies sent to the AOM (or AOD at that time), resulting in defect-free structures [31, 89, 90]. This opens up many research possibilities, including synthesis and spectroscopy of single Sr₂ dimers in a tweezer trap [34], and creating quantum gates [37, 38]. For the latter and for most other quantum simulation ideas, the ⁸⁷Sr isotope is required, because it is fermionic. Due to the versatility of our machine, switching isotopes is not difficult.

For our current purposes, the poissonian loading efficiency of almost 40 % is sufficient, but when many tweezers will be used, it might be desirable to increase this. In that case a dedicated 461 nm collision beam as described in subsection 5.3.3 can be installed.

Chapter 7

Conclusion & Outlook

In this thesis, a design for a microscope objective for imaging and manipulating atomic Sr is presented that is diffraction-limited at $\text{NA} = 0.44$ and $\lambda = 461 \text{ nm}$. The most important feature of the design is that it only includes commercial lenses, which greatly reduces the costs needed to realize the design. The objective has a long working distance of 18.1 mm and is corrected for a 3.175 mm thick fused silica viewport, making it suitable for imaging outside a vacuum chamber. It has a predicted depth of field of $3.1 \mu\text{m}$ and a field of view of about $200 \mu\text{m}$. A simple stacking model for the housing of the objective is presented, the CAD files of which can be found in appendix D and requested per [email to our group](#).

A prototype objective has been built out of PEEK. It has been tested by illumination of a test target containing 200 nm holes. By fitting a Gaussian approximation to the measured PSF, the resolution is determined to be $0.63(4) \mu\text{m}$ for 461 nm light. This is in excellent agreement with the predicted value of the diffraction limit of 639 nm. This high resolution makes the objective suitable for imaging Sr atoms in a lattice with a spacing of 532 nm, which forms the basis for a quantum gas microscope (QGM). The objective has a measured resolution of $0.75(4) \mu\text{m}$ for light at $\lambda = 532 \text{ nm}$. In combination with the high resolution for the 461 nm light, this makes the objective also a good candidate for tweezer experiments with Sr atoms, where 532 nm light serves as the tweezer trap and imaging is done with 461 nm light.

The objective has been mounted on our main machine to create a tweezer experiment, which is the topic of the second part of this thesis. In this experiment, images are made of a very small number of atoms and there is a possible detection of single Sr atoms in a tweezer. Next steps include realizing a reliable sequence of single atom preparation before turning to in-situ detection and multiple tweezers, which are the stepping stones towards atom sorting and creating defect-free structures.

When defect-free structures are obtained, a variety of experiments are possible on the machine, some of which will be discussed here. The first possible experiments that can be done involve the synthesis of quantum gates. This can be done by performing Rydberg excitations in the tweezer, where the Rydberg blockade turns the long-range interaction of qubits on and off [37, 91], but recently, also proposals have been brought forward to make quantum gates by using the clock states present in ^{87}Sr [38]. A second experiment could be the synthesis of a Sr_2 molecule by loading two tweezers with single atoms and after atom sorting, moving the tweezers to overlap and sending photo-association light to create a single molecule. This would require a 1064 nm tweezer to keep the lifetime of the Sr_2 molecule over a few 100 μs [92–94]. Due to the extra degrees of freedom, the molecule could serve as a multi-dimensional qubit or a qu-d-it [34, 35].

Finally, the tweezer machine forms the perfect training ground for the future goal of creating a QGM on this machine. In the QGM, many wells will be formed by a lattice and they will be individually imaged and addressed by the objective, instead of the single well formed by the tweezer.

Appendix A

Focusing the objective

The imaging system consisting of objective and field lens has to be focused on the atoms. Often, the imaging system is focused by moving the objective with picopositioners [24], but these are expensive. One could also adjust the position of the field lens to focus the system as presented in equation (2.10). The idea is that the effect of moving the field lens on the focus of the microscope is suppressed by the magnification of the optical system consisting of the objective and the field lens. This would then allow less precise (and thus expensive) translation stages for a similar step-size in focus. In this appendix, we go through the calculation of the focusing of the microscope using ray transfer matrices in two scenarios:

1. Focusing by moving the objective
2. Focusing by moving the field lens

We calculate the matrix for both scenarios individually and then compare to see the difference, from which equation (2.10) follows. In the last part of the section we then use those calculations to estimate the focusing range we have.

A.1 Ray transfer calculations

For the calculations of both scenarios, ray transfer matrix analysis is used on a simplified version of the imaging system. The objective is replaced by a single thin lens of $f_o = 25$ mm and the field lens is also assumed to be thin. The ray transfer matrix for a single thin lens is given as

$$M_f = \begin{pmatrix} 1 & 0 \\ -1/f & 1 \end{pmatrix}. \quad (\text{A.1})$$

The ray transfer matrix for light travelling a distance d in free space is given as

$$M_d = \begin{pmatrix} 1 & d \\ 0 & 1 \end{pmatrix}. \quad (\text{A.2})$$

Now we can combine these matrices to obtain a matrix for the total system and obtain

$$M_{\text{total}} = \begin{pmatrix} 1 & d_{\text{cam}} \\ 0 & 1 \end{pmatrix} \begin{pmatrix} 1 & 0 \\ -1/f_i & 1 \end{pmatrix} \begin{pmatrix} 1 & d \\ 0 & 1 \end{pmatrix} \begin{pmatrix} 1 & 0 \\ -1/f_o & 1 \end{pmatrix} \begin{pmatrix} 1 & d_{\text{atoms}} \\ 0 & 1 \end{pmatrix}, \quad (\text{A.3})$$

where d_{cam} and d_{atoms} are the distances of the imaging system to the camera and the atoms respectively, and the distance d is the tube-length. The distances d_{cam} and d_{atoms} are initially taken to be f_i and f_o , the focal lengths of the field lens and objective.

A.1.1 Focusing with objective

Focusing by moving the objective is described by changing d_{atoms} from f_o to $f_o + \epsilon$, where $\epsilon \ll f_o$. We furthermore assume that if $\epsilon \ll f_o$, also $\epsilon \ll d$, since $d > f_o$, so d will stay constant to good approximation during the process of zooming. The total matrix becomes

$$M_{\text{total}} = \begin{pmatrix} 1 & f_i \\ 0 & 1 \end{pmatrix} \begin{pmatrix} 1 & 0 \\ -1/f_i & 1 \end{pmatrix} \begin{pmatrix} 1 & d \\ 0 & 1 \end{pmatrix} \begin{pmatrix} 1 & 0 \\ -1/f_o & 1 \end{pmatrix} \begin{pmatrix} 1 & f_o + \epsilon \\ 0 & 1 \end{pmatrix} \quad (\text{A.4})$$

$$= \begin{pmatrix} 1 & f_i \\ 0 & 1 \end{pmatrix} \begin{pmatrix} 1 & 0 \\ -1/f_i & 1 \end{pmatrix} \begin{pmatrix} 1 & d \\ 0 & 1 \end{pmatrix} \begin{pmatrix} 1 & f_o + \epsilon \\ -1/f_o & -\epsilon/f_o \end{pmatrix} \quad (\text{A.5})$$

$$= \begin{pmatrix} 1 & f_i \\ 0 & 1 \end{pmatrix} \begin{pmatrix} 1 & 0 \\ -1/f_i & 1 \end{pmatrix} \begin{pmatrix} 1 - d/f_o & f_o + \epsilon(1 - d/f_o) \\ -1/f_o & -\epsilon/f_o \end{pmatrix} \quad (\text{A.6})$$

$$= \begin{pmatrix} 1 & f_i \\ 0 & 1 \end{pmatrix} \begin{pmatrix} 1 - d/f_o & f_o + \epsilon(1 - d/f_o) \\ -1/f_i - 1/f_o + d/f_o f_i & -f_o/f_i - \epsilon/f_i - \epsilon/f_o + d\epsilon/f_o f_i \end{pmatrix} \quad (\text{A.7})$$

$$= \begin{pmatrix} -f_i/f_o & -\epsilon f_i/f_o \\ -1/f_i - 1/f_o + d/f_o f_i & -f_o/f_i - \epsilon/f_i - \epsilon/f_o + d\epsilon/f_o f_i \end{pmatrix} \quad (\text{A.8})$$

$$= \begin{pmatrix} -M & -\epsilon M \\ -1/f_{\text{eff}} & -1/M - \epsilon/f_{\text{eff}} \end{pmatrix}, \quad (\text{A.9})$$

where we have used $1/f_{\text{eff}} = 1/f_i + 1/f_o + d/f_i f_o$ is the effective focal length of the system $M = f_i/f_o$ is the magnification of the system.

A.1.2 Focusing with field lens

Focusing by moving the field lens is described by changing d_{cam} from f_i to $f_i + \delta$. Again we assume d to be constant during this translation. The matrix now becomes

$$M'_{total} = \begin{pmatrix} 1 & f_i + \delta \\ 0 & 1 \end{pmatrix} \begin{pmatrix} 1 & 0 \\ -1/f_i & 1 \end{pmatrix} \begin{pmatrix} 1 & d \\ 0 & 1 \end{pmatrix} \begin{pmatrix} 1 & 0 \\ -1/f_o & 1 \end{pmatrix} \begin{pmatrix} 1 & f_o \\ 0 & 1 \end{pmatrix} \quad (\text{A.10})$$

$$= \begin{pmatrix} 1 & f_i + \delta \\ 0 & 1 \end{pmatrix} \begin{pmatrix} 1 & 0 \\ -1/f_i & 1 \end{pmatrix} \begin{pmatrix} 1 & d \\ 0 & 1 \end{pmatrix} \begin{pmatrix} 1 & f_o \\ -1/f_o & 0 \end{pmatrix} \quad (\text{A.11})$$

$$= \begin{pmatrix} 1 & f_i + \delta \\ 0 & 1 \end{pmatrix} \begin{pmatrix} 1 & 0 \\ -1/f_i & 1 \end{pmatrix} \begin{pmatrix} 1 - d/f_o & f_o \\ -1/f_o & 0 \end{pmatrix} \quad (\text{A.12})$$

$$= \begin{pmatrix} 1 & f_i + \delta \\ 0 & 1 \end{pmatrix} \begin{pmatrix} 1 - d/f_o & f_o \\ -1/f_i - 1/f_o + d/f_o f_i & -f_o/f_i \end{pmatrix} \quad (\text{A.13})$$

$$= \begin{pmatrix} -f_i/f_o - \delta/f_i - \delta/f_o + d\delta/f_o f_i & -\delta f_o/f_i \\ -1/f_i - 1/f_o + d/f_o f_i & -f_o/f_i \end{pmatrix} \quad (\text{A.14})$$

$$= \begin{pmatrix} -M - \delta/f_{eff} & -\delta/M \\ -1/f_{eff} & -1/M \end{pmatrix}. \quad (\text{A.15})$$

A.1.3 Comparison of methods

By comparing the results (A.9) and (A.15), we can determine how δ and ϵ scale with respect to each other. This sets the sensitivity of the focusing and thus sets the step-size we need.

Before directly setting (A.9) and (A.15) equal, it is clear that both M'_{11} and M_{22} have additional factors of δ and ϵ that do not vanish when setting both matrices equal. These factors account for aberrations in the system caused by the displacement of the lenses from the optimal setup. However, since we assume $\delta, \epsilon \ll f_o$, we can assume that these factors will not contribute in first approximation.

To verify the assumption that $\delta/f_o \rightarrow 0$, the relative difference between ray tracing results of (A.15) with and without this assumption are shown in figure A.1 for various tube-lengths d . The relative difference depends on d and greatly diminishes as $d \rightarrow f_o + f_i$, which is 525 mm for our setup.

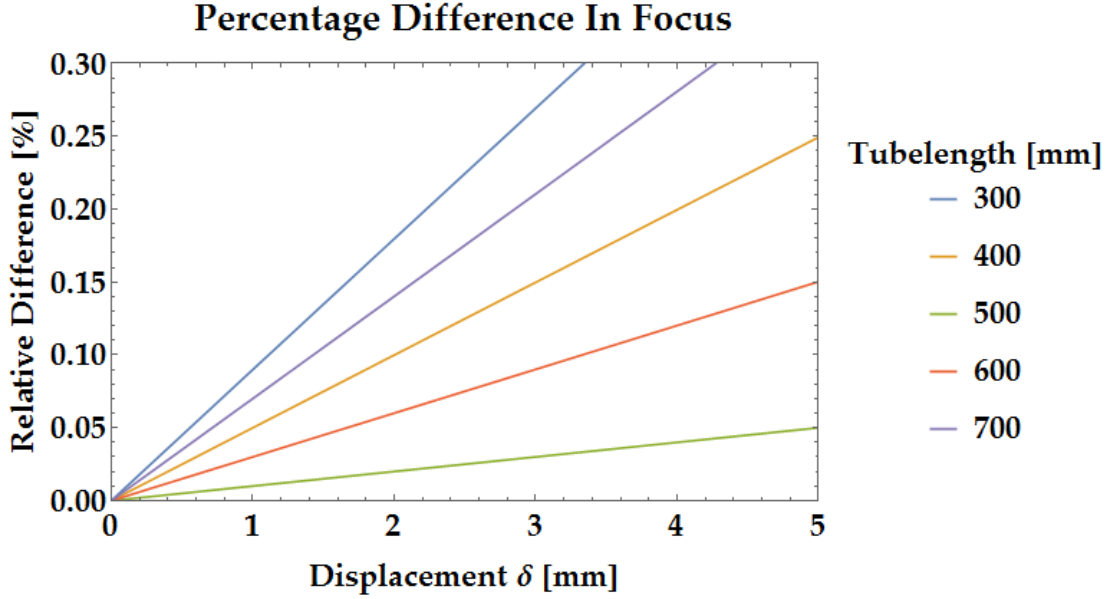


Figure A.1: Percentage difference in the ray tracing results with and without the assumption that $\delta/f_o \rightarrow 0$ for various tube-lengths d .

By setting M'_{12} and M_{12} equal, we obtain an expression for ϵ and δ :

$$-\delta/M = -\epsilon M \implies \epsilon = \delta/M^2. \quad (\text{A.16})$$

Given that in our test setup $f_o \approx 25$ mm and $f_i = 500$ mm, we have $M = 20$ and so

$$\epsilon = \delta/400. \quad (\text{A.17})$$

Since our DOF is around $3 \mu\text{m}$, steps of $\epsilon = 0.1 \mu\text{m}$ are preferable. This translates to $\delta = 40 \mu\text{m}$.

The above analysis depends heavily on the approximation that $\delta, \epsilon \ll f_o$. When this breaks down, the additional terms in M'_{11} and M_{22} will start playing a role and give rise to aberrations. As δ scales faster than ϵ , this first occurs at $\delta/f_o \approx 0.01$, which sets a limit on the method of focusing with the field lens. For our case of $f_o \approx 25$ mm, this means an interval of $\delta \in [-250 \mu\text{m}, 250 \mu\text{m}]$, corresponding to a focus range in target-space of $\epsilon \in [-0.625 \mu\text{m}, 0.625 \mu\text{m}]$, which is small compared to our DOF. When $\delta/f_o \approx 0.1$ the perturbation in M'_{11} for $M = 20$ is still below 1%. This corresponds to a range of

$$\epsilon \in [-6.25 \mu\text{m}, 6.25 \mu\text{m}], \quad (\text{A.18})$$

meaning a $12.5 \mu\text{m}$ range in target-space. This is enough to shift through the DOF.

Appendix B

Calculation of the deconvolution of two Gaussian functions

When an imaging system is used to image an object that has a size close to its resolution, the resulting image h is the convolution of the object f with the PSF of the imaging system g . This means the size of the object can be determined by means of deconvolution of the final image with the PSF of the imaging system if that is known:

$$f = h \circ^{-1} g. \quad (\text{B.1})$$

When the Fourier transform of every function here is taken, the deconvolution operator changes to a regular fraction:

$$\mathcal{F} = \mathcal{H}/\mathcal{G}. \quad (\text{B.2})$$

In this appendix, the calculation for the deconvolution of two Gaussian functions is presented, as the Gaussian approximation to the PSF is widely used in this work. The general formula for a Gaussian function is given by

$$f(x) = a \exp(-(x-b)^2/2\sigma^2), \quad (\text{B.3})$$

where a is a normalization constant that is not important for this analysis and b is the position, which can be taken as zero for the case of the Gaussian approximation of the Airy disk fitted to an azimuthal average. The Fourier transform of the Gaussian function is given by:

$$\mathcal{F}(k) = \frac{1}{\sqrt{2\pi}} \int_{-\infty}^{\infty} f(x) \exp(-ikx) dx, \quad (\text{B.4})$$

$$= \frac{a}{\sqrt{2\pi}} \int_{-\infty}^{\infty} \exp(-x^2/2\sigma^2 - ikx) dx. \quad (\text{B.5})$$

Multiplying by $\exp(A^2k^2)\exp(-A^2k^2)$ allows us to rewrite as:

$$\mathcal{F}(k) = \frac{a}{\sqrt{2\pi}} \exp(A^2k^2) \int_{-\infty}^{\infty} \exp(-x^2/2\sigma^2 - ikx - A^2k^2) dx, \quad (\text{B.6})$$

$$= \frac{a}{\sqrt{2\pi}} \exp(A^2k^2) \int_{-\infty}^{\infty} \exp\left(-\left(x/\sqrt{2}\sigma + Ak\right)^2\right) dx. \quad (\text{B.7})$$

This last step holds if the value of the constant A is $i\sigma/\sqrt{2}$ and the integral can be solved as:

$$\mathcal{F}(k) = \frac{a}{\sqrt{2\pi}} \exp(-\sigma^2k^2/2) \int_{-\infty}^{\infty} \exp\left(-\left(x + i\sigma^2k\right)^2/2\sigma^2\right) dx, \quad (\text{B.8})$$

$$= \frac{a}{\sqrt{2\pi}} \exp(-\sigma^2k^2/2) \sqrt{2\pi\sigma^2}, \quad (\text{B.9})$$

$$= a\sigma \exp(-\sigma^2k^2/2). \quad (\text{B.10})$$

The Fourier transform is thus again a Gaussian and subsequently, equation (B.2) can be rewritten as:

$$\mathcal{F}(k) = \frac{a_h\sigma_h}{a_g\sigma_g} \exp(-\sigma_h^2k^2/2 + \sigma_g^2k^2/2) = \frac{a_h\sigma_h}{a_g\sigma_g} \exp(-(\sigma_h^2 - \sigma_g^2)k^2/2), \quad (\text{B.11})$$

which is again the Fourier transform of the form (B.10), but with $\sigma_f^2 = \sigma_h^2 - \sigma_g^2$. Therefore the deconvolved standard deviation of the object is given as

$$\sigma_{\text{object}} = \sqrt{\sigma_{\text{image}}^2 - \sigma_{\text{sys}}^2}. \quad (\text{B.12})$$

Appendix C

Monte Carlo analysis of the assembly success rate

Using the Monte Carlo analysis option in OSLO [55], a series of simulations for the success rate of assembly is performed. Each series consisted of 500 runs. In each run, the tolerances listed in table 3.3 were used to create a random configuration of the placement of the lenses in the housing, assuming a uniform distribution for each tolerance. To compensate for the misalignment of the optics, compensation variables can be determined which OSLO varies to minimize the RMS value. Using ray tracing analysis, OSLO then calculated an error function change which relates to the performance as:

$$\text{Error Func Change} = \text{Max RMS value} - \text{Nominal value}, \quad (\text{C.1})$$

where the nominal value is computed by OSLO and has a value of 97.9 nm. The maximal RMS value we want to obtain is the diffraction-limit of 639 nm, so the maximum error function change we want is 541 nm.

In total four different series have been performed. The resulting cumulative probabilities of obtaining the desired error function change are plotted in figure C.1. The gray dashed line denotes the desired error function change of 541 nm.

In the first run, only the distance of the first lens with respect to the glass of the viewport is taken as a compensation parameter. In the first run, a success rate of only a few percent is obtained.

In the second run, wiggling of the last lens (TL-LC1315) has been included changing the tilt and the decenter of this lens only. This raised the success rate to more than 5%

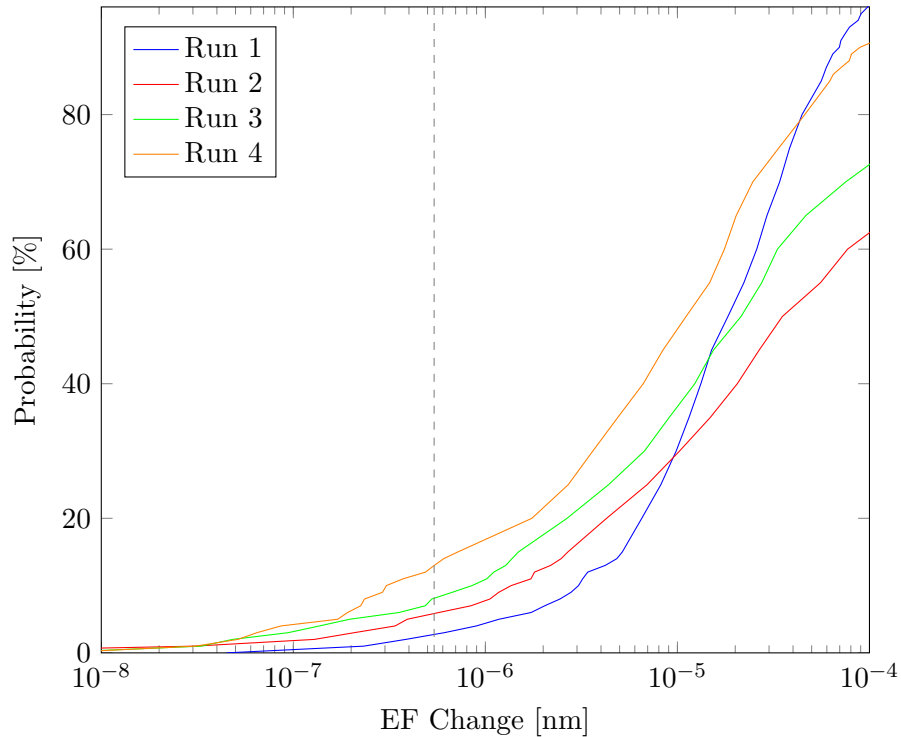


Figure C.1: Monte Carlo analysis for the success rate of assembly. The dashed line marks the desired value. Analysis performed in OSLO [55].

In the third run, the last lens is also displaced axially by taking the distance of this lens to the N-KBX-151 lens as a compensation parameter. This increased the success rate to roughly 8%.

In the final run, the distance of the last lens with respect to the N-KBX-151 lens was again kept constant but the X,Y-displacement of the whole objective is taken as a compensation parameter. This greatly increased the success rate to roughly 14%.

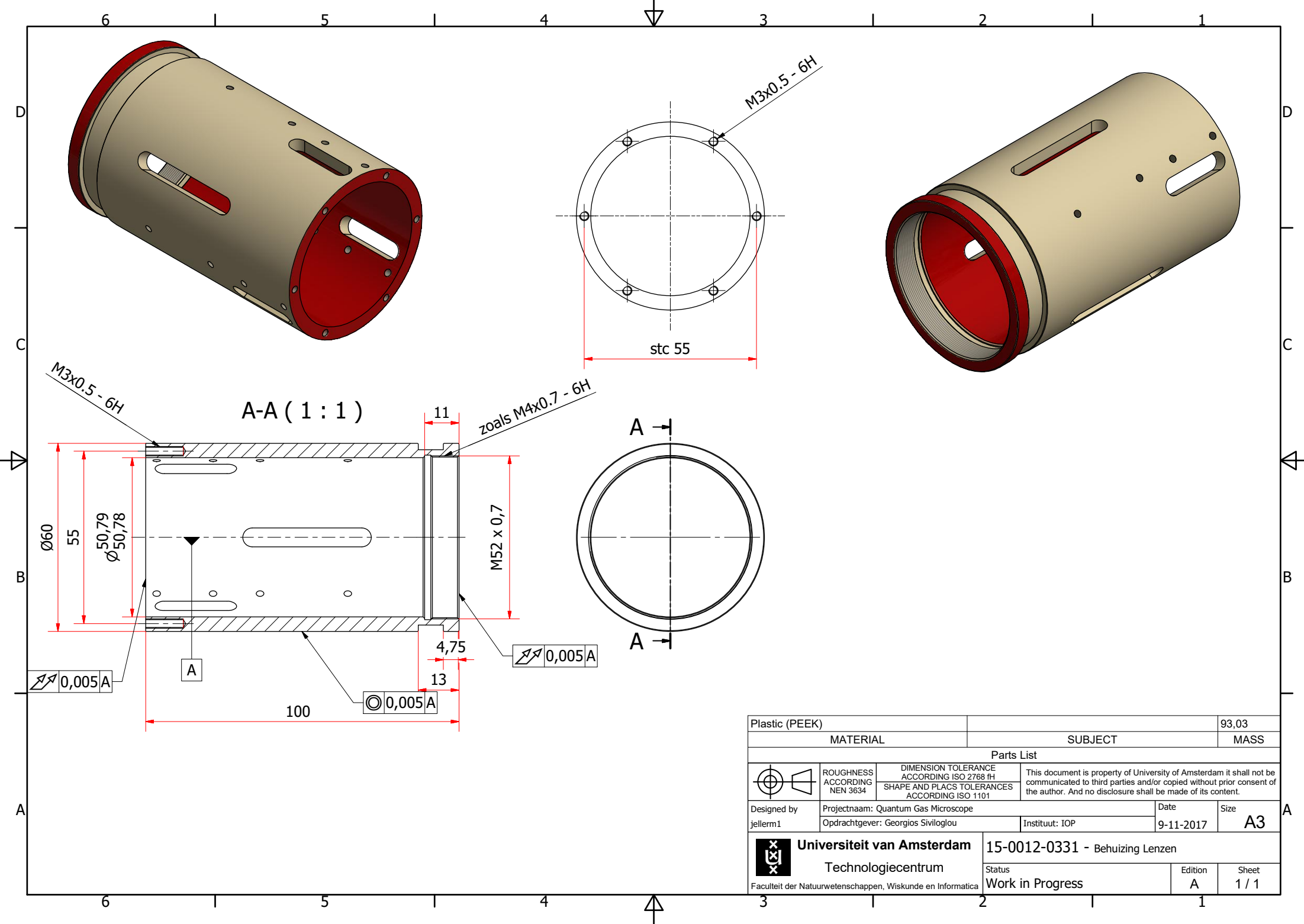
In reality we can also use rotations of the lenses and tilt of the objective as additional compensation parameters, which can only increase the success rate. This makes us confident that we will be able to assemble a working objective, in the worst case after assembling it a few times with random lens rotations.

Appendix D

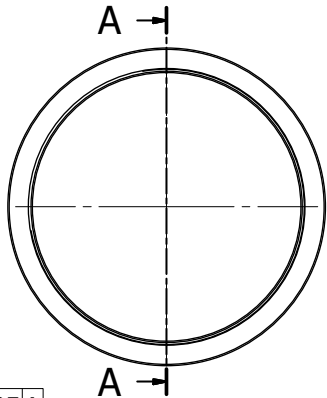
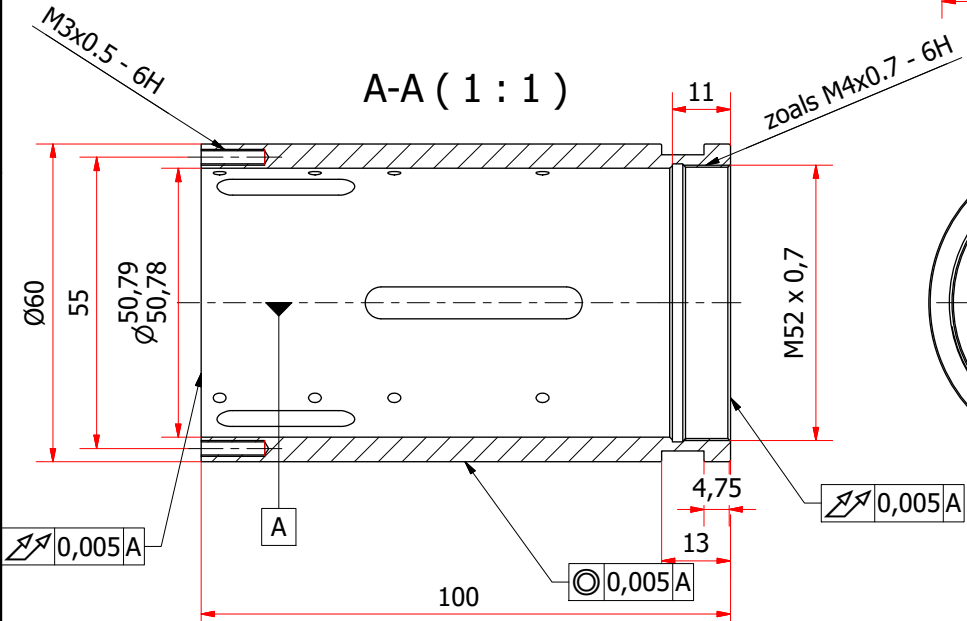
CAD Drawings Thesis

In this appendix, the CAD drawings for the objective that is designed in this project are presented. The designs are free for non-commercial use. For 3D files that can be loaded into Autodesk Inventor, please contact the author or [Florian Schreck](#). The documents are ordered as follows:

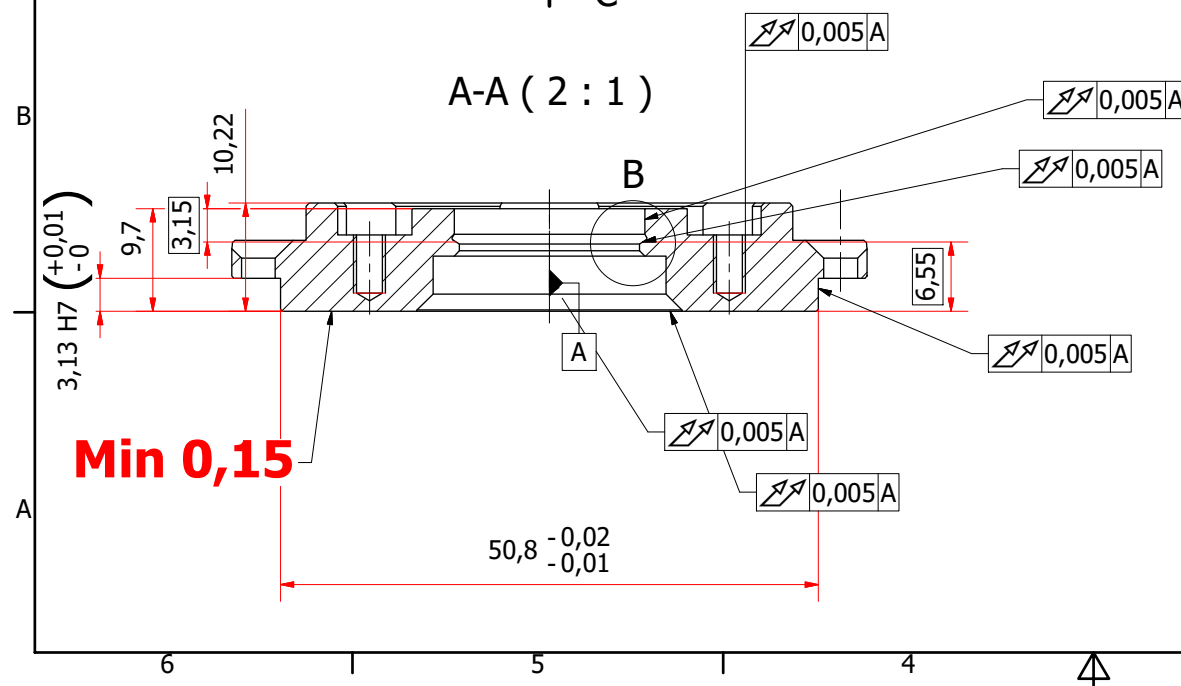
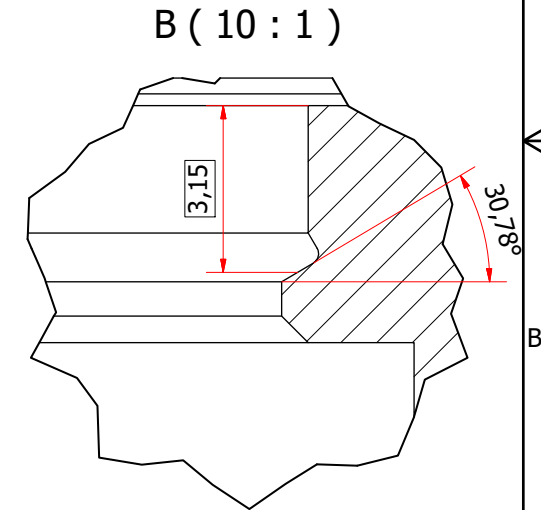
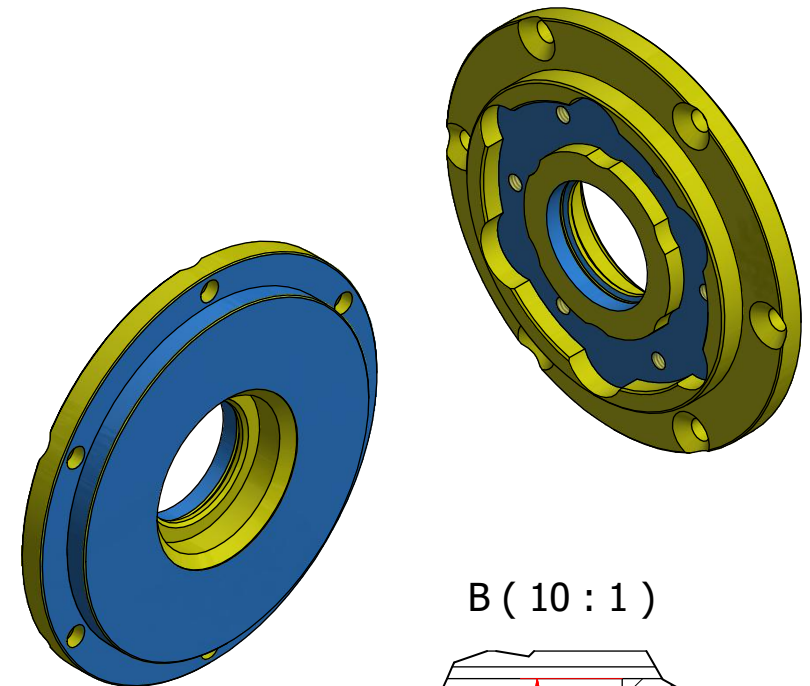
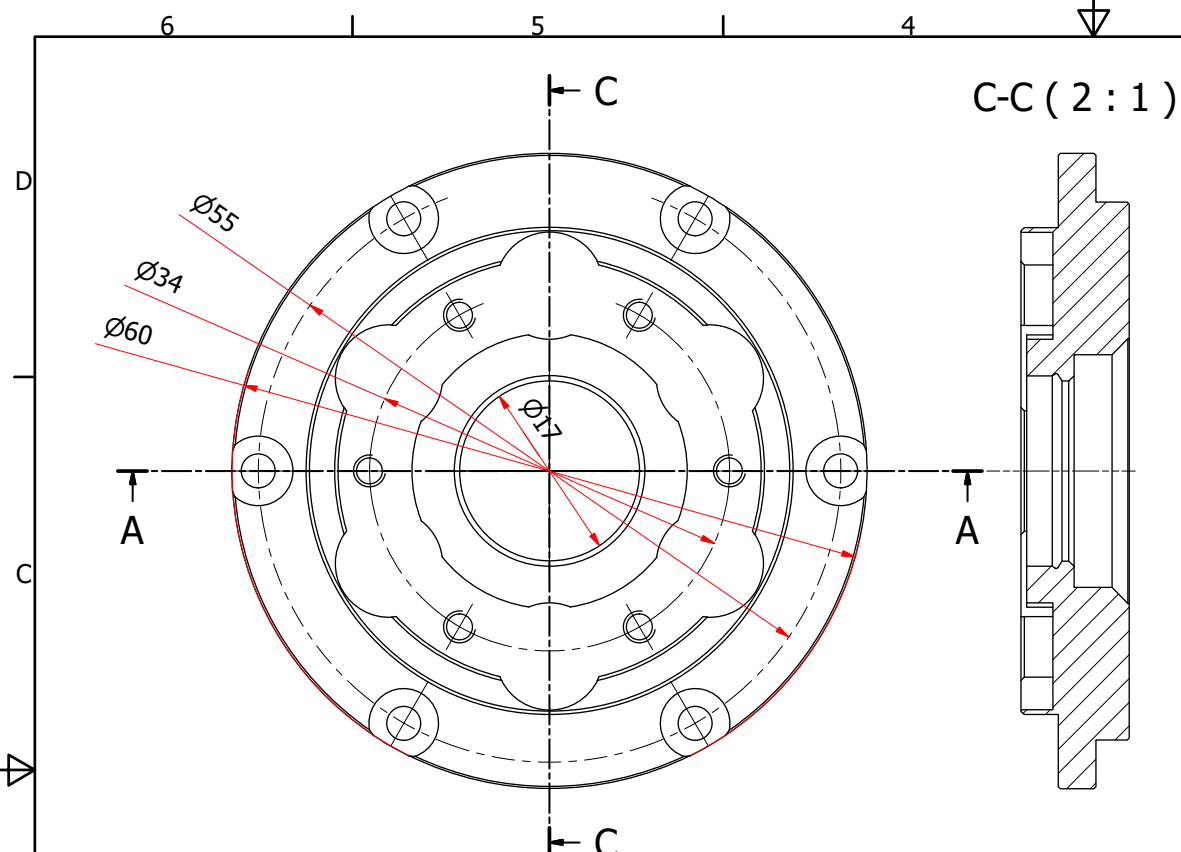
- Page [83](#) contains the drawing for the outer tube.
- Page [84](#) contains the drawing for the front cap to close the tube and hold the mirrors and lenses.
- Page [85](#) contains the drawing for the clamping piece that clamps the mirrors and the first lens to the front panel.
- Page [86](#) contains the drawing for the locking ring that is used to tighten the whole stack inside the outer tube.
- Page [87](#) contains the drawing for the spacing ring between locking ring and TL-LC1315.
- Page [88](#) contains the drawing for the spacing ring between TL-LC1315 and N-KBX-151.
- Page [89](#) contains the drawing for the spacing ring between N-KBX-151 and TL-LE1418.
- Page [90](#) contains the drawing for the spacing ring between TL-LE1418 and TL-LE1076.



A-A (1:1)

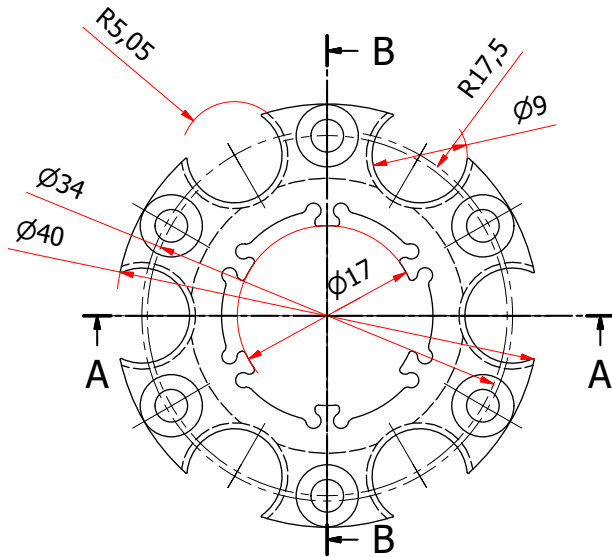


Plastic (PEEK)		93,03	
MATERIAL		SUBJECT	
93,03		MASS	
Parts List			
	ROUGHNESS ACCORDING NEN 3634	DIMENSION TOLERANCE ACCORDING ISO 2768 FH SHAPE AND PLACS TOLERANCES ACCORDING ISO 1101	This document is property of University of Amsterdam it shall not be communicated to third parties and/or copied without prior consent of the author. And no disclosure shall be made of its content.
	Designed by jellerm1	Projectnaam: Quantum Gas Microscope Opdrachtgever: Georgios Siviloglou	
Universiteit van Amsterdam Technologiecentrum Faculteit der Natuurwetenschappen, Wiskunde en Informatica		15-0012-0331 - Behuizing Lenzen Status Work in Progress	
		Instituut: IOP Edition A	Size A3 Sheet 1 / 1

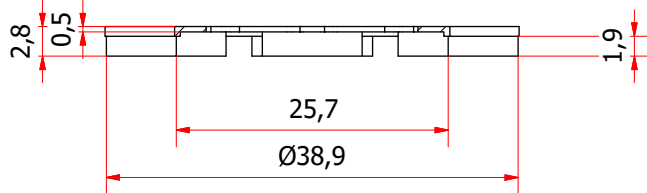


Min 0,15

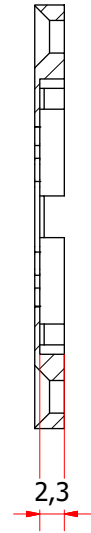
Plastic (PEEK)		20,92	
MATERIAL		SUBJECT	
		MASS	
Parts List			
	ROUGHNESS ACCORDING NEN 3634	DIMENSION TOLERANCE ACCORDING ISO 2768 FH	This document is property of University of Amsterdam it shall not be communicated to third parties and/or copied without prior consent of the author. And no disclosure shall be made of its content.
		SHAPE AND PLACES TOLERANCES ACCORDING ISO 1101	
Designed by jellerm1	Projectnaam: Quantum Gas Microscope	Date 9-11-2017	Size A3
	Opdrachtgever: Georgios Siviloglou	Instituut: IOP	
	Universiteit van Amsterdam	15-0012-0322 - Dop lens-5	
	Technologiecentrum	Status CNC	Edition A.1
Faculteit der Natuurwetenschappen, Wiskunde en Informatica			Sheet 1 / 1



A-A (2 : 1)

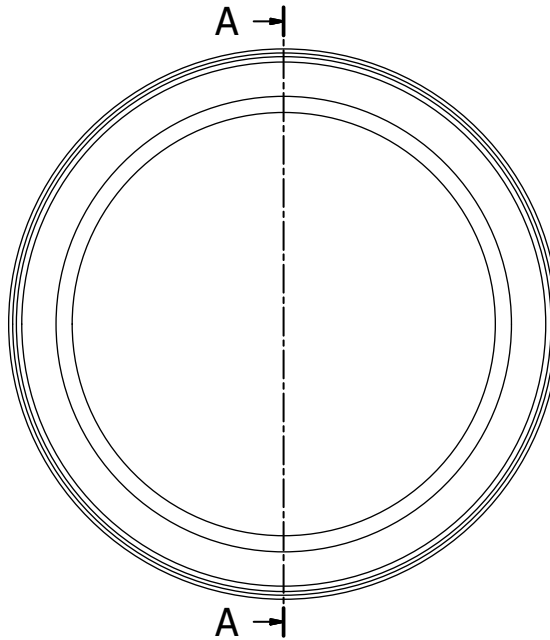
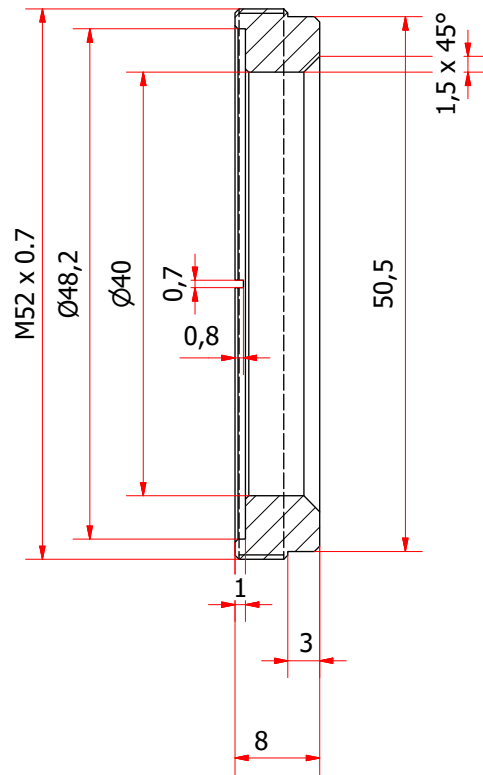


B-B (2 : 1)

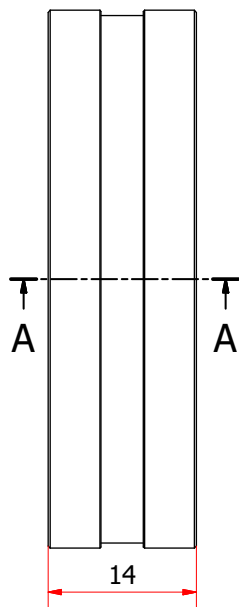
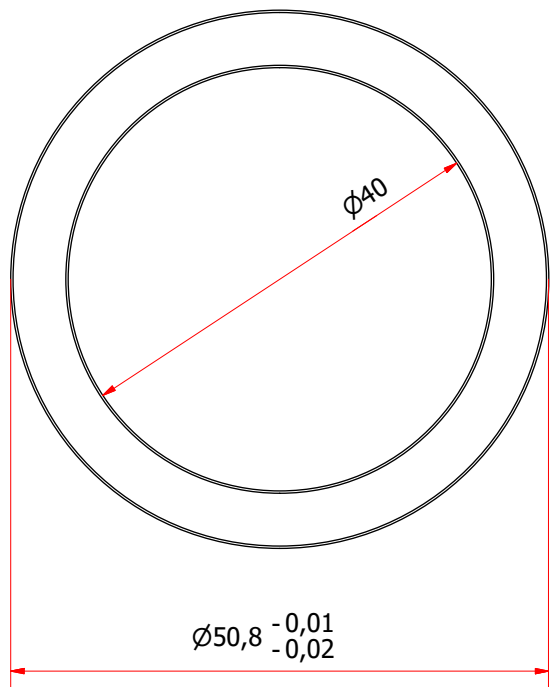


Plastic (PEEK)				1,28
MATERIAL		SUBJECT		MASS
Parts List				
	ROUGHNESS ACCORDING NEN 3634	DIMENSION TOLERANCE ACCORDING ISO 2768 fH SHAPE AND PLACS TOLERANCES ACCORDING ISO 1101	This document is property of University of Amsterdam it shall not be communicated to third parties and/or copied without prior consent of the author. And no disclosure shall be made of its content.	
Designed by jellerm1	Projectnaam: Quantum Gas Microscope Opdrachtgever: Georgios Siviloglou		Date 9-11-2017	Size A3
 Universiteit van Amsterdam Techniecentrum Faculteit der Natuurwetenschappen, Wiskunde en Informatica		15-0012-0330 - Aandruk Ring		
		Status CNC	Edition A.1	Sheet 1 / 1

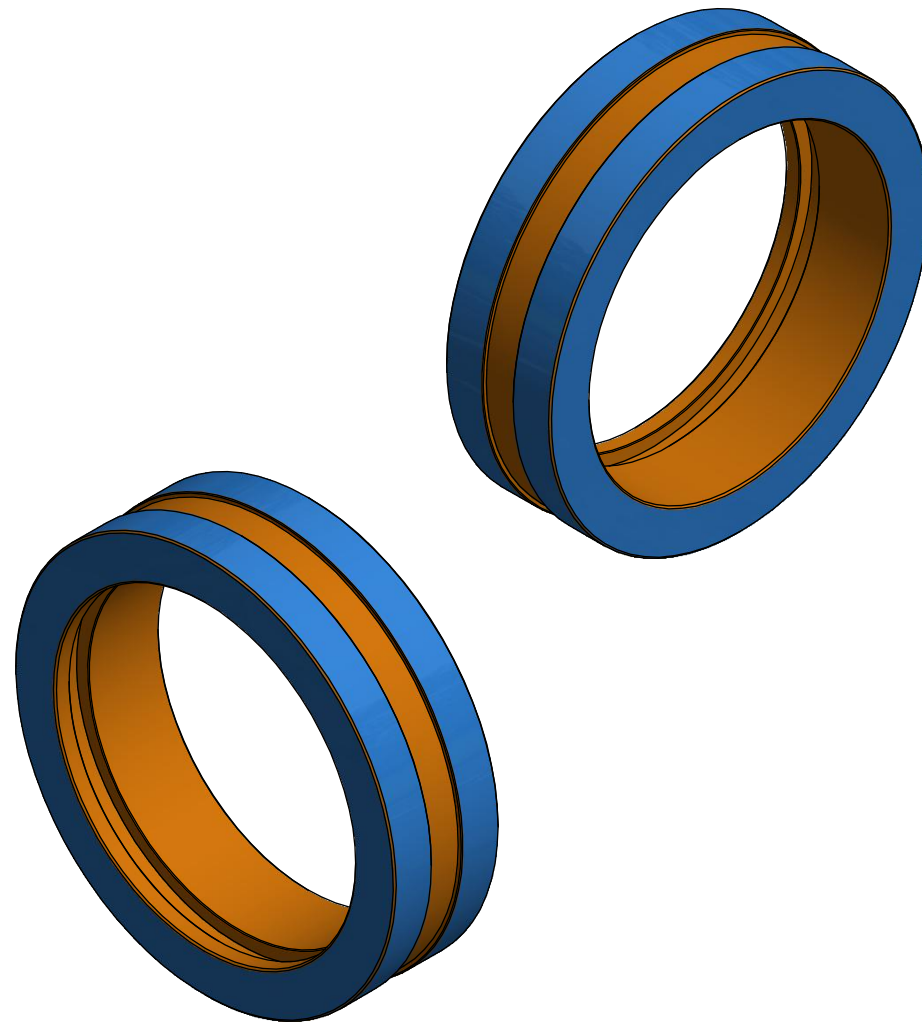
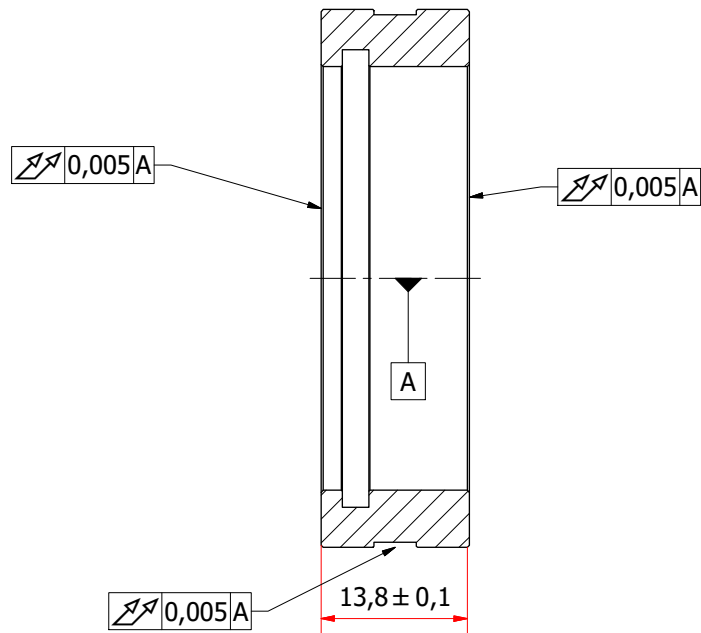
A-A (2 : 1)



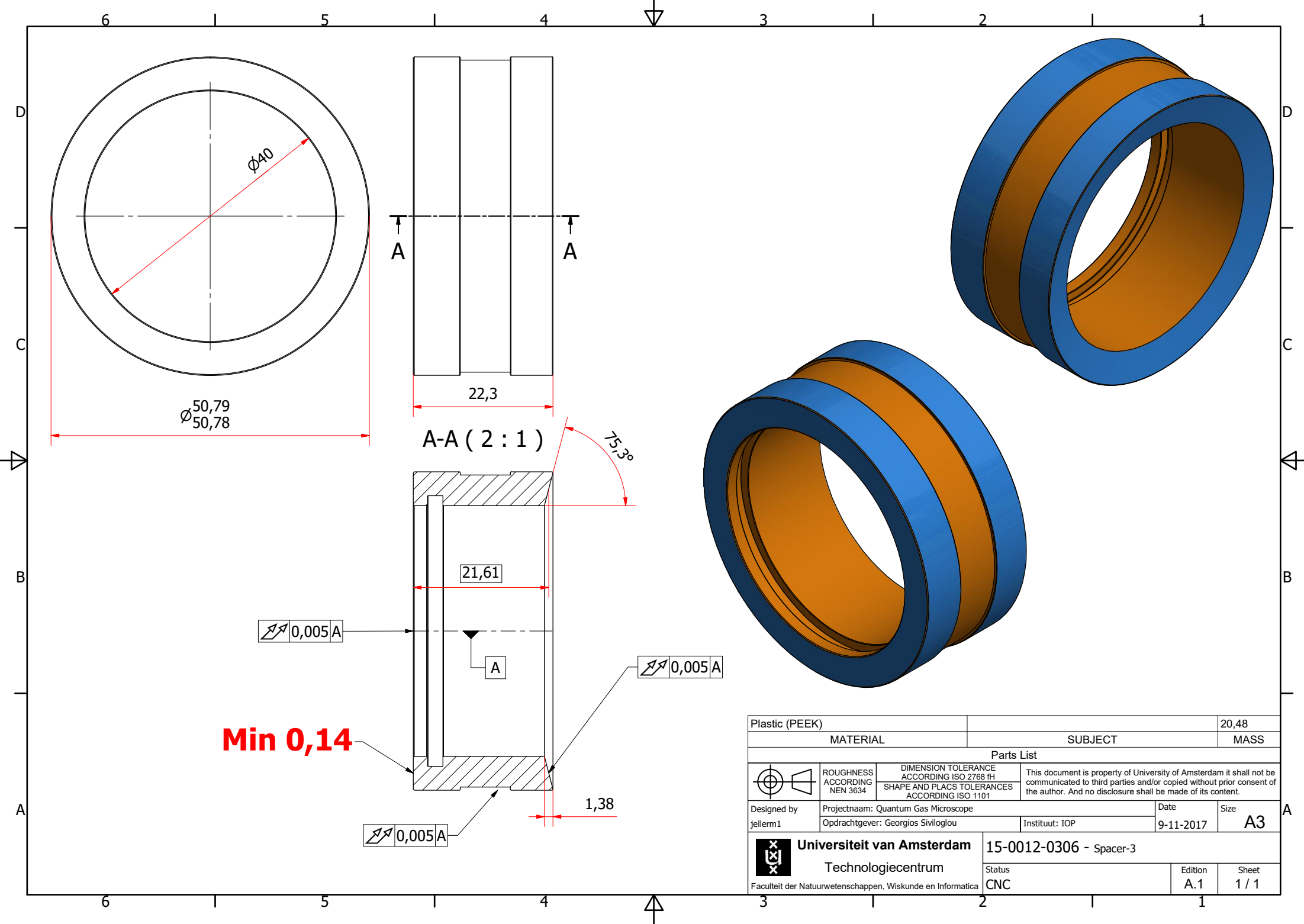
Plastic (PEEK)				7,66
MATERIAL		SUBJECT		MASS
Parts List				
	ROUGHNESS ACCORDING NEN 3634	DIMENSION TOLERANCE ACCORDING ISO 2768 fH	This document is property of University of Amsterdam it shall not be communicated to third parties and/or copied without prior consent of the author. And no disclosure shall be made of its content.	
		SHAPE AND PLACS TOLERANCES ACCORDING ISO 1101		
Designed by jellerm1	Projectnaam:	Date	Size	
	Opdrachtgever:	Instituut:	10-11-2017	A3
 Universiteit van Amsterdam Technologiecentrum Faculteit der Natuurwetenschappen, Wiskunde en Informatica	15-0012-0321 - Schroef Ring		Status	Sheet
			1	1 / 1



A-A (2 : 1)

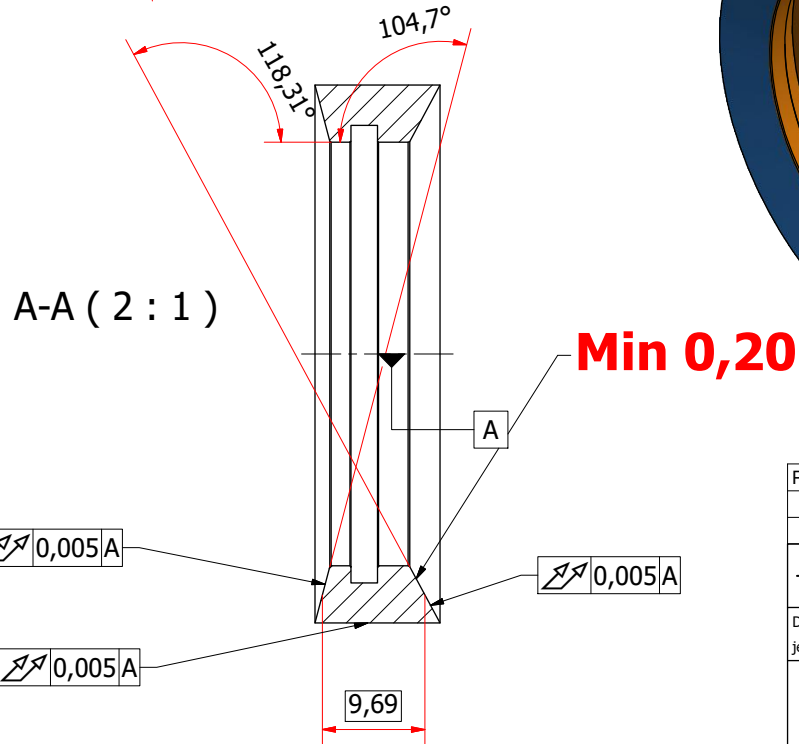
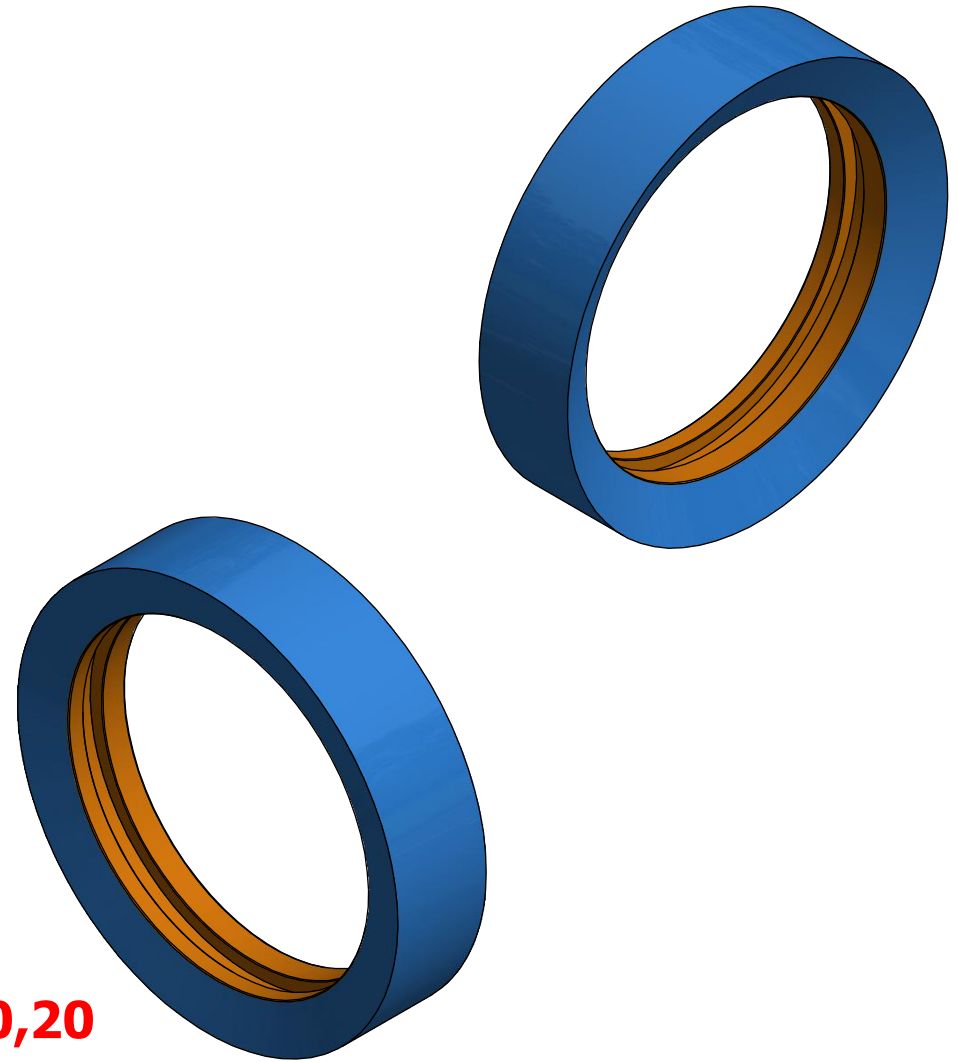
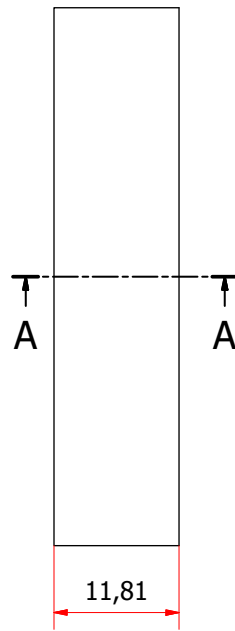
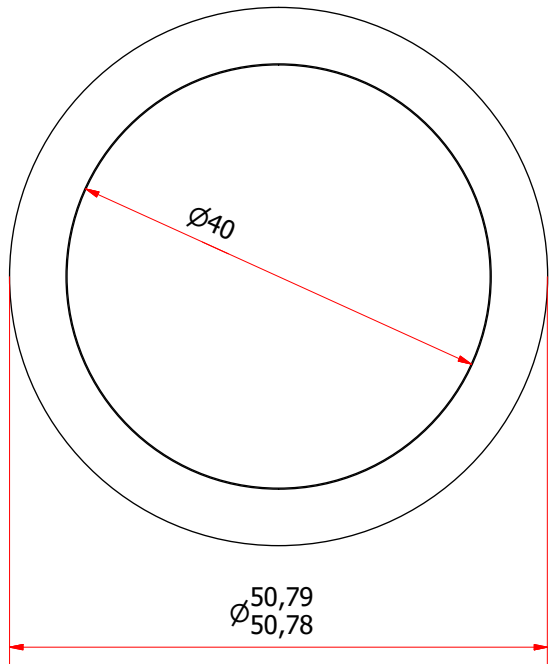


Plastic (PEEK)				13,11
MATERIAL		SUBJECT		MASS
Parts List				
	ROUGHNESS ACCORDING NEN 3634	DIMENSION TOLERANCE ACCORDING ISO 2768 fH	This document is property of University of Amsterdam it shall not be communicated to third parties and/or copied without prior consent of the author. And no disclosure shall be made of its content.	
		SHAPE AND PLACS TOLERANCES ACCORDING ISO 1101		
Designed by jellerm1	Projectnaam: Quantum Gas Microscope		Date 9-11-2017	Size A3
	Opdrachtgever: Georgios Siviloglou		Instituut: IOP	
Universiteit van Amsterdam Technologiecentrum Faculteit der Natuurwetenschappen, Wiskunde en Informatica		15-0012-0309 - Spacer-4		
		Status CNC	Edition A.1	Sheet 1 / 1

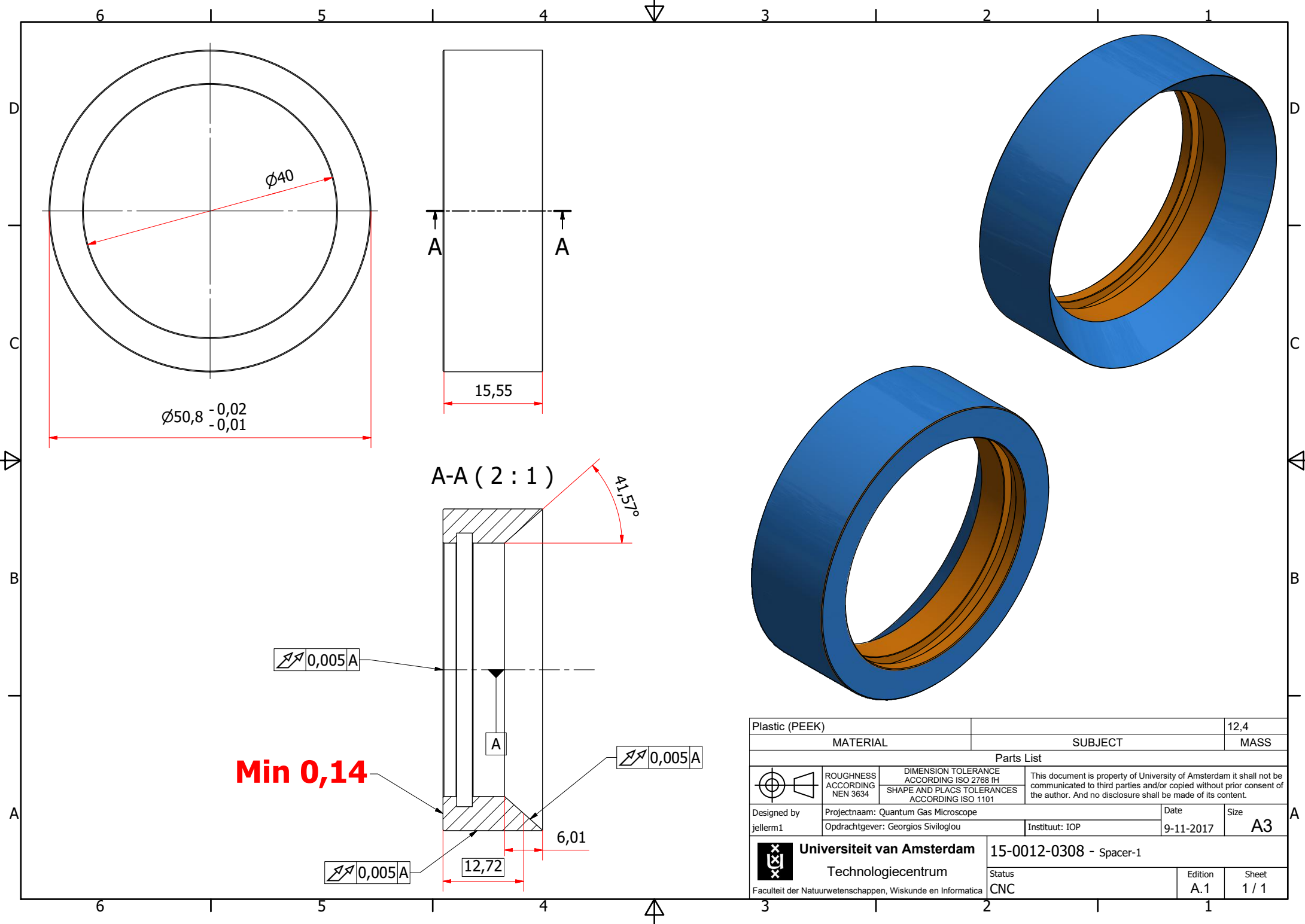


Min 0,14

Plastic (PEEK)		20,48	
MATERIAL		SUBJECT	
		MASS	
Parts List			
 ROUGHNESS ACCORDING NEN 3634	DIMENSION TOLERANCE ACCORDING ISO 2768 FH SHAPE AND PLACS TOLERANCES ACCORDING ISO 1101		This document is property of University of Amsterdam it shall not be communicated to third parties and/or copied without prior consent of the author. And no disclosure shall be made of its content.
	Designed by jellerm1	Projectnaam: Quantum Gas Microscope Opdrachtgever: Georgios Siviloglou	
Instituut: IOP		Size A3	
 Universiteit van Amsterdam Technologieceentrum Faculteit der Natuurwetenschappen, Wiskunde en Informatica		15-0012-0306 - Spacer-3	
		Status CNC	Edition A.1



Plastic (PEEK)		9,21	
MATERIAL		SUBJECT	
MASS		MASS	
Parts List			
	ROUGHNESS ACCORDING NEN 3634	DIMENSION TOLERANCE ACCORDING ISO 2768 fH SHAPE AND PLACS TOLERANCES ACCORDING ISO 1101	This document is property of University of Amsterdam it shall not be communicated to third parties and/or copied without prior consent of the author. And no disclosure shall be made of its content.
	Designed by jellerm1	Projectnaam: Quantum Gas Microscope Opdrachtgever: Georgios Siviloglou	
Universiteit van Amsterdam Technologiecentrum Faculteit der Natuurwetenschappen, Wiskunde en Informatica		15-0012-0307 - Spacer-2 Status CNC	
		Edition A.1	Size A3 Sheet 1 / 1



Min 0,14

Plastic (PEEK)		12,4	
MATERIAL		SUBJECT	
		MASS	
Parts List			
	ROUGHNESS ACCORDING NEN 3634	DIMENSION TOLERANCE ACCORDING ISO 2768 fH SHAPE AND PLACS TOLERANCES ACCORDING ISO 1101	This document is property of University of Amsterdam it shall not be communicated to third parties and/or copied without prior consent of the author. And no disclosure shall be made of its content.
	Designed by jellerm1		
Projectnaam: Quantum Gas Microscope		Size A3	
Opdrachtgever: Georgios Siviloglou		Instituut: IOP	
Universiteit van Amsterdam Technologiecentrum Faculteit der Natuurwetenschappen, Wiskunde en Informatica		15-0012-0308 - Spacer-1	
		Status CNC	Edition A.1
		Sheet 1 / 1	

Bibliography

- [1] R. de Wolf, *Quantum Computing: Lecture Notes*, University Lecture at University of Amsterdam.
- [2] M. McCorkle, *ORNL Launches Summit Supercomputer* (2018).
- [3] R. P. Feynman, *Simulating Physics with Computers*, *Int. J. Theor. Phys.* **21**, 467 (1982).
- [4] H. R. Calvert, *Astronomy: globes, orreries & other models*, London, HMSO, 1967 [ie 1968] (1967).
- [5] H. Weimer, *Lecture Notes on Quantum Simulation*, [arXiv preprint](#) (2017).
- [6] I. Bloch, J. Dalibard, and S. Nascimbene, *Quantum simulations with ultracold quantum gases*, *Nature Physics* **8**, 267 (2012).
- [7] A. M. Steane and C. J. Foot, *Laser Cooling below the Doppler Limit in a Magneto-Optical Trap*, *EPL (Europhysics Letters)* **14**, 231 (1991).
- [8] W. Ketterle and N. V. Druten, *Evaporative Cooling of Trapped Atoms*, vol. 37 of *Adv. At. Mol. Opt. Phys.*, 181 – 236, Academic Press (1996).
- [9] N. Masuhara, J. M. Doyle, J. C. Sandberg, D. Kleppner, T. J. Greytak, H. F. Hess, and G. P. Kochanski, *Evaporative cooling of spin-polarized atomic hydrogen*, *Phys. Rev. Lett.* **61**, 935 (1988).
- [10] M. H. Anderson, J. R. Ensher, M. R. Matthews, C. E. Wieman, and E. A. Cornell, *Observation of Bose-Einstein Condensation in a Dilute Atomic Vapor*, *Science* **269**, 198 (1995), ISSN 0036-8075.
- [11] K. B. Davis, M. O. Mewes, M. R. Andrews, N. J. van Druten, D. S. Durfee, D. M. Kurn, and W. Ketterle, *Bose-Einstein Condensation in a Gas of Sodium Atoms*, *Phys. Rev. Lett.* **75**, 3969 (1995).

- [12] Y. Takasu, K. Maki, K. Komori, T. Takano, K. Honda, M. Kumakura, T. Yabuzaki, and Y. Takahashi, *Spin-Singlet Bose-Einstein Condensation of Two-Electron Atoms*, [Phys. Rev. Lett. 91, 040404 \(2003\)](#).
- [13] S. Stellmer, M. K. Tey, B. Huang, R. Grimm, and F. Schreck, *Bose-Einstein condensation of strontium*, [Phys. Rev. Lett. 103, 200401 \(2009\)](#).
- [14] B. DeMarco and D. S. Jin, *Onset of Fermi degeneracy in a trapped atomic gas*, [Science 285, 1703 \(1999\)](#).
- [15] R. Grimm, *Low-temperature physics: A quantum revolution*, [Nature 435, 1035 \(2005\)](#).
- [16] M. W. Zwierlein, J. R. Abo-Shaeer, A. Schirotzek, C. H. Schunck, and W. Ketterle, *Vortices and superfluidity in a strongly interacting fermi gas*, [Nature 435, 1047 \(2005\)](#).
- [17] J. Dalibard, *Introduction to the physics of artificial gauge fields*, [arXiv e-prints \(2015\)](#).
- [18] J. C. Solem and L. C. Biedenharn, *Understanding geometrical phases in quantum mechanics: An elementary example*, [Foundations of Physics 23, 185 \(1993\)](#), ISSN 1572-9516.
- [19] Y.-J. Lin, K. Jiménez-García, and I. B. Spielman, *Spin-orbit-coupled Bose-Einstein condensates*, [Nature 471, 83 \(2011\)](#).
- [20] R. Jördens, N. Strohmaier, K. Günter, H. Moritz, and T. Esslinger, *A Mott insulator of fermionic atoms in an optical lattice*, [Nature 455, 204 \(2008\)](#).
- [21] M. Greiner, O. Mandel, T. Esslinger, T. W. Hänsch, and I. Bloch, *Quantum phase transition from a superfluid to a Mott insulator in a gas of ultracold atoms*, [Nature 415, 39 \(2002\)](#).
- [22] S. Kuhr, *Quantum-gas microscopes-A new tool for cold-atom quantum simulators*, [arXiv preprint](#) .
- [23] W. S. Bakr, J. I. Gillen, A. Peng, S. Fölling, and M. Greiner, *A quantum gas microscope for detecting single atoms in a Hubbard-regime optical lattice*, [Nature 462, 74 \(2009\)](#).
- [24] C. Weitenberg, *Single-atom resolved imaging and manipulation in an atomic Mott insulator*, Ph.D. thesis, lmu (2011).

- [25] M. Miranda, R. Inoue, Y. Okuyama, A. Nakamoto, and M. Kozuma, *Site-resolved imaging of ytterbium atoms in a two-dimensional optical lattice*, [Phys. Rev. A 91, 063414 \(2015\)](#).
- [26] L. W. Cheuk, M. A. Nichols, M. Okan, T. Gersdorf, V. V. Ramasesh, W. S. Bakr, T. Lompe, and M. W. Zwierlein, *Quantum-gas microscope for fermionic atoms*, [Phys. Rev. Lett. 114, 193001 \(2015\)](#).
- [27] R. Yamamoto, J. Kobayashi, T. Kuno, K. Kato, and Y. Takahashi, *An ytterbium quantum gas microscope with narrow-line laser cooling*, [New J. Phys. 18, 023016 \(2016\)](#).
- [28] E. Haller, J. Hudson, A. Kelly, D. A. Cotta, B. Peaudecerf, G. D. Bruce, and S. Kuhr, *Single-atom imaging of fermions in a quantum-gas microscope*, [Nature Physics 11, 738 \(2015\)](#).
- [29] J. Simon, W. S. Bakr, R. Ma, M. E. Tai, P. M. Preiss, and M. Greiner, *Quantum simulation of antiferromagnetic spin chains in an optical lattice*, [Nature 472, 307 \(2011\)](#).
- [30] T. Grünzweig, A. Hilliard, M. McGovern, and M. Andersen, *Near-deterministic preparation of a single atom in an optical microtrap*, [Nature Physics 6, 951 \(2010\)](#).
- [31] D. Barredo, V. Lienhard, S. de Léséleuc, T. Lahaye, and A. Browaeys, *Synthetic three-dimensional atomic structures assembled atom by atom*, [arXiv preprint \(2017\)](#).
- [32] M. Endres, H. Bernien, A. Keesling, H. Levine, E. R. Anschuetz, A. Krajenbrink, C. Senko, V. Vuletic, M. Greiner, and M. D. Lukin, *Atom-by-atom assembly of defect-free one-dimensional cold atom arrays*, [Science 354, 1024 \(2016\)](#), ISSN 0036-8075.
- [33] H. Bernien, S. Schwartz, A. Keesling, H. Levine, A. Omran, H. Pichler, S. Choi, A. S. Zibrov, M. Endres, M. Greiner, *et al.*, *Probing many-body dynamics on a 51-atom quantum simulator*, [Nature 551, 579 \(2017\)](#).
- [34] L. R. Liu, J. D. Hood, Y. Yu, J. T. Zhang, N. R. Hutzler, T. Rosenband, and K.-K. Ni, *Building one molecule from a reservoir of two atoms*, [Science 360, 900 \(2018\)](#), ISSN 0036-8075.
- [35] P. B. R. Nisbet-Jones, J. Dilley, A. Holleczek, O. Barter, and A. Kuhn, *Photonic qubits, qutrits and ququads accurately prepared and delivered on demand*, [New J. Phys. 15, 053007 \(2013\)](#).

- [36] A. M. Hankin, Y.-Y. Jau, L. P. Parazzoli, C. W. Chou, D. J. Armstrong, A. J. Landahl, and G. W. Biedermann, *Two-atom Rydberg blockade using direct $6S$ to nP excitation*, [Phys. Rev. A 89, 033416 \(2014\)](#).
- [37] M. Marcuzzi, J. Minář, D. Barredo, S. De Léséleuc, H. Labuhn, T. Lahaye, A. Browaeys, E. Levi, and I. Lesanovsky, *Facilitation dynamics and localization phenomena in Rydberg lattice gases with position disorder*, [Phys. Rev. Lett. 118, 063606 \(2017\)](#).
- [38] G. Pagano, F. Scazza, and M. Foss-Feig, *Fast and scalable quantum information processing with two-electron atoms in optical tweezer arrays*, [arXiv e-prints \(2018\)](#).
- [39] A. Baumgärtner, *A new apparatus for trapping and manipulating single Strontium atoms*, Master's thesis, University of Heidelberg (2017).
- [40] M. Martin, M. Bishof, M. Swallows, X. Zhang, C. Benko, J. Von-Stecher, A. Gorshkov, A. Rey, and J. Ye, *A quantum many-body spin system in an optical lattice clock*, [Science 341, 632 \(2013\)](#).
- [41] M. Borkowski, P. Morzyński, R. Ciuryło, P. S. Julienne, M. Yan, B. J. DeSalvo, and T. C. Killian, *Mass scaling and nonadiabatic effects in photoassociation spectroscopy of ultracold strontium atoms*, [Phys. Rev. A 90, 032713 \(2014\)](#).
- [42] S. Stellmer, *Degenerate quantum gases of strontium*, Ph.D. thesis, Austrian Academy of Sciences (2012).
- [43] A. Urech, *Work towards creating a quantum gas of strontium and the construction of 3P_0 & 3P_2 ultranarrow-linewidth lasers*, Master's thesis, University of Amsterdam (2017).
- [44] D. Douillet, E. Rolley, C. Guthmann, and A. Prevost, *An easy-to-build long working distance microscope*, [Phys. B 284, 2059 \(2000\)](#).
- [45] W. Alt, *An objective lens for efficient fluorescence detection of single atoms*, [Optik 113, 142 \(2002\)](#), ISSN 0030-4026.
- [46] L. Bennie, P. Starkey, M. Jasperse, C. Billington, R. Anderson, and L. Turner, *A versatile high resolution objective for imaging quantum gases*, [Opt. Express 21, 9011 \(2013\)](#).
- [47] B. E. Saleh, M. C. Teich, and B. E. Saleh, *Fundamentals of photonics*, vol. 22, Wiley New York (1991).
- [48] R. L. McCally, *Measurement of Gaussian beam parameters*, [Appl. Opt. 23, 2227 \(1984\)](#).

- [49] G. Airy, *On the Diffraction of an Object-glass with Circular Aperture*, Transactions of the Cambridge Philosophical Society 5, 283 (1835).
- [50] B. Zhang, J. Zerubia, and J.-C. Olivo-Marin, *Gaussian approximations of fluorescence microscope point-spread function models*, [Appl. Opt. 46, 1819 \(2007\)](#).
- [51] M. Spitaler, *Microscopic image restoration by deconvolution*, University Lecture at Imperial College London.
- [52] R. Jain, R. Kasturi, and B. G. Schunck, *Machine vision*, vol. 5, McGraw-Hill New York (1995).
- [53] W. T. Welford, *Aberrations of optical systems*, Routledge (2017).
- [54] Cor Berrevoets, *Aberrator* (2002), [Link](#).
- [55] Lambda Research Corporation, *Optics Software for Layout and Optimization* (2009), [Link](#).
- [56] E. J. Botcherby, R. Juskaitytis, M. J. Booth, and T. Wilson, *Aberration-free optical refocusing in high numerical aperture microscopy*, [Opt. Lett. 32 \(2007\)](#).
- [57] J. Burge, *Introductory Optomechanical Engineering OPTI 421/521*, University Lecture at University of Arizona (2016).
- [58] M. C. Funck, *Design and analysis of combinatorially assembled optical systems* (2012).
- [59] D. J. Griffiths, *Introduction to electrodynamics; 4th ed.*, Pearson, Boston, MA (2013), re-published by Cambridge University Press in 2017.
- [60] Ensinger, *ULTEM*, [Link](#).
- [61] Corning Inc., *Machinable Glass Ceramic For Industrial Applications* (2012), [Link](#).
- [62] K. Van de Velde and P. Kiekens, *Thermoplastic polymers: overview of several properties and their consequences in flax fibre reinforced composites*, [Polymer Testing 20, 885 \(2001\)](#).
- [63] AFT Fluorotec, *AF804 30% Carbon Fibre filled PEEK* (2009), [Link](#).
- [64] H. Chibani, K. Dukenbayev, M. Mensi, S. Sekatskii, and G. Dietler, *Near-field scanning optical microscopy using polymethylmethacrylate optical fiber probes*, [Ultramicroscopy 110, 211 \(2010\)](#).
- [65] H. J. Metcalf and P. Van der Straten, *Laser cooling and trapping*, Springer Science & Business Media (2012).

- [66] R. Grimm, M. Weidemüller, and Y. B. Ovchinnikov, *Optical Dipole Traps for Neutral Atoms*, [Adv. At. Mol. Opt. Phys. 42, 95 \(2000\)](#).
- [67] A. D. Ludlow, *The strontium optical lattice clock: optical spectroscopy with sub-Hertz accuracy*, Ph.D. thesis, University of Colorado at Boulder (2008).
- [68] M. M. Boyd, *High precision spectroscopy of strontium in an optical lattice: Towards a new standard for frequency and time*, Ph.D. thesis (2007).
- [69] J. E. Sansonetti and W. C. Martin, *Handbook of basic atomic spectroscopic data*, [Journal of Physical and Chemical Reference Data 34, 1559 \(2005\)](#).
- [70] S. Porsev, A. D. Ludlow, M. M. Boyd, and J. Ye, *Determination of Sr properties for a high-accuracy optical clock*, [Phys. Rev. A 78, 032508 \(2008\)](#).
- [71] V. Bagnato, D. E. Pritchard, and D. Kleppner, *Bose-Einstein condensation in an external potential*, [Phys. Rev. A 35, 4354 \(1987\)](#).
- [72] S. Stellmer, R. Grimm, and F. Schreck, *Production of quantum-degenerate strontium gases*, [Phys. Rev. A 87, 013611 \(2013\)](#).
- [73] M. Safronova, U. Safronova, and C. W. Clark, *Magic wavelengths for optical cooling and trapping of potassium*, [Phys. Rev. A 87, 052504 \(2013\)](#).
- [74] Y. H. Fung, *Near-deterministic preparation of single atoms and Raman sideband cooling*, Ph.D. thesis, University of Otago (2016).
- [75] W. J. Thompson, *Poisson Distributions*, [Computing in Science & Engineering 3, 78 \(2001\)](#), ISSN 1521-9615.
- [76] M. T. DePue, C. McCormick, S. L. Winoto, S. Oliver, and D. S. Weiss, *Unity occupation of sites in a 3D optical lattice*, [Phys. Rev. Lett. 82, 2262 \(1999\)](#).
- [77] Y. H. Fung, P. Sompet, and M. F. Andersen, *Single atoms preparation using light-assisted collisions*, [Technologies 4, 4 \(2016\)](#).
- [78] N. Schlosser, G. Reymond, and P. Grangier, *Collisional Blockade in Microscopic Optical Dipole Traps*, [Phys. Rev. Lett. 89, 023005 \(2002\)](#).
- [79] N. Schlosser, G. Reymond, I. Protsenko, and P. Grangier, *Sub-poissonian loading of single atoms in a microscopic dipole trap*, [Nature 411, 1024 \(2001\)](#).
- [80] D. Stuart, *Manipulating single atoms with optical tweezers*, Ph.D. thesis, University of Oxford (2014).

- [81] T. Zelevinsky, M. M. Boyd, A. D. Ludlow, T. Ido, J. Ye, R. Ciuryło, P. Naidon, and P. S. Julienne, *Narrow Line Photoassociation in an Optical Lattice*, [Phys. Rev. Lett. 96, 203201 \(2006\)](#).
- [82] E. Czuchaj, M. Krośnicki, and H. Stoll, *Valence ab initio calculation of the potential energy curves for the Sr₂ dimer*, [Chem. Phys. Lett. 371, 401 \(2003\)](#).
- [83] P. Sompet, A. V. Carpentier, Y. H. Fung, M. McGovern, and M. F. Andersen, *Dynamics of two atoms undergoing light-assisted collisions in an optical microtrap*, [Phys. Rev. A 88, 051401 \(2013\)](#).
- [84] A. Fuhrmanek, R. Bourgain, Y. R. P. Sortais, and A. Browaeys, *Light-assisted collisions between a few cold atoms in a microscopic dipole trap*, [Phys. Rev. A 85, 062708 \(2012\)](#).
- [85] P. S. Julienne, *Cold binary atomic collisions in a light field*, [J. Res. Natl. Inst. Stand. Technol. 101, 487 \(1996\)](#).
- [86] Andor Technology, *Andor Luca* (2007), [Link](#).
- [87] M. Hirsch, R. J. Wareham, M. L. Martin-Fernandez, M. P. Hobson, and D. J. Rolfe, *A stochastic model for electron multiplication charge-coupled devices—from theory to practice*, [PLoS One 8, e53671 \(2013\)](#).
- [88] A. M. Kaufman, B. J. Lester, and C. A. Regal, *Cooling a Single Atom in an Optical Tweezer to Its Quantum Ground State*, [Phys. Rev. X 2, 041014 \(2012\)](#).
- [89] M. Endres, H. Bernien, A. Keesling, H. Levine, E. R. Anschuetz, A. Krajenbrink, C. Senko, V. Vuletic, M. Greiner, and M. D. Lukin, *Atom-by-atom assembly of defect-free one-dimensional cold atom arrays*, [Science \(2016\)](#), ISSN 0036-8075.
- [90] D. Barredo, S. de Léséleuc, V. Lienhard, T. Lahaye, and A. Browaeys, *An atom-by-atom assembler of defect-free arbitrary 2D atomic arrays*, [Science \(2016\)](#), ISSN 0036-8075.
- [91] M. Saffman, T. G. Walker, and K. Mølmer, *Quantum information with Rydberg atoms*, [Rev. Mod. Phys. 82, 2313 \(2010\)](#).
- [92] A. Ciamei, A. Bayerle, C.-C. Chen, B. Pasquiou, and F. Schreck, *Efficient production of long-lived ultracold Sr₂ molecules*, [Phys. Rev. A 96, 013406 \(2017\)](#).
- [93] G. Reinaudi, C. B. Osborn, M. McDonald, S. Kotochigova, and T. Zelevinsky, *Optical Production of Stable Ultracold ⁸⁸Sr₂ Molecules*, [Phys. Rev. Lett. 109, 115303 \(2012\)](#).

-
- [94] S. Stellmer, B. Pasquiou, R. Grimm, and F. Schreck, *Creation of Ultracold Sr₂ Molecules in the Electronic Ground State*, [Phys. Rev. Lett. 109, 115302 \(2012\)](#).